

AD 687323



USAAVLABS TECHNICAL REPORT 68-180
PREDICTION OF ROTOR INSTABILITY AT
HIGH FORWARD SPEEDS
VOLUME IV
TORSIONAL DIVERGENCE

By
Charles F. Niehanch
H. L. Elman

February 1969

U. S. ARMY AVIATION MATERIEL LABORATORIES
FORT EUSTIS, VIRGINIA

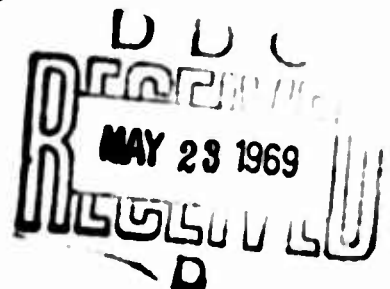
CONTRACT DA 44-177-AMC-332(T)

UNITED AIRCRAFT CORPORATION
SIKORSKY AIRCRAFT DIVISION
STRATFORD, CONNECTICUT

*This document has been approved
for public release and sale; its
distribution is unlimited.*



Reproduced by the
CLEARINGHOUSE
for Federal Scientific & Technical
Information Springfield Va. 2215.



DATE	DATE SECTION <input checked="" type="checkbox"/>
POS	DATE SECTION <input type="checkbox"/>
W-ADDRESS	<input type="checkbox"/>
LOCATION	
DISPOSITION/AVAILABILITY INDEX	
DEL.	MAIL IN W SPECIAL
/	

Disclaimers

The findings in this report are not to be construed as an official Department of the Army position unless so designated by other authorized documents.

When Government drawings, specifications, or other data are used for any purpose other than in connection with a definitely related Government procurement operation, the United States Government thereby incurs no responsibility nor any obligation whatsoever; and the fact that the Government may have formulated, furnished, or in any way supplied the said drawings, specifications, or other data is not to be regarded by implication or otherwise as in any manner licensing the holder or any other person or corporation, or conveying any rights or permission, to manufacture, use, or sell any patented invention that may in any way be related thereto.

Disposition Instructions

Destroy this report when no longer needed. Do not return it to the originator.



DEPARTMENT OF THE ARMY
U S ARMY AVIATION MATERIEL LABORATORIES
FORT RUSKIN VIRGINIA 22004

This contract was initiated to determine the aerodynamic stability limits of articulated and unarticulated helicopter rotor systems at high forward speeds. The four primary modes of aerodynamic instability (classical flutter, stall flutter, torsional divergence, and flapping or flatwise bending instability) were investigated. The possibility of a flap-lag instability suggested by Dr. Maurice I. Young of the Vertol Division, The Boeing Company, was investigated as a special case of flapping instability.

The results are published as a five-volume set; the subject of each volume is as follows:

Volume I	Equations of Motion
Volume II	Classical Flutter
Volume III	Stall Flutter
Volume IV	Torsional Divergence
Volume V	Flapping Instability

These reports have been reviewed by the U. S. Army Aviation Materiel Laboratories. These reports, which are published for the exchange of information and the stimulation of ideas, are considered to be technically sound with regard to technical approach, results, conclusions, and recommended parameter ranges for accurate usage.

Task 1F125901A13904
Contract DA 44-177-AMC-332(T)
USIAVLABS Technical Report 68-18D
February 1969

PREDICTION OF ROTOR INSTABILITY AT
HIGH FORWARD SPEEDS

SER-50469

Volume IV

Torsional Divergence

By

Charles F. Niebanck
and
H. L. Elsan

Prepared by

United Aircraft Corporation
Sikorsky Aircraft Division
Stratford, Connecticut

for

U. S. ARMY AVIATION MATERIEL LABORATORIES
PORT EUSTIS, VIRGINIA

This document has been approved
for public release and sale; its
distribution is unlimited.

SUMMARY

The purposes of this research program were to extend or develop analytical methods for determining rotor blade aeroelastic stability limits and to perform stability calculations over a range of design and operating variables for articulated and nonarticulated configurations. The usefulness of simpler analytical methods was investigated by comparing results with operating boundaries from the more elaborate analysis.

In the part of the investigation presented in this volume, a simple energy balance method for determining static stability was used to evaluate rotor blade torsional divergence boundaries, and a set of blade design charts was generated. To compare the results of this simple analysis with a more refined method, and to investigate the effects of parameters not included in the simple method, other calculations were made with the extended Normal Mode Transient Analysis.

One type of practical rotor blade operating boundary is defined by peak-to-peak torsional stress. The static torsional divergence stability boundary usually approximates this practical operating limit, as verified by the Normal Mode Transient Analysis calculations. This approximation is valid for an important number of blade parameters.

This part of the investigation is introduced with a description of the torsional divergence concept as it applies to rotorcraft blades. The condensed development of the simple energy balance method is given. The uniform blade design charts are the result of the application of this method. The uniform blades treated in the charts are of arbitrary size, control system flexibility, aerodynamic root cutout, and section center-of-gravity location. The results of additional calculations with the simple method for nonuniform blades are also given graphically. The independent effects of nonuniform blade chord, torsional stiffness, and inertia are shown, with inertial effects reflected by the use of the natural torsional vibration mode as an assumed divergence mode. The independent effects of nonuniform lift-curve slope caused by Mach number, pitch-flap coupling, and nonarticulation are presented in similar fashion. Normal Mode Transient Analysis calculations for verification of the simpler analysis include investigations of the effects of nonarticulation, reduced air density, control system flexibility, aft center-of-gravity position, and pitch-flap coupling on articulated blades. The effects of gyro feedback coupling on nonarticulated blades are also presented. Discussion of the results of this part includes the significance of the idealized torsional divergence parameters, the relative effects on torsional divergence of the various parameters, and permissible analytical assumptions useful in the calculation of the torsional divergence stability boundary.

Recommended preliminary design procedures, incorporating the charts generated for this volume are given for the rapid definition of blades with adequate torsional stiffness.

FOREWORD

The investigation presented in this volume is part of a general study of rotor blade aeroelastic instabilities, which is contained in five volumes. The work was performed under Contract DA 44-177-AMC-332(T) with the U. S. Army Aviation Materiel Laboratories, Fort Eustis, Virginia. The program was monitored for USAAVLABS by Mr. Joseph McGarvey.

The rotor blade torsional divergence analysis, design charts, and discussions in this volume are the result of work done at Sikorsky Aircraft by Mr. Charles F. Niebanck and at the United Aircraft Research Laboratories by Mr. H. L. Elman.

Volume I of this report contains the development of the differential equations of motion of an elastic rotor blade with chordwise mass unbalance.

Volume II presents a linearized discrete azimuth classical flutter analysis for rotor blades, with an appropriate parameter variation study, a comparison with test data, and a comparison with results calculated by using the method of Volume I.

Volume III describes a stall flutter analysis based on the calculation of aerodynamic work for a cycle of blade torsional vibration. Two-dimensional unsteady airfoil test data were used in the evaluation of the aerodynamic work. The analysis was used to generate stall flutter boundaries.

Volume V presents the results of a study of flapping and coupled flap-lag instability. The results of a parametric study based on a single-degree-of-freedom flapping or flatwise bending analysis are presented. Comparisons are made with results from the more elaborate method of Volume I. The results obtained by using the method of Volume I to determine the coupled flap-lag response of a rotor to a number of sudden control changes are presented.

TABLE OF CONTENTS

	<u>Page</u>
SUMMARY	iii
FOREWORD	v
LIST OF ILLUSTRATIONS	viii
LIST OF TABLES	xi
LIST OF SYMBOLS	xii
INTRODUCTION	1
DEVELOPMENT AND DISCUSSION OF TORSIONAL DIVERGENCE ANALYSIS	3
TORSIONAL DIVERGENCE DESIGN CHARTS	23
TORSIONAL DIVERGENCE CALCULATIONS WITH THE EXTENDED NORMAL MODE TRANSIENT ANALYSIS	31
DISCUSSIONS OF TORSIONAL DIVERGENCE RESULTS	38
CONCLUSIONS	108
RECOMMENDATION	109
DISTRIBUTION	110

LIST OF ILLUSTRATIONS

<u>Figure</u>		<u>Page</u>
1	Comparison of Differential Equation Solution and Assumed Divergence Mode	47
2	Advance Ratio Versus Torsional Stiffness Coefficient for Various Control Stiffness Ratios and Center-of- Gravity Positions; $X_{0s} = 0$, $\alpha_0 = 2\pi$	48
3	Reciprocal of Control Stiffness Ratio Versus Torsional Stiffness Coefficient; $X_{0s} = 0$, $\alpha_0 = 2\pi$	64
4	Center-of-Gravity Position With Respect to 25% Chord Versus Torsional Stiffness Coefficient; $X_{0s} = 0$, $\alpha_0 = 2\pi$	69
5	Effect of Linear Variation in Chord on Retreating Blade Torsional Divergence; $1/K = .001$, $Y_{CG}/C = 0$, $X_{0A} = .25$, $X_{0s} = 0$, $\alpha_0 = 2\pi$	80
6	Effect of Structural Cutout on Retreating Blade Torsional Divergence; $1/K = .001$, $Y_{CG}/C = 0$, $X_{0A} = 0$, $\alpha_0 = 2\pi$	81
7	Effect of Linear Variation in Stiffness on Retreating Blade Torsional Divergence; $1/K = .001$, $Y_{CG}/C = 0$, $X_{0A} = 0$, $X_{0s} = 0$, $\alpha_0 = 2\pi$	82
8	Effect of Inertial Cutout on Retreating Blade Torsional Divergence; $1/K = .001$, $Y_{CG}/C = 0$, $X_{0s} = 0$, $\alpha_0 = 2\pi$	83
9	Effect of Linear Variation in Inertia on Retreating Blade Torsional Divergence; $1/K = .001$, $X_{0A} = 0$, $X_{0s} = 0$, $\alpha_0 = 2\pi$	84
10	Effect of Prandtl-Glauert Mach Number Correction on Advancing Blade Torsional Divergence; $1/K = .001$, $Y_{CG}/C = -.10$, $X_{0A} = 0$, $X_{0s} = 0$	85
11	Effect of Prandtl-Glauert Mach Number Correction on Retreating Blade Torsional Divergence; $1/K = .001$, $Y_{CG}/C = 0$, $X_{0A} = 0$, $X_{0s} = 0$	86
12	Retreating Blade Torsional Divergence on Articulated and Nonarticulated Blades; $1/K = .001$, $Y_{CG}/C = .005$, $X_{0A} = 0$, $X_{0s} = 0$, $\rho \alpha_0 C_0^2/m = .168$	87
13	Advancing Blade Torsional Divergence on Articulated and Nonarticulated Blades; $1/K = .001$, $Y_{CG}/C = -.005$, $X_{0A} = 0$, $X_{0s} = 0$, $\rho \alpha_0 C_0^2/m = .168$	88

FigurePage

- 14 Effect of Pitch-Flap Coupling on Retreating Blade Torsional Divergence; $1/K = .001$, $X_{0A} = 0$, $X_{0S} = 0$, $\alpha_0 = 2\pi$ 89
- 15 Blade First Torsion Modal Response Versus Azimuth Angle for the Basic Articulated Rotor; $\mu = 1.6$, $\theta_{75R} = 0^\circ$, $Y_{CG}/C = 0$, $M_{1,90} = .85$ 90
- 16 Blade First Torsion Modal Response Versus Azimuth Angle for the Articulated Rotor with Aft Center of Gravity; $\mu = .6$, $\theta_{75R} = 2^\circ$, $Y_{CG}/C = -.15$, $M_{1,90} = .85$ 91
- 17 Vibratory Stress Versus Advance Ratio for the Basic Articulated Rotor; $1/K = 0$, $Y_{CG}/C = 0$, $X_{0A} = .12$, $X_{0S} = .060$, $M_{1,90} = .85$, $\delta_3 = 0$, $\alpha_0 \Omega^2 S_R = 96$ 92
- 18 Vibratory Stress Versus Advance Ratio for the Basic Articulated Rotor with Reduced Air Density; $1/K = 0$, $Y_{CG}/C = 0$, $X_{0A} = .12$, $X_{0S} = .060$, $M_{1,90} = .85$, $\rho = .001585$ SLUGS/FT³, $\delta_3 = 0^\circ$, $\alpha_0 \Omega^2 S_R = 144$ 93
- 19 Vibratory Stress Versus Advance Ratio for the Basic Articulated Rotor With Control System Flexibility; $1/K = .2$, $Y_{CG}/C = 0$, $X_{0A} = .12$, $X_{0S} = .060$, $M_{1,90} = .85$, $\delta_3 = 0^\circ$, $\alpha_0 \Omega^2 S_R = 96$ 94
- 20 Vibratory Stress Versus Advance Ratio for the Basic Articulated Rotor With Pitch-Flap Coupling; $1/K = 0$, $Y_{CG}/C = 0$, $X_{0A} = .12$, $X_{0S} = .060$, $M_{1,90} = .85$, $\delta_3 = 45^\circ$, $\alpha_0 \Omega^2 S_R = 96$ 95
- 21 Vibratory Stress Versus Center-of-Gravity Offset for the Articulated Rotor; $1/K = 0$, $X_{0A} = .12$, $X_{0S} = .060$, $\mu = .6$, $M_{1,90} = .85$, $\delta_3 = 0$, $\alpha_0 \Omega^2 S_R = 96$, $\theta_{75R} = 2^\circ$ 96
- 22 Vibratory Stress Versus Advance Ratio for the Basic Nonarticulated Rotor; $1/K = 0$, $Y_{CG}/C = 0$, $X_{0A} = .12$, $X_{0S} = .060$, $M_{1,90} = .85$, $\alpha_0 \Omega^2 S_R = 96$ 97
- 23 Vibratory Stress Versus Center-of-Gravity Offset for the Nonarticulated Rotor; $1/K = 0$, $X_{0A} = .12$, $X_{0S} = .060$, $\mu = .6$, $M_{1,90} = .85$, $\alpha_0 \Omega^2 S_R = 96$, $\theta_{75R} = 2^\circ$, $A_{1S} = -1^\circ$, $B_{1S} = 2^\circ$ 98

<u>Figure</u>		<u>Page</u>
24	Blade First Torsion Modal Response Versus Azimuth Angle for the Nonarticulated Rotor; $Y_{CG}/C = 0$, $\mu = 1.4$, $M_{1,0} = .85$	99
25	Effects of Torsional Stiffness Coefficient Variations on Typical Torsional Divergence Flight Condition Boundaries; $1/K = .001$, $Y_{CG}/C = 0$, $X_{0A} = .25$, $X_{0S} = 0$, $\alpha_0 = 2\pi$, $S_R(R\Omega)^2 = 2GJ/\rho \alpha_0 C_0^2 R^2$	100
26	Effects of Chordwise Center-of-Gravity Location on Typical Torsional Divergence Flight Condition Boundaries; $1/K = .001$, $X_{0A} = .25$, $X_{0S} = 0$, $\alpha_0 = 2\pi$, $S_R(R\Omega)^2 = 2GJ/\rho \alpha_0 C_0^2 R^2 = 16,750 \text{ FT/SEC}^2$. .	101
27	Effects of Aerodynamic Root Cutout on Typical Torsional Divergence Flight Condition Boundaries; $1/K = .001$, $Y_{CG}/C = 0$, $X_{0S} = 0$, $\alpha_0 = 2\pi$, $S_R(R\Omega)^2 = 2GJ/\rho \alpha_0 C_0^2 R^2 = 16,750 \text{ FT/SEC}^2$	102
28	Effects of Control Stiffness on Typical Torsional Divergence Flight Condition Boundaries; $Y_{CG}/C = 0$, $X_{0A} = .25$, $X_{0S} = 0$, $\alpha_0 = 2\pi$, $S_R(R\Omega)^2 = 2GJ/\rho \alpha_0 C_0^2 R^2 = 16,750 \text{ FT/SEC}^2$	103

LIST OF TABLES

<u>Table</u>		<u>Page</u>
I	Basic Properties of Rotor System Used in Torsional Divergence Studies With the Normal Mode Transient Analysis	104
II	Rotor Configurations for Torsional Divergence Study With the Normal Mode Transient Analysis	105
III	Flight Conditions for Torsional Divergence Study With Normal Mode Transient Analysis	106
IV	Configuration and Flight Condition Combinations for Torsional Divergence Study With the Normal Mode Transient Analysis	107

LIST OF SYMBOLS

A^*	speed of sound, ft/sec
A_{1s}	lateral cyclic pitch, deg
a_0	reference value (at 75% radius) of slope of C versus a_r curve, dC_L/da_r , rad^{-1}
a	local value of slope of C_L versus a_r curve, dC_L/da_r , rad^{-1}
B_{1s}	longitudinal cyclic pitch, deg
C_{1-14}	blade modal constants defined in Eq. (4) through Eq. (53)
C	local value of blade chord, ft.
C_0	reference value (at 75% radius) of blade chord, ft.
\bar{C}	local chord divided by rotor radius
C_d	section drag coefficient, $d/(1/2\rho U^2 C)$
$C_{m_{c/4}}$	section pitching moment coefficient about the 25% chord, $m_{c/4}/(1/2\rho U^2 C^2)$
C_L	section lift coefficient, $L/(1/2\rho U^2 C)$
E	Young's modulus of elasticity, lb/ft^2
EI_f	flatwise blade bending stiffness, lb-ft^2
e_0	reference distance (at 75% radius) between the coincident elastic and center-of-gravity axes and the aerodynamic center, ft
\bar{e}	flapping hinge radius divided by rotor radius
e_A	distance of the centroid of blade spar area forward of the elastic axis, ft.
G	shear modulus of elasticity, lb/ft^2
GJ	local blade torsional stiffness, lb-ft^2
GJ_T	local blade torsional stiffness at tip, lb-ft^2
GJ_R	local blade torsional stiffness at root, lb-ft^2

GJ_0	reference (at 75% radius) blade torsional stiffness, lb-ft ²
\bar{GJ}_0	nondimensional blade torsional stiffness, defined in Eq. (98)
g	acceleration of gravity, ft/sec ²
I_B	nondimensional blade flapping moment of inertia defined in Eq. (99)
J	torsional stiffness constant of blade section, ft ⁴
K	control stiffness-to-blade stiffness ratio, $K = K_r L_B / GJ_0$
K_r	control stiffness in torsion, ft-lb/rad
k	radius of gyration of blade section mass, ft.
k_A	radius of gyration of spar cross-sectional area, ft.
k_z	local blade mass radius of gyration in torsion, ft.
L_B	length of blade outboard of push rod location, ft.
l	lift force increment divided by blade radial increment, lb/ft
\bar{M}_B	blade mass divided by $m_0 R$
M_r	blade mass ratio $M_r = m_0 / \rho \pi C^2$
\bar{M}	nondimensional moment
$M_{1.90}$	advancing blade tip Mach number
$M_{75.90}$	advancing blade Mach number at the 75% rotor radius
$M_{75.270}$	retreating blade Mach number at the 75% rotor radius
M_e	moment due to elastic deformation of the blade, ft-lb
m	blade mass increment divided by radial increment, slugs/ft
m_0	reference value of m , slugs/ft
\bar{m}	local value of m divided by m_0
m_A	section aerodynamic pitching moment per unit span about elastic axis, ft-lb/ft

$m_{c/s}$	steady state section pitching moment per unit span, ft-lb/ft
m_{cw}	counterweight mass per unit span, lb-sec ² /ft ²
P_0, P_1	dimensionless constants in Eq. (109) which are determined by the boundary conditions for the differential equation
q	local dynamic pressure, lb/ft ²
q_{θ_1}	first torsion modal amplitude, rad
q_w	first flatwise bending modal amplitude, ft
$q_v()$	amplitude of () th edgewise deflection mode (equals blade tip deflection in z_0 direction divided by R when $\gamma_{w(1)}$ at tip is defined as 1.0)
$q_w()$	amplitude of () th flatwise deflection mode (equals blade tip deflection in z_0 direction divided by R when $\gamma_{w(1)}$ at tip is defined as 1.0)
$q_{\theta}()$	amplitude of () th elastic torsional mode (equals elastic twist angle about z_0 axis in radians at tip when $\gamma_{\theta(1)}$ at tip is defined as 1.0)
R	rotor radius, ft
R_I	tip value of blade torsional inertia per unit span divided by root value
r	distance along the blade radius from the flapping hinge for the articulated blades and from the rotor axis for the nonarticulated blade, ft
r	nondimensional value of r ; $r = r/R$
r_t	value of r at blade tip, ft
r_{ocw}	value of r at inboard end of counterweight, ft
r_{cg}	radius of blade center of gravity defined in Eq. (100)
S_A	aerodynamic shear force per unit span, lb/ft
S_c	nondimensional parameter, $S_c = GJ_0/\rho\pi C_0^2 R^2 (A^0)^2$
S_n	nondimensional torsional stiffness coefficient, defined in Eq. (108)
t	time, sec
U	resultant velocity at blade section, $U = \sqrt{U_T^2 + U_P^2}$, ft/sec

U_p	velocity component at blade section, normal to the local elastic axis direction and U_T , ft/sec
U_T	velocity component at blade section, normal to the local elastic axis direction and parallel to the plane of rotation, ft/sec
\bar{U}_T	local nondimensional relative air velocity, normal to the undeflected blade radius and parallel to the plane of rotation, $\bar{U}_T = \bar{U} + \bar{V} + \mu \sin \psi$
V	aircraft forward velocity, knots or ft/sec
V_e	local edgewise elastic displacement of elastic axis, ft
W_e	local flatwise elastic displacement of elastic axis, ft
x_n, y_n, z_n	coordinates in the nth axis system
r	radial distance from rotor axis of rotation divided by rotor radius
x_{OA}	radius of innermost aerodynamically effective blade section, divided by rotor radius (aerodynamic root cutout)
x_{OM}	radius of innermost blade section with appreciable torsional inertia, divided by rotor radius (inertial root cutout)
x_{OS}	radius of innermost torsionally flexible blade section, divided by rotor radius (structural root cutout)
\bar{Y}_{AC}	local chordwise distance from the elastic axis to the aerodynamic center divided by rotor radius, positive when the aerodynamic center is forward
Y_{CG}	local chordwise distance from blade elastic axis to blade center of gravity position, positive when center of gravity is forward, ft
\bar{Y}_{CG}	nondimensional center of gravity offset, Y_{CG}/R
α_s	rotor shaft angle of attack, positive nose up, rad
α_r	local blade section angle of attack, rad
β	blade flapping angle at hinge, rad
γ_{θ_1}	first uncoupled torsional natural vibration normalized mode shape
γ_{w_1}	first uncoupled bending natural vibration normalized mode shape
$\dot{\gamma}_{\theta_1}$	first derivative of γ_{θ_1} , $d\gamma_{\theta_1}/d\theta$

$\dot{\gamma}_w$	first derivative of γ_w , $d\gamma_w/d\tau$
$(\dot{\gamma}_\theta)_{PR}$	value of $\dot{\gamma}_\theta$ at push rod location
$(\dot{\gamma}_w)_{PR}$	value of $\dot{\gamma}_w$ at push rod location
$\gamma_{v(i)}$	()th uncoupled edgewise natural vibration normalized mode shape
$\gamma_{w(i)}$	()th uncoupled flatwise natural vibration normalized mode shape
$\gamma_{\theta(i)}$	()th uncoupled torsional natural vibration normalized mode shape
Δe_{acw}	distance between chordwise location of counterweight and chordwise location of spar centroid, positive when former is between centroid and leading edge, ft
δ	blade lead angle, rad
δ_c	pitch-flap coupling angle, $\delta_c = \arctan d\theta/d\beta$
θ	total local blade pitch angle, rad
θ_c	local blade pitch angle due to control system input and built-in twist, rad
θ_l	local blade pitch angle due to built-in linear twist, rad
θ_e	local elastic twist angle, rad
$\dot{\theta}_e$	rate of change of θ_e with respect to τ , rad
$\theta_{75\%}$	collective pitch setting expressed at the 75% radius, deg
λ	total air velocity component parallel to rotor shaft divided by rotational tip speed ΩR
μ	advance ratio, $V/\Omega R$
ξ	dummy variable of integration along rigid blade axis, ft
ρ	air density, slugs/ft ³
ϕ	local inflow angle, rad
ψ	blade azimuth angle, positive in direction of rotation from downwind, rad or deg
$\bar{\omega}_\theta$	first torsional natural frequency divided by rotor rotational frequency

$\bar{\omega}_0$	first flatwise bending natural frequency divided by rotor rotational frequency
ω_{v_i}	uncoupled natural frequency of () th edgewise vibratory mode, rad/sec
ω_{f_i}	uncoupled natural frequency of () th flatwise vibratory mode, rad/sec
ω_{θ_i}	uncoupled natural frequency of () th torsional vibratory mode, rad/sec
Ω	rotor angular velocity, rad/sec

SUBSCRIPTS

$i - jO$	indicates axis system under consideration, as defined in Volume I of this report
$C/4$	indicates quantity evaluated at 25% chord
$3C/4$	indicates quantity evaluated at 75% chord
o	denotes a known discreet set of values, as used in Eq. (118)
$c g$	indicates quantity evaluated at local chordwise center of gravity
cw	indicates quantity pertaining to the blade counterweight
eo	indicates quantity evaluated at elastic axis
FD	indicates flap damper or quantity evaluated at flap damper attachment point as appropriate
i, i', m	flatwise mode subscripts
j, j', k	torsional mode subscripts
LD	indicates lag damper or quantity evaluated at lag damper attachment point as appropriate
PR	indicates pushrod or quantity evaluated at pushrod attachment point as appropriate
p, p', n	edgewise mode subscripts (maximum value = 2)
$\bar{r} = 0$	indicates quantity evaluated at $\bar{r} = 0$
x, y, z	indicates quantity evaluated in x , y or z direction as defined in Volume I of this report

$x(), y(), z()$ indicates quantity evaluated in x , y or z direction of () axis system as defined in Volume I of this report

$y_{ocq} = 0$ indicates quantity evaluated at $y_{ocq} = 0$

DERIVATIVE NOTATION

$d()/dr$ indicates derivative of () with respect to r

$()'$ indicates derivative of () with respect to r

$()^\circ$ indicates derivative of () with respect to t

$()^{\ddot{}}$ indicates derivative of () with respect to t (i.e., $\ddot{}$)

MISCELLANEOUS

$(\vec{\quad})$ indicates vector quantity

$(\bar{\quad})$ indicates quantity nondimensionalized through the use of factors, R , m_0 , and Ω

INTRODUCTION

One of the basic aeroelastic investigations applying to fixed wings is the torsional divergence analysis, for cases where the center of pressure is ahead of the elastic axis. The central concept is the presence of an aerodynamic torsional couple on the wing, which increases linearly with angle of attack and which therefore varies in similar fashion as the wing twists. These couples, which are opposed by an elastic restoring torque, increase with the square of the forward velocity for a given angle of attack. In such a case, the aerodynamic couple is proportional to the square of the speed and linear with the twisting deformation, while elastic resisting couple is proportional to the twisting deformation alone. It is clear that a velocity will exist for which an increment in the aerodynamic twisting couple is equal to the corresponding increment of elastic resisting couple for any arbitrary deflection. This is known as the torsional divergence speed. Below this speed, the elastic resistance to an increment in torsional deflection will be greater than the corresponding aerodynamic couple, and the deflection will find its equilibrium value. Above it, the increment in elastic resistance will be less than the increment in the aerodynamic couple, and the simple divergence theory predicts a continuous growth in deflection. It should be noted in passing that the divergence speed may be either larger or smaller than the classical flutter speed.

The above concept of a torsional divergence for a fixed wing led to an examination of similar situations existing for helicopter rotors. Obviously, the velocity distribution on a helicopter rotor varies along the span and is rapidly and continuously changing. Hence, the static stability analysis for torsional divergence applies only to an instantaneous condition. In fact, the torsional divergence situation for a helicopter rotor blade usually develops on the retreating blade for advance ratios greater than unity. The blade is then traveling backwards (sharp edge first) through the air for part of each revolution, and the aerodynamic center moves close to what is normally the 75% chord position. This produces a large torsional moment arm about the blade elastic axis and center-of-gravity position at or near the 25% chord position. Hence, torsional divergence will be encountered for the retreating blade even though the relative velocity is comparatively low.

A more detailed description of the theoretical approach to the torsional divergence calculations will follow later. However, a definition of torsional divergence can be given at this point. In terms of theory, the torsional divergence boundary is that set of flight conditions where blade static aeroelastic stability in torsion is just satisfied at either the advancing or retreating blade positions. The practical effect of exceeding this boundary has been found to be a steep rise in blade torsional vibratory stress levels.

In this volume of the report, the flight conditions for torsional divergence have been examined extensively, and useful design charts have been prepared. These critical flight conditions have also been examined with the much more rigorous extended Normal Mode Transient Analysis, which provides solutions for the flexible blade equations of motion. It is generally verified that the torsional divergence analysis fulfills its purpose, which is the definition of potentially troublesome flight conditions which should be avoided or investigated further.

DEVELOPMENT AND DISCUSSION OF TORSIONAL DIVERGENCE ANALYSIS

Rotor blades on high speed helicopters can experience torsional divergence as discussed earlier. One essential difference between helicopter blade and fixed wing torsional divergence is the role played by the center-of-gravity location. For a fixed wing, the torsional moment causing the divergence is the lift force increment multiplied by the distance between the aerodynamic center of pressure and the elastic axis. For articulated rotor blades, and nonarticulated rotor blades of conventional stiffness, most of the resistance to blade vertical deflection is supplied by centrifugal force components rather than by elastic forces. For this reason, the torsional moment causing the torsional divergence of a rotor blade of conventional stiffness is very nearly the lift force increment multiplied by the distance between the aerodynamic center of pressure and the center of gravity. On a blade of conventional stiffness, the distance between the elastic axis and the aerodynamic center will have very little effect on the torsional divergence speed.

In the case of nonarticulated rotor blades which are to be stopped in flight, the torsional divergence mechanism is more like that for fixed wings. As the rotor angular velocity, is decreased, the blade vertical stiffness due to centrifugal effects diminishes, and the vertical elastic forces must resist a larger portion of the vertical loads on the blade. If the rotor is stopped, the basic torsional divergence mechanism is the same as that for a fixed wing. It should be noted that the combined effects of centrifugal and elastic stiffness are considered in the non-articulated blade torsional divergence analysis to be presented later.

As explained above, the torsional moment which causes blade torsional divergence arises because the lift forces on the blade are not coincident with the center of centrifugal and elastic forces resisting the vertical deflection of the blade. In order for the moment to produce a potentially unstable mechanism, the moment must cause the blade angle of attack to become greater when the lift force becomes greater. This condition is obtained when the aerodynamic center of pressure is forward of the center of the effective centrifugal and elastic forces resisting vertical motion of the blade. If the aerodynamic center of pressure is aft of the center of effective vertical resistance, torsional divergence cannot occur, since an increase in lift will result in a blade torsional deflection which will decrease the angle of attack.

It is instructive to examine the conditions for which a conventional blade can encounter the stable and unstable situations just described. If the blade center of gravity, aerodynamic center of pressure, and elastic axis are at the 25% chord position, no torsional divergence is possible on an advancing blade, since the aerodynamic center of pressure coincides with the center of vertical resistance. If the center of gravity is ahead of the 25% chord position, the moment produced by a lift increment is statically stabilizing. In this case, the blade on the advancing side of the rotor will tend to twist so as to reduce the lift increment due to a gust or a control movement. If, on the other hand, the center of gravity is

aft of the 25% chord position, the moment produced by a lift increment is potentially unstable for the advancing blade. As pointed out earlier, the relative position of the elastic axis with respect to the aerodynamic center has a similar but much weaker effect for the conventional rotor blade. Thus the usual rotor blade configuration will be immune to torsional divergence on the advancing side of the rotor. This is not true, however, for a blade on the retreating side of the rotor when the advance ratio is high enough to produce reverse flow over most of the blade. In the reverse flow region, the blade is traveling through the air backwards, and the aerodynamic center of pressure moves to the position which is usually referred to as the 75% chord position. Since the blade center of gravity and elastic axis remain at the 25% chord position, the distance between the aerodynamic center of pressure and the center of the effective blade vertical stiffness is 50% of the chord. This produces a potential static instability, which fortunately is mitigated by the lower dynamic pressures on the retreating blade. It should be noted that for the retreating blade, moving the center of gravity towards the normal trailing edge decreases the unstable tendency, since it is then closer to the actual aerodynamic center. The opposite effect is produced by moving the center of gravity forward towards the normal leading edge.

As mentioned in the previous discussion, the usual rotor blade configuration will experience static torsional divergence only in a region of reverse flow. A single degree of freedom analysis is adequate for a study of the effect of torsional stiffness on torsional divergence of an articulated blade with this normal configuration. In order to evaluate the effects of pitch-flap coupling and nonarticulation with arbitrary center of gravity location, a two-degree-of-freedom analysis is required, and was therefore used in this investigation.

The general approach followed in this analysis is the development of two equations of static stability involving one torsional and one flapping, or flatwise bending, degree of freedom. The determinant of these two homogeneous equations is evaluated. A zero value for this determinant indicates that the blade is operating on the boundary between a statically stable and a statically unstable regime. Operation of the rotor in a flight condition beyond this static stability boundary does not imply that blade deflections will increase indefinitely, since the condition will generally exist over only a portion of the rotor disc. The amplitude of the blade deflections is affected not only by the extent and severity of the statically unstable region, but also by blade inertia, damping, and blade motions upon entry into the unstable region. Therefore, the results of an analysis of the type presented here serve principally to indicate those flight conditions which are potentially troublesome from the standpoint of adequate blade torsional stiffness and which should be analyzed in further detail.

Inclusion of chordwise mass unbalance for nonarticulated blades and pitch-flap coupling effects requires consideration of blade deflection out of the plane of rotation as well as blade torsional deflections about the elastic axis. It was assumed that the first natural torsional vibration mode and the rigid flapping mode would adequately represent the deflections

of articulated rotors. It was further assumed that the first torsion and flatwise bending modes would represent the deflection of nonarticulated rotors. The total torsional spring coefficient was obtained from the blade equations of motion presented in Volume I of this report. A list of the principal simplifying assumptions made to arrive at the equations used here is given below:

1. All dynamic terms are neglected.
2. All edgewise and lag terms are neglected, as are the terms involving flatwise and torsional modal amplitudes other than the first.
3. For articulated rotors, the flatwise bending amplitude is zero; for nonarticulated rotors, the blade is rigidly cantilevered at the root.
4. The lift force is the only aerodynamic force. It is described by means of a linearized lift-curve slope, which is the same absolute magnitude in both conventional and reverse incompressible flows. When desired, compressibility effects can be accounted for by the Prandtl-Glauert correction, which is applied to both conventional and reverse flow.
5. Only steady-state aerodynamics are considered and the aerodynamic center of pressure is located at the 25% chord for conventional flow or at the 75% chord for reverse flow.
6. The resultant section velocity is equal to the tangential velocity component.
7. Terms involving collective or cyclic pitch, blade pre-twist, precone and second and higher products of modal amplitudes are neglected.
8. Blade angles of attack remain small in forward flow and are close to 180° in reverse flow.

The equations of static stability were developed by applying the assumptions mentioned above to modal equations, used in the Normal Mode Transient Analysis of Volume I. These modal equations arise by effectively setting the virtual work done by the aerodynamic loads and centrifugal effects equal to the change in strain energy during a virtual displacement of the assumed modes. This consideration of energy terms gives rise to the description of the static stability analysis as an "energy method".

The development of the analysis will begin with the modal equations given in Volume I. The equations needed are the flatwise bending modal equation, the torsional modal equation, and the flap angle modal equation. In Volume I these appear as Eqs. (80), (89), and (91) respectively. For convenience, they are reproduced below as Eqs. (1), (2), and (3). Many of the terms in these equations from Volume I are eliminated herein, since they do not pertain to the static divergence concept. Some terms will be used for the divergence analysis of both articulated and nonarticulated blades, while others will be applicable to articulated blades only, or to nonarticulated blades only. The specific reasons for deleting the various terms will be given. Volume I, of course, gives a more complete discussion of the modal equations.

The flatwise bending modal equation from Volume I of this report is

$$\begin{aligned}
 0 = & \int_0^{\bar{r}} \chi_{w1} \left[i \bar{S}_A z_s \cos \Theta - (\bar{S}_A)_{y_s} \sin \Theta \right] d\bar{r} - \bar{M}_{PR} \cos \theta_{PR} (\gamma_{w1}')_{r=0} + \sin \theta_{LD} \bar{M}_{LD} (\gamma_{w1}')_{r=0} \\
 & - \cos \theta_{TD} \bar{M}_{TD} (\gamma_{w1}')_{r=0} - C_{11} \left[\bar{a}_{w1} + q_{w1} \left(\bar{w}_{w1}^2 - \dot{\theta}_0^2 - 2\beta \dot{\theta}_0 + \dot{\beta} \sin 2\theta_0 - \frac{1}{2} (1 \right. \right. \\
 & \left. \left. + 2\dot{\beta}) (1 - \cos 2\theta_0) \right) \right] + \sum_i q_{wi} \left[-2\theta_1 \bar{w}_{wi}^2 c_{9,1,1} + \theta_1 \sin 2\theta_0 c_{60,1,1} + 2\dot{\beta} (c_7 - c_4)_{1,1} \right. \\
 & \left. - 2\dot{\theta}_0 \sin \theta_0 (c_{65} - c_{69})_{1,1} \right] + \sum_p q_{vp} \left\{ c_{3p} \left[-\bar{\theta}_0 - \dot{\beta} (1 - \cos 2\theta_0) - \frac{1}{2} (1 + 2\dot{\beta}) \sin 2\theta_0 \right] \right. \\
 & \left. - \theta_1 \cos 2\theta_0 (c_5 - 0.75 c_3)_{1,p} - c_{27,1,p} + 2\theta_1 (1 + \bar{w}_{vp}^2) c_{8,1,p} - \theta_1 c_{5,1,p} \right\} \\
 & + \sum_p \dot{q}_{vp} \left[-2 \sin \theta_0 c_{64,1,p} - 2(\dot{\theta}_0 + \beta) c_{3,1,p} \right] + 2 \sum_p \sum_i q_{ip} q_{vp} (1 + \bar{w}_{vp}^2) c_{67,1,p,i} \\
 & - \sum_i \ddot{q}_{ip} c_{62,1,i} + \sum_i q_{ip} \left[c_{57,1,i} - c_{62,1,i} \cos 2\theta_0 + c_{56,1,i} \langle (\ddot{\beta} + \beta) \sin \theta_0 + \dot{\beta} \cos \theta_0 \rangle \right. \\
 & \left. - c_{61,1,i} \right] - C_{11} \left[\bar{e} (\beta \cos \theta_0 - \delta \sin \theta_0) + \bar{q}_{z_s} \cos \theta_0 - \bar{q}_{y_s} \sin \theta_0 \right] - C_{12} \left[(\ddot{\beta} \right. \\
 & \left. + \beta + 2\beta \dot{\beta}) \cos \theta_0 + (2\beta \dot{\beta} - \ddot{\theta}_0) \sin \theta_0 \right] + C_{13} \left[(\ddot{\beta} + \beta) \sin \theta_0 + \dot{\beta} \cos \theta_0 \right] \\
 & - C_{63} \left[\bar{\theta}_0 + \dot{\beta} (1 - \cos 2\theta_0) + \frac{1}{2} (1 + 2\dot{\beta}) \sin 2\theta_0 \right] - \theta_1 \cos 2\theta_0 c_{60,1} - 0.75 c_{63,1} - \theta_1 c_{60,1}
 \end{aligned}
 \tag{1}$$

The torsional modal equation from Volume I of this report is

$$\begin{aligned}
 0 = & \int_0^{\bar{r}_T} \gamma_{\theta_1} (\bar{m}_A)_{z_3} d\bar{r} + c_{37} + \cos 2\theta_0 c_{80} - \sum_i \ddot{q}_w c_{82,i} - c_{38} \ddot{q}_{\theta_1} \\
 & + c_{38} q_{\theta_1} (1 - \bar{u}_{\theta_1}^2 - \cos 2\theta_0) - c_{44} \left[\ddot{\theta}_0 + \frac{1}{2} (1 + 2\dot{\theta}) \sin 2\theta_0 + \dot{\theta} (1 - \cos 2\theta_0) \right] \\
 & - \sum_i \sum_p q_w q_p c_{46,i,p} + \theta_1 \sum_i \sum_p q_w q_p c_{38,i,p} + \theta_1 \sum_p \sum_p q_p q_p c_{38,p,p} \\
 & + \sum_i q_w \left[2\dot{\theta}_0 \sin \theta_0 c_{10,i} - c_{86,i} - 2\dot{\theta} c_{88,i} - \bar{e} c_{83,i} - (1 + 2\dot{\theta}) c_{84,i} - c_{82,i} \langle -\dot{\theta}_0^2 \right. \\
 & \left. - 2\beta \dot{\theta}_0 + \dot{\theta} \sin 2\theta_0 - \frac{1}{2} (1 + 2\dot{\theta}) (1 - \cos 2\theta_0) \rangle + \sin 2\theta_0 c_{93,i} \right] \\
 & - \sum_p \ddot{q}_p \left[2 \sin \theta_0 c_{82,p} + 2 c_{74,p} (\dot{\theta}_0 + \beta) \right] + \sum_p q_p \left[2 \theta_1 c_{87,p} - \theta_1 c_{88,p} - c_{74,p} \langle \dot{\theta}_0^2 \right. \\
 & \left. + \dot{\theta} (1 - \cos 2\theta_0) + \frac{1}{2} (1 + 2\dot{\theta}) \sin 2\theta_0 \rangle - \cos 2\theta_0 c_{114,p} \right] \\
 & - \sum_i \sum_p 2 c_{111,i,p} q_w (\dot{q}_p \cos \theta_0 - q_p \dot{\theta}_0 \sin \theta_0) + \sum_i \sum_p 2 c_{112,i,p} q_w (\dot{q}_w \sin \theta_0 \\
 & - q_w \dot{\theta}_0 \cos \theta_0) - c_{92} [\bar{e} (\beta \cos \theta_0 - \dot{\theta} \sin \theta_0) + \bar{q}_2 \cos \theta_0 - \bar{q}_2 \sin \theta_0] \\
 & - c_{93} [(\dot{\beta} + \beta + 2\beta \dot{\theta}) \cos \theta_0 - (\ddot{\theta} - 2\beta \dot{\theta}) \sin \theta_0] + c_{94} [(\dot{\beta} + \beta) \sin \theta_0 \\
 & + \ddot{\theta} \cos \theta_0] + \sum_i q_{\theta_1} c_{113,i} [(\dot{\beta} + \beta) \sin \theta_0 - \ddot{\theta} \cos \theta_0] \quad (2)
 \end{aligned}$$

The flap angle equation from Volume I of this report is

$$\begin{aligned}
 0 = & -\bar{M}_{FD} + \int_0^{\bar{r}_T} (\bar{S}_A)_{z_3} \bar{r} d\bar{r} - \bar{M}_B \bar{r}_{c9} (\bar{e}\beta + \bar{q}_{z_3}) - \bar{I}_B [\ddot{\beta} + \beta (1 + 2\dot{\theta})] \\
 & - c_{97} [\ddot{\theta}_0 \cos \theta_0 - \dot{\theta}_0^2 \sin \theta_0 - 2\beta \dot{\theta}_0 \sin \theta_0 - (1 + 2\dot{\theta}) \sin \theta_0] \\
 & - \tan \delta_3 (\bar{GJ})_{r=0} \sum_i (\gamma_{\theta_1})_{r=0} q_{\theta_1} - \bar{e} \left[\sum_i q_w c_{10,i} \cos \theta_0 \right. \\
 & \left. + \sum_p q_p c_{15,p} \sin \theta_0 + \sin \theta_0 c_{96} \right] \quad (3)
 \end{aligned}$$

The modal constants C_1 through C_{114} are defined in Appendix IV of Volume I. They are reproduced below for convenience

$$C_{11} = \int_0^{\bar{T}_T} \bar{m} \chi_{w1}^2 d\bar{r} \quad (4)$$

$$C_{31,p} = \int_0^{\bar{T}_T} \bar{m} \gamma_{w1} \gamma_{vp} d\bar{r} \quad (5)$$

$$C_{41,1'} = \int_0^{\bar{T}_T} \bar{m} \gamma_{w1} \gamma'_{w1,1'} d\bar{r} \quad (6)$$

$$C_{51,p} = \int_0^{\bar{T}_T} \bar{m} \gamma_{w1} \gamma_{vp} \bar{r} d\bar{r} \quad (7)$$

$$C_{71,1'} = \int_0^{\bar{T}_T} \gamma_{w1} \chi_{w1}'' \int_{\bar{r}}^{\bar{T}_T} \bar{m} \bar{\xi} d\bar{\xi} d\bar{r} \quad (8)$$

$$C_{81,p} = \int_0^{\bar{T}_T} \chi_{w1} \int_{\bar{r}}^{\bar{T}_T} \bar{m} \gamma_{vp} d\bar{\xi} d\bar{r} \quad (9)$$

$$C_{91,1'} = \theta_1 \int_0^{\bar{T}_T} \chi_{w1} \left[\int_{\bar{r}}^{\bar{T}_T} \bar{m} \chi_{w1} \bar{\xi} d\bar{\xi} - \bar{r} \int_{\bar{r}}^{\bar{T}_T} \bar{m} \gamma_{w1} d\bar{\xi} \right] d\bar{r} \quad (10)$$

$$C_{101} = \int_0^{\bar{T}_T} \bar{m} \gamma_{w1} d\bar{r} \quad (11)$$

$$C_{121} = \int_0^{\bar{T}_T} \bar{m} \gamma_{w1} \bar{r} d\bar{r} \quad (12)$$

$$C_{131} = \theta_1 \int_0^{\bar{T}_T} \bar{m} \bar{r} \gamma_{w1} (\bar{T} - 0.75) d\bar{r} \quad (13)$$

$$C_{15p} = \int_0^{\bar{T}_T} \bar{m} \gamma_{vp} d\bar{r} \quad (14)$$

$$C_{271,p} = 2\theta_1 \int_0^{\bar{T}_T} \gamma_{w1} (\bar{E}\bar{I}_1 \gamma'_{vp})'' d\bar{r} = -2\theta_1 \int_0^{\bar{T}_T} \chi_{w1} \left[\bar{E}\bar{I}_1 \gamma'_{vp} + \bar{E}\bar{I}_1 \gamma''_{vp} \right] d\bar{r} \quad (15)$$

$$C_{361} = \int_0^{\bar{T}_T} \bar{m} \bar{k}_{20}^2 \gamma_{\theta 1}^2 d\bar{r} \quad (16)$$

$$C_{371} = \theta_1 \int_0^{\bar{T}_T} \gamma_{\theta 1} \left[\bar{k}_A^2 \int_{\bar{r}}^{\bar{T}_T} \bar{m} \bar{\xi} d\bar{\xi} \right]' d\bar{r} \quad (17)$$

$$C_{30,1,1} = 2 \int_0^{\bar{T}_1} \gamma_{\theta,1} \gamma'_{w,1} \gamma''_{w,1} (E I_z - E I_y) d\bar{r} \quad (18)$$

$$C_{30,1,0,0} = -2 \int_0^{\bar{T}_1} \gamma_{\theta,1} \gamma'_{v,p} \gamma''_{v,p} (E I_z - E I_y) d\bar{r} \quad (19)$$

$$C_{44,1} = \int_0^{\bar{T}_1} m \bar{h}_{z,0}^2 \gamma_{\theta,1} d\bar{r} \quad (20)$$

$$C_{46,1,1} = \int_0^{\bar{T}_1} \gamma_{\theta,1} \gamma''_{w,1} \gamma''_{v,p} (E I_z - E I_y) d\bar{r} \quad (21)$$

$$C_{56,1,1} = \int_0^{\bar{T}_1} \gamma_{w,1} m \gamma_{\theta,1} \bar{r} d\bar{r} \quad (22)$$

$$C_{57,1,1} = \int_0^{\bar{T}_1} \gamma_{w,1} \gamma_{\theta,1} \left[\bar{e}_A \int_{\bar{T}}^{\bar{T}_1} m \bar{\xi} d\bar{\xi} - \Delta \bar{e}_{Acw} \int_{\bar{T}_{0cw}}^{\bar{T}} m_{cw} \bar{\xi} d\bar{\xi} \right] d\bar{r} \quad (23)$$

$$C_{60,1} = \int_0^{\bar{T}_1} m \gamma_{w,1} \bar{y}_{10c0} \bar{r} d\bar{r} \quad (24)$$

$$C_{61,1,1} = \int_0^{\bar{T}_1} m \gamma_{w,1} \gamma'_{\theta,1} \bar{y}_{10c0} \bar{r} d\bar{r} \quad (25)$$

$$C_{62,1,1} = \int_0^{\bar{T}_1} m \gamma_{w,1} \gamma_{\theta,1} \bar{y}_{10c0} d\bar{r} \quad (26)$$

$$C_{63,1} = \int_0^{\bar{T}_1} m \gamma_{w,1} \bar{y}_{10c0} d\bar{r} \quad (27)$$

$$C_{64,1,0} = \int_0^{\bar{T}_1} m \gamma_{w,1} \gamma'_{v,p} \bar{y}_{10c0} d\bar{r} \quad (28)$$

$$C_{65,1,1} = \int_0^{\bar{T}_1} \gamma_{w,1} \gamma''_{w,1} \int_{\bar{T}}^{\bar{T}_1} m \bar{y}_{10c0} d\bar{\xi} d\bar{r} \quad (29)$$

$$C_{67,1,1} = \int_0^{T_1} \gamma_{w,1} \gamma_{\theta,1}' \int_r^{T_1} \pi \gamma_{v,p} d\xi d\tau \quad (40)$$

$$C_{68,1,1} = \int_0^{T_1} m \gamma_{w,1} \gamma_{w,1}' (\tau - 0.75) d\tau \quad (41)$$

$$C_{69,1,1} = \int_0^{T_1} m \gamma_{w,1} \gamma_{w,1}' \bar{y}_{10c9} d\tau \quad (42)$$

$$C_{74,1,1} = \int_0^{T_1} m \gamma_{v,p} \bar{y}_{10c9} \gamma_{\theta,1} d\tau \quad (43)$$

$$C_{80,1} = -\theta_1 \int_0^{T_1} m \gamma_{\theta,1} \bar{k}_{z,0}^2 (\tau - 0.75) d\tau \quad (44)$$

$$C_{81,1,p} = \int_0^{T_1} m \gamma_{v,p} \bar{y}_{10c9} \gamma_{w,1}' d\tau \quad (45)$$

$$C_{82,1,1} = \int_0^{T_1} m \bar{k}_{z,0}^2 \gamma_{\theta,1} \gamma_{v,p}' d\tau \quad (46)$$

$$C_{83,1,1} = \int_0^{T_1} \gamma_{\theta,1} m \bar{y}_{10c9} \gamma_{w,1}' d\tau \quad (47)$$

$$C_{84,1,1} = \int_0^{T_1} m \bar{y}_{10c9} \gamma_{\theta,1} \gamma_{w,1}' \tau d\tau \quad (48)$$

$$C_{85,1,1} = \int_0^{T_1} m \bar{y}_{10c9} \gamma_{\theta,1} \tau \gamma_{v,p} d\tau \quad (49)$$

$$C_{86,1,1} = \int_0^{T_1} \gamma_{\theta,1} \gamma_{w,1}'' \left[-\bar{e}_A \int_r^{T_1} m (\bar{\xi} + \bar{e}) d\bar{\xi} + \Delta \bar{e}_{A,cw} \int_{T_{0,cw}}^T m_{cw} (\bar{\xi} + \bar{e}) d\bar{\xi} \right] d\tau \quad (50)$$

$$C_{87,1,1} = \int_0^{T_1} \gamma_{\theta,1} \gamma_{v,p}' \left[-\bar{e}_A \int_r^{T_1} m \bar{\xi} d\bar{\xi} + \Delta \bar{e}_{A,cw} \int_{T_{0,cw}}^T m_{cw} \bar{\xi} d\bar{\xi} \right] d\tau \quad (51)$$

$$C_{88,1,1} = \int_0^{T_1} \gamma_{\theta,1} \gamma_{w,1}'' \left[-\theta_A \int_0^{\bar{T}} \bar{m} \bar{\xi} d\bar{\xi} + \Delta \bar{z}_{A_{cw}} \int_0^{\bar{T}} \bar{m}_{cw} \bar{\xi} d\bar{\xi} \right] d\bar{T} \quad (42)$$

$$C_{92,1} = \int_0^{T_1} \bar{m} \bar{y}_{10c9} \gamma_{\theta,1} d\bar{T} \quad (43)$$

$$C_{93,1} = \int_0^{T_1} \bar{m} \bar{y}_{10c9} \gamma_{\theta,1} \bar{T} d\bar{T} \quad (44)$$

$$C_{94,1} = \theta_1 \int_0^{T_1} \bar{m} \bar{y}_{10c9} \gamma_{\theta,1} \bar{T} (\bar{T} - 0.75) d\bar{T} \quad (45)$$

$$C_{95,1} = \theta_1 \int_0^{T_1} \bar{m} \bar{y}_{10c9} \gamma_{\theta,1} \gamma_{w,1} (\bar{T} - 0.75) d\bar{T} \quad (46)$$

$$C_{96} = \int_0^{T_1} \bar{m} \bar{y}_{10c9} d\bar{T} \quad (47)$$

$$C_{97} = \int_0^{T_1} \bar{m} \bar{T} \bar{y}_{10c9} d\bar{T} \quad (48)$$

$$C_{110,1,1} = \int_0^{T_1} \bar{m} \bar{k}_{z,10}^2 \gamma_{\theta,1} \gamma_{w,1}' d\bar{T} \quad (49)$$

$$C_{111,1,1} = \int_0^{T_1} \bar{m} \bar{y}_{10c9} \gamma_{\theta,1} \gamma_{w,1}' \gamma_{v,1} d\bar{T} \quad (50)$$

$$C_{112,1,1} = \int_0^{T_1} \bar{m} \bar{y}_{10c9} \gamma_{\theta,1} \gamma_{w,1} \gamma_{w,1}' d\bar{T} \quad (51)$$

$$C_{113,1,1} = \int_0^{T_1} \bar{m} \bar{y}_{10c9} \gamma_{\theta,1} \gamma_{\theta,1}' \bar{T} d\bar{T} \quad (52)$$

$$C_{114,1,1} = \theta_1 \int_0^{T_1} \bar{m} \bar{y}_{10c9} \gamma_{\theta,1} \gamma_{v,1} (\bar{T} - 0.75) d\bar{T} \quad (53)$$

The nondimensional aerodynamic twisting moment $(M_A)_{z_0}$ and the nondimensional aerodynamic shearing force $(S_A)_{z_0}$ appear in the above equations, and are pertinent to the static divergence analysis. The expressions for these quantities are given as Eqs. (141) and (146) in Volume I of this report. They are reproduced below as Eqs. (54) and (55).

$$(S_A)_{z_0} = \frac{1}{2} \left(\frac{\rho R^2}{m_0} \right) \bar{c} \left(\frac{U}{\Omega R} \right)^2 (c_l \cos \phi + c_d \sin \phi) \quad (54)$$

$$\begin{aligned} (M_A)_{z_0} = \frac{1}{2} \left(\frac{\rho R^2}{m_0} \right) \left\{ \bar{c}^2 \left(\frac{U}{\Omega R} \right)^2 c_{m_{\frac{1}{2}}} - \frac{\pi}{4} \left(\frac{U}{\Omega R} \right) \bar{c}^3 \Theta \left(\frac{1}{2} - a_0 \right) \right. \\ \left. + \bar{\gamma}_{10 \frac{1}{2}} \bar{c} \left(\frac{U}{\Omega R} \right)^2 \left[\cos \Theta (c_l \cos \phi + c_d \sin \phi) \right. \right. \\ \left. \left. - \sin \Theta (c_l \sin \phi - c_d \cos \phi) \right] \right\} \quad (55) \end{aligned}$$

The angle Θ is given by Eqs. (147) through (149) of Volume I. The mathematical definition of Θ is reproduced below as Eq. (56).

$$\begin{aligned} \Theta = \theta_{.75R} - A_{18} \cos \psi - B_{18} \sin \psi - \tan \delta_3 [\beta + (W'_0)_{r=0}] \\ + \theta_1 (\xi + \tau - 0.75) + \theta_0 \quad (56) \end{aligned}$$

The angle ϕ is the local angle between the plane of rotor rotation and the local resultant velocity vector, as shown in Figure 5 of Volume I.

In accordance with assumptions 3 and 7 of this volume, which were given on page 5, Eq. (56) becomes

$$\Theta = \theta_0 - \beta \tan \delta_3 \quad (57)$$

Note that δ_3 does not exist for the nonarticulated blade.

In accordance with assumption 2, Eq. (57) becomes

$$\Theta = \gamma_{\theta, q_{\theta}} - \beta \tan \delta_3 \quad (58)$$

As in Figure 5 of Volume I,

$$\alpha_r = \alpha + \phi \quad (59)$$

In accordance with assumptions 4 and 8, and through the use of Eq. (58) and (59)

$$(C_l \cos \phi + C_d \sin \phi) = \sigma(\gamma_\theta, q_\theta, -\beta \tan \theta_s + \phi) \quad (60)$$

is obtained for conventional flow. For reverse flow,

$$(C_l \cos \phi + C_d \sin \phi) = -\sigma(\gamma_\theta, q_\theta, -\beta \tan \theta_s + \pi - \phi) \quad (61)$$

is obtained in the same way.

When Eq. (60) or (61) is substituted in Eq. (54), the expression for the nondimensional flatwise aerodynamic shear force for conventional flow becomes

$$(\bar{S}_A)_{z_0} = \frac{1}{2} \left(\frac{\rho R^2}{m_0} \right) \bar{c} \left(\frac{U}{\Omega R} \right)^2 \sigma(\gamma_\theta, q_\theta, -\beta \tan \theta_s + \phi) \quad (62)$$

and

$$(\bar{S}_A)_{z_0} = -\frac{1}{2} \left(\frac{\rho R^2}{m_0} \right) \bar{c} \left(\frac{U}{\Omega R} \right)^2 \sigma(\gamma_\theta, q_\theta, -\beta \tan \theta_s + \pi - \phi) \quad (63)$$

for reverse flow.

For conventional flow, and in accordance with assumptions 4, 5, and 8,

$$C_{m_{c/a}} = 0 \quad (64)$$

for reverse flow,

$$C_{m_{c/a}} = -C_l/2 \quad (65)$$

When Eq. (60) and (64) or (61) and (65) are used in Eq. (55), and consideration is given to assumptions 1, 5, and 7, the expression for the non-dimensional aerodynamic twisting moment becomes

$$(\overline{M}_A)_{x_0} = \frac{1}{2} \left(\frac{\rho R^2}{M_0} \right) \left\{ \overline{y}_{10} c_{\Delta} \overline{C} \left(\frac{U}{\Omega R} \right)^2 \alpha (\gamma_{\theta}, q_{\theta}, -\beta \tan \delta_s + \phi) \right\} \quad (66)$$

for conventional flow, and

$$\begin{aligned} (\overline{M}_A)_{x_0} = \frac{1}{2} \left(\frac{\rho R^2}{M_0} \right) \left\{ \overline{C}^2 \left(\frac{U}{\Omega R} \right)^2 \frac{\alpha}{2} (\gamma_{\theta}, q_{\theta}, -\beta \tan \delta_s + \pi - \phi) \right. \\ \left. - \overline{y}_{10} c_{\Delta} \overline{C} \left(\frac{U}{\Omega R} \right)^2 \alpha (\gamma_{\theta}, q_{\theta}, -\beta \tan \delta_s + \pi - \phi) \right\} \end{aligned} \quad (67)$$

for reverse flow.

Eq. (67) can be written in the following form by collecting terms.

$$(\overline{M}_A)_{x_0} = \frac{1}{2} \left(\frac{\rho R^2}{M_0} \right) \left\{ \left(\frac{U}{\Omega R} \right)^2 \left(\frac{\overline{C}}{2} - \overline{y}_{10} c_{\Delta} \right) \overline{C} \alpha (\gamma_{\theta}, q_{\theta}, -\beta \tan \delta_s + \pi - \phi) \right\} \quad (68)$$

In accordance with assumption 8,

$$\phi \cong \tan \phi = \frac{U_p}{U_T} \quad (69)$$

for conventional flow, and

$$\pi - \phi \cong \tan(\pi - \phi) = -\frac{U_p}{U_T} \quad (70)$$

for reverse flow.

The expression for $U_T/\Omega R$ is given as Eq. (139) of Volume I. When all dynamic terms are eliminated in accordance with assumption 1, the following expression is obtained.

$$\begin{aligned} \frac{U_T}{\Omega R} = & \mu \left[\left(1 - \frac{\beta^2}{2}\right) \sin \psi + \delta \cos \psi \right] + \bar{\epsilon} + \tau \left(1 - \frac{\beta^2}{2}\right) - \bar{y}_{10\ 3C/4} \bar{V}_e' \\ & - \beta \left[\bar{W}_e \cos \theta + (\bar{V}_e + \bar{y}_{10\ 3C/4}) \sin \theta \right] \\ & + (\bar{W}_e' \sin \theta - \bar{V}_e' \cos \theta) \left[-\mu (\cos \psi - \delta \sin \psi) - \lambda_s \beta - \bar{y}_{10\ 3C/4} \cos \theta \right] \\ & - \theta' \left[\bar{V}_e \sin \theta + \bar{W}_e \cos \theta \right] \mu \cos \psi \end{aligned} \quad (71)$$

For this static divergence analysis, using assumptions 7 and 3,

$$\theta = -\beta \tan \delta_s \quad (72)$$

$$\theta' = 0 \quad (73)$$

When assumptions 2 and 7 are used on Eq. (71), considering Eqs. (72) and (73),

$$\frac{U_T}{\Omega R} = \mu \sin \psi + \bar{\epsilon} + \tau \quad (74)$$

The expression for $U_P/\Omega R$ is given by Eq. (140) of Volume I. When all dynamic terms are eliminated in accordance with assumption 1, the following expression is obtained.

$$\begin{aligned} \frac{U_P}{\Omega R} = & \lambda_s \left(1 - \frac{\beta^2}{2}\right) - \mu \beta (\cos \psi - \delta \sin \psi) - \beta \left[(\bar{V}_e + \bar{y}_{10\ 3C/4}) \cos \theta - \bar{W}_e \sin \theta \right] \\ & + (\bar{W}_e' \cos \theta + \bar{V}_e' \sin \theta) \left[-\mu (\cos \psi - \delta \sin \psi) - \lambda_s \beta - \bar{y}_{10\ 3C/4} \cos \theta \right] \\ & - \theta' \mu \cos \psi (\bar{V}_e \cos \psi - \bar{W}_e \sin \psi) \end{aligned} \quad (75)$$

When assumptions 2 and 7, and Eqs. (72) and (73) are employed with Eq. (75), the following simplified expression for $U_P/\Omega R$ results.

$$\frac{U_P}{\Omega R} = \lambda_s - \mu \beta \cos \psi - \beta \bar{y}_{10\ 3C/4} - \mu \bar{W}_e' \cos \psi - \bar{y}_{10\ 3C/4} \bar{W}_e' \quad (76)$$

The terms containing $\gamma_{10sc/4}$ in Eq. (76) are small, and will be neglected in the remaining development.

When Eq. (76) is used with Eqs. (69) and (70) and assumption 6 in Eqs. (62) and (63), the following expressions result.

The expression for conventional flow is

$$(\bar{S}_A)_{z_s} = \frac{1}{2} \left(\frac{\rho R^2}{m_0} \right) \bar{C} \left[\left(\frac{U_T}{\Omega R} \right)^2 \alpha (\gamma_{\theta_1} q_{\theta_1} - \beta \tan \delta_s) + \left(\frac{U_T}{\Omega R} \right) \alpha (\lambda_s - \mu \beta \cos \psi - \mu \bar{W}_e' \cos \psi) \right] \quad (77)$$

The expression for reverse flow is

$$(\bar{S}_A)_{z_s} = -\frac{1}{2} \left(\frac{\rho R^2}{m_0} \right) \bar{C} \left[\left(\frac{U_T}{\Omega R} \right)^2 \alpha (\gamma_{\theta_1} q_{\theta_1} - \beta \tan \delta_s) - \left(\frac{U_T}{\Omega R} \right) \alpha (\lambda_s - \mu \beta \cos \psi - \mu \bar{W}_e' \cos \psi) \right] \quad (78)$$

When Eqs. (69), (70), (76), and assumption 6 are used in Eqs. (66) and (68), the following expressions result:

The expression for conventional flow is

$$(\bar{M}_A)_{x_s} = \frac{1}{2} \left(\frac{\rho R^2}{m_0} \right) \bar{C} \alpha \gamma_{10c/4} \left[\left(\frac{U_T}{\Omega R} \right)^2 (\gamma_{\theta_1} q_{\theta_1} - \beta \tan \delta_s) + \left(\frac{U_T}{\Omega R} \right) (\lambda_s - \mu \beta \cos \psi - \mu \bar{W}_e \cos \psi) \right] \quad (79)$$

The expression for reverse flow is

$$(\bar{M}_A)_{x_s} = \frac{1}{2} \left(\frac{\rho R^2}{m_0} \right) \bar{C} \alpha \left(\frac{\bar{C}}{2} - \gamma_{10c/4} \right) \left[\left(\frac{U_T}{\Omega R} \right)^2 (\gamma_{\theta_1} q_{\theta_1} - \beta \tan \delta_s) - \left(\frac{U_T}{\Omega R} \right) (\lambda_s - \mu \beta \cos \psi - \mu \bar{W}_e' \cos \psi) \right] \quad (80)$$

The algebraic sign of U_T as given by Eq. (74) determines whether a particular blade section is in conventional or reverse flow. If $U_T \geq 0$ the blade section is in conventional flow. If $U_T < 0$ the blade section is in reverse flow. Therefore a single expression can replace Eqs. (77) and (78), through the use of the absolute value of U_T . This expression is

$$(\bar{S}_A)_{z_s} = \frac{1}{2} \left(\frac{\rho R^2}{m_0} \right) \bar{C} \alpha \left[\frac{U_T |U_T|}{(\Omega R)^2} (\gamma_{\theta_1} q_{\theta_1} - \beta \tan \delta_s) + \left(\frac{|U_T|}{\Omega R} \right) (\lambda_s - \mu \beta \cos \psi - \mu \bar{W}_e' \cos \psi) \right] \quad (81)$$

Similar considerations can be used to provide a single expression for $(\bar{m}_A)_{x_s}$, also valid in both forward and reverse flow, from Eqs. (79) and (80). This expression is

$$(\bar{m}_A)_{x_s} = \frac{1}{2} \left(\frac{\rho R^2}{m_0} \right) \bar{C}_0 \bar{V}_{AC} \left[\frac{U_T |U_T|}{(\Omega R)^2} (\gamma_{\theta_1} q_{\theta_1} - \beta \tan \delta_s) + \left(\frac{|U_T|}{\Omega R} \right) (\lambda_s - \mu \beta \cos \psi - \mu \bar{W}_e' \cos \psi) \right] \quad (82)$$

Where the quantity \bar{V}_{AC} is given by

$$\bar{V}_{AC} = \bar{V}_{AC/A} - \frac{\bar{C}}{2} \left(\frac{U_T - |U_T|}{2U_T} \right) \quad (83)$$

The flatwise bending modal equation was presented in this volume as Eq. (1). This equation is now simplified by using assumptions 1, 2, 3, 7, and 8 listed on page 5. The resulting equation is

$$0 = \left(\int_0^{l_T} \gamma_{w_1} (\bar{S}_A)_{z_s} d\bar{r} \right) - C_{11} (q_{w_1} \bar{\omega}_{w_1}^2) + q_{\theta_1} (C_{57,1,1} - C_{62,1,1} - C_{61,1,1}) - C_{10,1} (\bar{q}_{z_s}) \quad (84)$$

The $C_{57,1,1}$ modal constant accounts for spar centroid to elastic axis distance, and tip supported counterweight effects. This modal constant is small and is therefore deleted hereafter.

The torsional modal equation was presented in this volume as Eq. (2). This equation is now simplified by using assumptions 1, 2, 3, 7, and 8 on page 5. The resulting equation is

$$0 = \left(\int_0^{l_T} \gamma_{\theta_1} (\bar{m}_A)_{x_s} d\bar{r} \right) + C_{37,1} + C_{60,1} - C_{36,1} q_{\theta_1} \bar{\omega}_{\theta_1}^2 - C_{44,1} [-\beta \tan \delta_s] + q_{w_1} [-C_{66,1,1} - 8C_{63,1,1} - C_{64,1,1}] - C_{92,1} [8\beta + \bar{q}_{z_s}] - C_{93,1} [\beta] \quad (85)$$

The $C_{\theta\theta}$ modal constant accounts for spar centroid to elastic axis distance and tip supported counterweight effects. This constant is small, and is omitted from the following development. The term involving $C_{\theta\theta}$ is also small, and is deleted in the following development. This term reflects the steady centrifugal twisting couple due to blade flapping when pitch-flap coupling is present.

The flap angle equation was presented in this volume as Eq. (3). This equation is now simplified by using assumptions 1, 2, 3, 7 and 8 of page 5. The resulting equation is

$$\begin{aligned}
 0 = & \left(\int_0^{r_T} (\bar{S}_A)_{z_0} r dr \right) - \bar{M}_0 r_{c0} (\bar{\theta}\beta + \bar{\theta}_{z_0}) - I_0 \beta \\
 & + C_{\theta\theta} \beta \tan \delta_3 + C_{\theta\theta} \bar{\theta} \beta \tan \delta_3 \\
 & + q_\theta (\gamma_{\theta_1}')_{\bar{r}_0} \bar{G} J_0 \tan \delta_3
 \end{aligned} \tag{86}$$

The terms containing $C_{\theta\theta}$ and $C_{\theta\theta}$ are small compared to the others, and will therefore be neglected hereafter.

When the articulated blade is considered in accordance with assumption 3 of page 5, the following equation results from the substitution of Eq. (82) in Eq. (85):

$$\begin{aligned}
 & \left\{ \left(\frac{\rho R^2}{2m_0} \right) \int_0^{r_T} \gamma_{\theta_1}^2 \bar{\gamma}_{ac} \bar{C}_0 \frac{U_T |U_T|}{(\Omega R)^2} dr - C_{\theta\theta} \bar{\omega}_{\theta_1}^2 \right\} q_{\theta_1} \\
 & - \left\{ \left(\frac{\rho R^2}{2m_0} \right) \tan \delta_3 \int_0^{r_T} \gamma_{\theta} \bar{\gamma}_{ac} \bar{C}_0 \frac{U_T |U_T|}{(\Omega R)^2} dr \right. \\
 & \left. + \frac{\rho R^2}{2m_0} \mu \cos \psi \int_0^{r_T} \gamma_{\theta_1} \bar{\gamma}_{ac} \bar{C}_0 \frac{|U_T|}{\Omega R} dr + \bar{\theta} C_{\theta\theta} + C_{\theta\theta} \right\} \beta \\
 & = -C_{\theta\theta} - C_{\theta\theta} + C_{\theta\theta} \bar{\theta}_{z_0} - \left(\frac{\rho R^2}{2m_0} \right) \lambda_0 \int_0^{r_T} \gamma_{\theta_1} \bar{\gamma}_{ac} \bar{C}_0 \frac{|U_T|}{\Omega R} dr
 \end{aligned} \tag{87}$$

When the articulated blade is again considered in accordance with assumption 3 on page 5, the following equation results from the substitution of Eq. (81) in Eq. (86),

$$\begin{aligned}
& \left\{ \left(\frac{\rho R^2}{2m_0} \right) \int_0^{r_1} r \bar{C}_0 \gamma_{\theta_1} \frac{U_T |U_T|}{(\Omega R)^2} dr - (\gamma_{\theta_1}')_{PR} \bar{G}_{10} \tan \delta_3 \right\} q_{\theta_1} \\
& - \left\{ \left(\frac{\rho R^2}{2m_0} \right) \tan \delta_3 \int_0^{r_1} r \bar{C}_0 \frac{|U_T|}{(\Omega R)^2} dr \right. \\
& \left. + \left(\frac{\rho R^2}{2m_0} \right) \mu \cos \psi \int_0^{r_1} r \bar{C}_0 \frac{|U_T|}{\Omega R} dr + \bar{M}_0 r_{cg} \bar{e} + \bar{I}_0 \right\} \beta \\
& = - \left(\frac{\rho R^2}{2m_0} \right) \lambda_3 \int_0^{r_1} r \bar{C}_0 \frac{|U_T|}{\Omega R} dr + \bar{M}_0 r_{cg} \bar{q}_{z_0} \quad (88)
\end{aligned}$$

Then the procedure used to obtain Eqs. (87) and (88) is repeated for the nonarticulated blade, Eq. (82) is substituted in Eq. (85), and Eq. (81) is substituted in Eq. (84). The following pair of equations result.

$$\begin{aligned}
& \left\{ \frac{\rho R^2}{2m_0} \int_0^{r_1} \gamma_{\theta_1}^2 \bar{Y}_{Ac} \bar{C}_0 \frac{U_T |U_T|}{(\Omega R)^2} dr - C_{36,1} \bar{\omega}_{\theta}^2 \right\} q_{\theta_1} \\
& - \left\{ \frac{\rho R^2}{2m_0} \mu \cos \psi \int_0^{r_1} \gamma_{\theta_1} \gamma_{w_1}' \bar{Y}_{Ac} \bar{C}_0 \frac{U_T}{\Omega R} dr + \bar{e} C_{33,1} - C_{34,1,1} \right\} q_{w_1} \\
& = - \frac{\rho R^2}{2m_0} \lambda_3 \int_0^{r_1} \gamma_{\theta_1} \bar{Y}_{Ac} \bar{C}_0 \frac{|U_T|}{\Omega R} dr - C_{37,1} - C_{30,1} + C_{32,1} \bar{q}_{z_0} \\
& \quad (89)
\end{aligned}$$

$$\begin{aligned}
& \left\{ \frac{\rho R^2}{2m_0} \int_0^{r_T} \gamma_{\theta_1} \gamma_{w_1} \bar{c}_0 \frac{u_T |u_T|}{(\Omega R)^2} d\bar{r} - C_{e1,1,1} - C_{e2,1,1} \right\} q_{\theta_1} \\
& - \left\{ \frac{\rho R^2}{2m_0} \mu \cos \psi \int_0^{r_T} \gamma_{w_1} \gamma_{w_1}' \bar{c}_0 \frac{|u_T|}{\Omega R} d\bar{r} + C_1 \bar{\omega}_{w_1}^2 \right\} q_{w_1} \\
& = - \frac{\rho R^2}{2m_0} \lambda_3 \int_0^{r_T} \gamma_w \bar{c}_0 \frac{|u_T|}{\Omega R} d\bar{r} + C_{10} \bar{q}_{z_3} \quad (90)
\end{aligned}$$

In the above, the substitution

$$\bar{w}_{\theta_1}' = \gamma_{w_1}' q_{w_1} \quad (91)$$

has been made.

Eqs. (87) and (88) and Eqs. (89) and (90) are two sets of two linear equations each. These equations could be solved for q_{θ_1} and β from Eqs. (87) and (88) for articulated blades, and for q_{θ_1} and q_{w_1} from Eqs. (89) and (90) for nonarticulated blades, if all the other parameters were given. However, the objective is to find conditions for boundaries of static stability. The boundaries of static stability are those sets of conditions for which static equilibrium is present when the right hand sides of Eq. (87) through (90) are zero. It should be noted that the right hand sides of these equations represent steady torsional and flapping or flatwise bending moments, independent of the deflections and consistent with the simplifying assumptions employed. The conditions for a static stability boundary are thus those conditions such that indefinitely large static deflections can occur even though these independently applied steady forces are zero.

In this way, the following pair of equations was obtained for articulated blades:

$$\begin{aligned}
0 = & \left\{ \frac{\rho R^2}{2m_0} \int_0^{r_T} \gamma_{\theta_1}^2 \bar{\gamma}_{AC} \bar{c}_0 \bar{u}_T |\bar{u}_T| d\bar{r} - C_{36} \bar{\omega}_{\theta}^2 \right\} q_{\theta_1} \\
& - \left\{ \frac{\rho R^2}{2m_0} \tan \delta_3 \int_0^{r_T} \gamma_{\theta_1} \bar{\gamma}_{AC} \bar{c}_0 \bar{u}_T |\bar{u}_T| d\bar{r} \right. \\
& \left. + \frac{\rho R^2}{2m_0} \mu \cos \psi \int_0^{r_T} \gamma_{\theta_1} \bar{\gamma}_{AC} \bar{c}_0 |\bar{u}_T| d\bar{r} + \bar{e} C_{92} + C_{93} \right\} \beta \quad (92)
\end{aligned}$$

$$\begin{aligned}
0 = & \left\{ \frac{\rho R^2}{2m_0} \int_0^{r_1} r \bar{c}_a \gamma_\theta \bar{u}_r |\bar{u}_r| dr - (\gamma_{\theta_1}')_{\text{PR}} \tan \delta_3 \bar{\omega}_0 \right\} q_{\theta_1} \\
& - \left\{ \frac{\rho R^2}{2m_0} \tan \delta_3 \int_0^{r_1} r \bar{c}_a \bar{u}_r |\bar{u}_r| dr \right. \\
& \left. + \frac{\rho R^2}{2m_0} \mu \cos \psi \int_0^{r_1} r \bar{c}_a |\bar{u}_r| dr + M_0 r_{c\theta} \bar{\theta} + I_0 \right\} \beta
\end{aligned} \quad (93)$$

In Eq. (92) and (93), the term $u_r/\Omega R$ has been replaced by \bar{u}_r . This approximation is in consideration of assumptions 2 and 7 on page 5.

In a similar manner, the following pair of equations was obtained for non-articulated blades:

$$\begin{aligned}
0 = & \left\{ \frac{\rho R^2}{2m_0} \int_0^{r_1} \gamma_{\theta_1}^2 \nabla_{ac} \bar{c}_a \bar{u}_r |\bar{u}_r| dr - C_{2\theta} \bar{\omega}_\theta^2 \right\} q_{\theta_1} \\
& - \left\{ \frac{\rho R^2}{2m_0} \mu \cos \psi \int_0^{r_1} \gamma_{\theta_1} \gamma_{w_1}' \nabla_{ac} \bar{c}_a |\bar{u}_r| dr + \bar{\theta} C_{\theta 3} + C_{\theta 4} \right\} q_{w_1}
\end{aligned} \quad (94)$$

$$\begin{aligned}
0 = & \left\{ \frac{\rho R^2}{2m_0} \int_0^{r_1} \gamma_\theta \gamma_w \bar{c}_a \bar{u}_r |\bar{u}_r| dr - C_{\theta 1} - C_{\theta 2} \right\} q_{\theta_1} \\
& - \left\{ \frac{\rho R^2}{2m_0} \mu \cos \psi \int_0^{r_1} \gamma_w \gamma_w' \bar{c}_a |\bar{u}_r| dr + C_1 \bar{\omega}_w^2 \right\} q_{w_1}
\end{aligned} \quad (95)$$

In Eq. (92) through (95),

$$\bar{u}_r \cong \frac{u_r}{\Omega R} \quad (96)$$

$$\bar{u}_r = \bar{\theta} + \bar{r} + \mu \sin \psi \quad (97)$$

$$\overline{GJ}_0 = GJ_0 / m_0 (\Omega R^2)^2 \quad (98)$$

$$\overline{I}_0 = \int_0^{l_1} m r^2 dr \quad (99)$$

$$\overline{M}_0 \overline{r}_{c0} = \int_0^{l_1} m r dr \quad (100)$$

In further developments, the following more convenient notation will be used for the distance from the elastic axis to the center of gravity:

$$\overline{Y}_{c0} = \overline{Y}_{0c0} \quad (101)$$

In the case of an articulated rotor, the determinant of the two homogeneous equations (92) and (93) is formed and evaluated for many values of advance ratio μ , with all other input being held constant. The value of μ for which this determinant is zero is found within the desired degree of approximation by a computer trial-and-error procedure. This value of μ is considered to be the value at which torsional divergence occurs. The process is similar with a nonarticulated rotor except that Eq. (94) and (95) are used.

TORSIONAL DIVERGENCE DESIGN CHARTS

DISCUSSION

The limits on rotor operating conditions imposed by blade torsional divergence have been studied extensively by means of the relatively simple method described above.

A fairly large number of parameters have been selected for this study, with various combinations being chosen to be of maximum future use in the preliminary evaluation of new blade designs. Design charts have been generated to facilitate such evaluations without performing new calculations.

The various parameters originally chosen to be varied were as follows:

1. Blade inertia ratio, $m_0 k_r^2 / \rho C_0 e_0 R^2$.
2. Control system spring ratio, $K_r L_B / GJ_0$.
3. Blade frequency parameter, $GJ_0 / m_0 k_r^2 (\Omega R)^2$
4. Blade chord distribution.
5. Blade torsional stiffness distribution.
6. Blade pitching inertia distribution.
7. Blade average lift-curve slope.
8. Aerodynamic root cutout.
9. Blade center-of-gravity distribution.

In addition to the above, the effect of blade lift-curve slope spanwise variation caused by Mach number effects was investigated. The effects of pitch-flap coupling were evaluated, and calculations were carried out for nonarticulated blade designs.

Blade designs with uniform chord, mass and stiffness properties were used in order to obtain design charts for the effects on torsional divergence boundaries of control system flexibility, aerodynamic root cutout, and center-of-gravity position. The independent effects of the other parameters mentioned above were studied with additional calculations. The various charts and pertinent assumptions used in their preparation are described in this subsection. The significance of the simple energy analysis results and the permissible analytical assumptions and preliminary design procedures are given later under the appropriate subsections, after the Normal Mode Transient Analysis results have been presented.

The inertia distribution is included as a parameter in this study, even though the static stability calculation does not, strictly speaking, consider inertial effects as such. The natural vibration mode is used as an assumed divergence mode; thus, inertial effects on the divergence calculation are actually a reflection of changes in mode shape. Certain unpublished preliminary results have indicated that correct trends are predicted by using the natural mode shape in this manner.

It is instructive to consider the differential equation of torsional static deflection of a rotor blade. This differential equation expresses the equilibrium of static elastic and aerodynamic torsional couples on an infinitesimal spanwise increment:

$$\frac{d}{dr} \left(GJ \frac{d\theta}{dr} \right) = -q C_l C_e = -q a_0 C_\theta \quad (102)$$

It is assumed that the blade is uniform, with properties of the reference 75% radius. Then the differential equation is

$$GJ \frac{d^2\theta}{dr^2} = -q C_l C_e = -q a_0 C_\theta \quad (103)$$

The symmetrical blade is assumed to be operating at zero angle of attack, except for the angle caused by the torsional deflection.

The dynamic pressure q due to velocity components normal to the radius is given by the following:

$$q = \frac{\rho}{2} (\Omega r + V \sin \psi)^2 = \frac{\rho}{2} (x + \mu \sin \psi)^2 (\Omega R)^2 \quad (104)$$

Nondimensionalizing and using Eq. (104) in Eq. (103) gives

$$\frac{GJ_0}{R^2} \frac{d^2\theta}{dr^2} = -\frac{\rho}{2} (x + \mu \sin \psi)^2 (\Omega R)^2 a_0 C_\theta \left(\frac{r}{R} \right) \theta \quad (105)$$

For the case where $\psi = 270^\circ$, and with $\mu \geq 1$, reverse flow exists over the entire span, and a_0/C_θ equals 0.5 for the normal 25% chord center-of-gravity and elastic axis positions.

Thus, the differential equation becomes

$$\frac{d^2\theta}{dx^2} = -\frac{\rho}{4} \frac{a_0 C_\theta^2 \Omega^2 R^4}{GJ_0} (x - \mu)^2 \theta \quad (106)$$

$$\frac{d^2\theta}{dx^2} = -\frac{(x-\mu)^2}{2S_n} \theta \quad (107)$$

The nondimensional parameter S_n is defined by

$$S_n = \frac{2GJ_p}{\rho a_0 C_p \Omega^2 R^4} \quad (108)$$

Rigorous satisfaction of the above differential equation, assuming $\mu \geq 1$, is provided by the following infinite series:

$$\begin{aligned} \theta = & p_0 \sum_{n=1}^{\infty} \left[\frac{(x-\mu)^{4n}}{(2S_n)^n (4n)(4n-1)(4n-4)(4n-5)(4n-8)(4n-9) \cdots (4)(3)} \right] \\ & + p_1 \sum_{n=1}^{\infty} \left[\frac{(x-\mu)^{4n+1}}{(2S_n)^n (4n+1)(4n)(4n-3)(4n-4)(4n-7)(4n-8) \cdots (5)(4)} \right] \end{aligned} \quad (109)$$

The series given as Eq. (109) converges fairly rapidly, so only a few terms need be used for numerical evaluations.

The appropriate boundary conditions for the blade fixed at the root are

$$\theta = 0 \quad \text{when} \quad x = 0 \quad (110)$$

$$\frac{d\theta}{dx} = 0 \quad \text{when} \quad x = 1 \quad (111)$$

Use of these with Eq. (109) provides two homogeneous equations. Setting the determinant equal to zero provides a characteristic equation in $1/S_n$ if μ is given. The lowest value of $1/S_n$ which makes the determinant zero is the critical value of interest. When this has been found, the value of p_1 in terms of p_0 can be found by using one of the boundary conditions. The above procedure was carried out for $\mu = 1$ with the results shown in Figure 1 and with a solution for critical $S_n = .031$. Also shown for comparison is the uniform blade natural vibration mode.

The digital computer was used to predict a divergence advance ratio, using Eq. (92) and (93) as described previously. The first natural torsional vibration mode was used in these calculations. With a value of $S_n = .031$, the predicted value of critical advance ratio was $\mu = 1.03$, compared with $\mu = 1.0$ for the differential equation solution. This demonstrated that the use of a natural vibration mode as a divergence mode is a good simplifying assumption, even for advance ratios near unity.

The most important conclusion to be drawn from the above, however, is that the advance ratio μ , and the torsional stiffness coefficient S_a , are the basic parameters for the study of retreating uniform blade static torsional divergence. The same parameters also arise from inspection of a single-degree-of-freedom energy analysis, where S_a appears as a parameter along with the nondimensional integrals of strain energy and virtual work. The parameter S_a is also the product of blade inertia ratio and frequency parameter, divided by average lift-curve slope. These parameters are among those listed at the beginning of this section. Variations in these parameters are included as variations in the more basic S_a parameter. The numerical value of S_a for a typical rotor blade operating at design tip speed is approximately 0.040.

The parameter S_a has been developed with a 50% chord distance between the aerodynamic center of pressure and the center of gravity, which is coincident with the elastic axis. This is appropriate to the usual retreating blade case.

The usefulness of attempting the definition of a parameter even more generally applicable than S_a has been examined. Specifically, Eq. (106) can be rewritten, retaining the nondimensional distance between the aerodynamic center of pressure and the center of gravity, which is coincident with the elastic axis.

$$\frac{d^2\theta}{dz^2} = -(1 + \mu \sin\psi)^2 \frac{\rho}{2} \left(\frac{e_0}{C_0} \right) \frac{e_0 C_0^2 \Omega^2 R^4}{GJ_0} \theta \quad (112)$$

It is evident from consideration of the right hand side of Eq. (102) that divergence will first appear, as aircraft forward speed increases, at that azimuth angle where the coefficient of θ reaches a maximum absolute value. From Eq. (104) it can be seen that two particular azimuth angles are of primary interest; these are $\psi = 90^\circ$ and $\psi = 270^\circ$. Note that the value of e_0/C_0 is, in general, different at these two azimuth angles. For $\psi = 90^\circ$, for example

$$\frac{e_0}{C_0} = \bar{V}_{ce} \quad (113)$$

while for $\psi = 270^\circ$, and $\mu \geq 1$,

$$\frac{e_0}{C_0} = .50 + \bar{V}_{ce} \quad (114)$$

where \bar{V}_{ce} is constant along the blade radius. When only the two specific azimuth angles $\psi = 90^\circ$ and $\psi = 270^\circ$ are considered, Eq. (112) has two possible forms. These are

$$\frac{d^2\theta}{dx^2} = -\frac{\rho}{2} \left(\frac{e_0}{C_0} \right) \frac{a_0 C_0^2 \Omega^2 R^4}{GJ_0} (x + \mu)^2 \theta \quad (115)$$

for $\psi = 90^\circ$ and

$$\frac{d^2\theta}{dx^2} = -\frac{\rho}{2} \left(\frac{e_0}{C_0} \right) \frac{a_0 C_0^2 \Omega^2 R^4}{GJ_0} (x - \mu)^2 \theta \quad (116)$$

for $\psi = 270^\circ$. It might be concluded from the above that the coefficient of $(x + \mu)^2 \theta$ and $(x - \mu)^2 \theta$ in the above equations is the most general parameter. This would be true if only advance ratios greater than unity were of interest. For advance ratios $\mu < 1$, the above simple concepts are not true even for a uniform blade, since e_0/C_0 will vary radically between the inboard portions of the blade where reverse flow is present, and the outboard portions where conventional flow is present. An effective value of e_0/C_0 might be defined, but this itself would be a function of advance ratio. Therefore it is advantageous to accept the S_n parameter as the basic parameter, and consider variations in e_0/C_0 through the generation of both advancing and retreating blade stability boundaries, and through the treatment of \bar{Y}_{c_0} as an independent parameter.

The energy analysis described during the development of Eq. (92) through (95) introduces a flapping or bending degree of freedom to the torsional divergence analysis. This accounts for the fact that blade static torsional stability always involves some blade flapping due to lift caused by torsional deflection. The resistance to flapping of conventional rotor blades is provided mainly by a centrifugal force component which acts at the blade chordwise center of mass.

If the center of mass does not coincide with the aerodynamic center the resulting couple causes potentially divergent torsional deflections. At azimuth angles of 270° and 90° , the results for articulated blades with no pitch-flap coupling are practically identical with single-degree-of-freedom analyses if the torsional couple caused by the distance between the aerodynamic center and the center of mass is considered.

The uniform blade design charts, Figures 2, 3, and 4, were produced for a completely uniform blade with a chord-to-radius ratio of 0.050 and negligible flapping hinge offset. The value of mass ratio M_r was 11.9. Calculations were carried out for practical variations in this parameter, and divergence results were identical within the reading and data input accuracy. The ratio of the blade torsional radius of gyration to rotor radius was 0.012. The elastic axis was assumed to lie along the 25% chord line. The lift-curve slope was assumed to be constant along the blade span, with no tip loss being considered.

The boundaries were generated by finding the critical advance ratio for 10 different values of nondimensional stiffness coefficient S_R for each of the otherwise identical blade configurations.

Torsional elastic stiffness was changed to vary the nondimensional stiffness. Identical values of torsional stiffness coefficient S_R were generated by changing rotational speed with elastic stiffness held constant, and calculations were carried out to verify that identical values of critical advance ratio would be obtained. Small variations in torsional mode shape due to different rotational speeds were not found to be significant. The effects of rotation on blade torsional stiffness were also unimportant.

The first set of design charts, Figure 2, presents plots of the critical advance ratio μ versus torsional stiffness coefficients S_R for various values of aerodynamic root cutout X_{OA} . Each plot is for constant values of control stiffness parameter, $1/K$, and chordwise center-of-gravity offset, Y_{CG}/C . These plots are for critical values of μ occurring at azimuth angles of either 270° or 90° . The 90° azimuth torsional divergence occurs only for the aft center-of-gravity positions (negative Y_{CG}/C), and is represented by the branch on the left side of the break in these curves. The divergence boundaries for the 90° azimuth are shown only as they are more critical than the 270° azimuth boundaries, and vice versa. This set of curves will be useful in the evaluation of specific blade designs.

The second set of design charts, Figure 3, presents cross plots of the first set at various constant values of μ and Y_{CG}/C . The values of μ presented are 1.2, 1.4, 1.6, 1.8, and 2.0, which cover the range expected to be of greatest future interest for torsional divergence. Both positive and negative values of Y_{CG}/C are included. The values of Y_{CG}/C are .10, 0, -.02, -.06, and -.10. The reciprocal of the control stiffness ratio K is plotted against S_R at constant values of X_{OA} . This set of curves can be used in trade-off studies concerning the relative benefits of changes in S_R and K . Since Figure 3 is composed of direct cross plots of Figure 2, it also reflects instabilities at azimuth angles of either 90° or 270° , depending on which is most critical.

The third set of design charts, Figure 4, also presents cross plots of the first set, but with Y_{CG}/C plotted against S_R at various constant values of X_{OA} . The values of μ and $1/K$ remain constant for each of these plots. This set of curves can be used in trade-off studies concerning the relative benefits of changes in S_R and Y_{CG}/C . As with Figure 3, the boundaries are shown for azimuth positions of either 90° or 270° , depending on which is most critical. The azimuth angle to which a particular point on any of the boundaries pertains is easily determined by reference to Figure 2.

The independent effects of certain other parameters on the static divergence stability boundaries are shown in Figures 5 through 14. The value of S_R in these cases was determined by using the values of GJ_0 , α_0 , and C_0 existing at the 75% radius. The shapes and frequencies of each of the torsional modes are appropriate to each configuration. The rigid flapping

mode was used for deflections out of the plane of rotation for the articulated rotor. The first flatwise bending mode appropriate to the given values of a parameter $m/\rho_0 C_0^2$, the ratio of torsional to flapwise bending stiffness EI_f/GJ_0 , and the torsional stiffness coefficient S_n was used in the case of the nonarticulated blades. In each case where blade cross-sectional properties were varied separately for this set of charts, they were made equal to the uniform blade properties at the 75% rotor radius. Information as to how the various parameters were varied is contained on the captions and legends for each figure.

The effect on retreating blade torsional divergence of a linearly varying blade chord is shown in Figure 5, for different values of tip-chord-to-root-chord ratio. The chord-to-radius ratio at the 75% radius remained at the value used for the uniform blade, and S_n is also based on this value. All other blade properties remained as for the uniform blades.

The effect of a structural flexibility cutout, X_{0s} on retreating blade torsional divergence is shown in Figure 6. The structural flexibility cutout refers to a torsionally rigid inboard section. Thus, when $X_{0s} = .10$ the inboard 10% radius of the blade is considered to be torsionally rigid. The remainder of the blade is identical to the previously considered uniform blades. The torsional deflection modes used in these calculations are natural vibration modes appropriate to these blades with torsionally rigid inboard sections.

The effect on retreating blade torsional divergence of a linearly varying blade torsional stiffness is shown in Figure 7 for different values of tip-stiffness-to-root-stiffness ratio. The nondimensional stiffness coefficient S_n is defined at the three-quarter radius. The blade torsional deflection modes used in these calculations are the appropriate natural vibration modes. The significance of the small apparent effect of tapering stiffness will be discussed later.

The effect of inertial cutout on retreating blade torsional divergence is shown in Figure 8. Inertial cutout refers to a uniform blade, with an inboard section of negligible torsional inertia. This has an effect on torsional divergence through the use of the natural vibration mode as an assumed divergence mode. Thus, comparison with the completely uniform blades reflects only the effect of the change in mode shape on the static stability calculation. Except for the cutout, the blades were identical to the previously considered uniform blades.

The effect of linearly varying inertia on retreating blade torsional divergence is shown in Figure 9. The inertia was made equal to that for the previously considered uniform blades at the 75% radius, with different ratios of root inertia to tip inertia. Except for the variation in inertia, the blades were identical to the previously considered uniform blades. It should be noted that the effect on the torsional divergence static stability stems only from the alterations in the torsional natural mode shape.

Torsional divergence cases were considered for the retreating blade with spanwise variations in the chordwise center-of-gravity offset position. These included offsets of $Y_{cg}/C = .10$, extending from inboard fractional radii of 0.25 and 0.45 to the tip, and linearly varying offset distances, with Y_{cg}/C equal to 0.10 at the 75% radius. Linearly varying offsets, such that the ratio of root-to-tip offsets was two and three, were chosen and also used in separate sets of divergence calculations. The results for all of these calculations were within 1 percent of the values for the uniform blade; therefore, no separate charts were made.

The next charts, Figures 10 and 11, show the effect of the distribution of Glauert's lift-curve slope correction due to Mach number. The effects on the advancing, as well as on the retreating, blades are shown. The parameter S_c , defined in the table of symbols, is also equal to the parameter S_R , evaluated with a lift-curve slope of 2π , and multiplied by the square of the ratio of rotational tip speed ΩR to the speed of sound. The value of S_R in Figures 10 and 11, however, refers to the value at the 75% radius with the lift-curve slope correction applied. The zero value of S_c refers to the earlier uniform blade cases without Glauert's correction. A 0.0143 value of S_c refers to conventional blade stiffness coefficient and rotational speed under the standard conditions, as typified by the CH-3C rotor. It should be noted that the curves of constant S_c in Figure 10 are very nearly curves of constant advancing blade Mach number at the 75% radius. The advancing blade 75% radius Mach number along the curve $S_c = .0286$ ranges between 0.68 and 0.71.

The next charts, Figures 12 and 13, show the comparative divergence boundaries for articulated and nonarticulated blades, with the nonarticulated uniform blades rigidly built into the hub at the center of rotation. Advancing as well as retreating blade divergence is considered. Note that the nondimensional stiffness concept remains valid for the nonarticulated blades, so long as the ratio $El_f \rho a_0 C_0^2 / m G J_0$ remains constant. This point will be discussed later. The value of $El_f / G J_0$ of 0.548 refers to conventional practice as typified by the CH-3C rotor.

The effect of pitch-flap coupling as predicted by the simple divergence analysis is shown in Figure 14. The effects on the retreating blade only are shown, since pitch-flap coupling will greatly increase advancing blade divergence advance ratio and decrease it for the retreating blade. The effects of pitch-flap coupling were investigated for the articulated blade only, since the provision of an appreciable amount of this type of coupling is mechanically difficult with nonarticulated blades.

TORSIONAL DIVERGENCE CALCULATIONS WITH THE EXTENDED NORMAL MODE TRANSIENT ANALYSIS

DISCUSSION OF PURPOSE AND METHODS

A number of solutions of the flexible blade equations of motion for torsional divergence conditions were accomplished, by use of the extended Normal Mode Transient Analysis. The solutions demonstrate the effect on torsional divergence of blade flatwise and edgewise flexibility, in conjunction with consideration of all significant inertial terms. This was done for coincident and noncoincident section elastic and center-of-gravity axes and for articulated and nonarticulated blades. In addition to this, cases were run at reduced air density, to provide data at higher values of torsional stiffness coefficient S_R . Control system flexibility was also investigated for the articulated blades.

The effects of pitch-flap coupling on the torsional divergence of an articulated blade were calculated, and the effect of a representative system of gyro feedback on a nonarticulated blade was determined.

The solution of the blade equations of motion was generally conducted by starting a typical blade, whose properties are given in Table I and II at an azimuth angle of zero. Collective pitch and inflow were also made equal to zero.

The elastic modes considered for the articulated blades were the first through the third flatwise bending modes, the first edgewise bending mode, and the first torsional mode. These elastic modes were in addition to the rigid blade flapping and lagging modes for the articulated blades. For the nonarticulated blades, the first through the fourth flatwise bending modes, the first and second edgewise bending modes, and the first torsional mode were considered. The solution for blade motion was then obtained for one revolution of the rotor by using the extended Normal Mode Transient Analysis. The values of aircraft forward speed and rotor rotational speed at the various values of advance ratio were chosen by setting the advancing blade tip Mach number equal to 0.85. The aerodynamic data were appropriate to an NACA 0012 airfoil, with Mach number and stall effects included. Rotor shaft angle of attack was set constant at zero degrees. The parameter used to evaluate blade response was one-half peak-to-peak stress variation.

It will be noted that the effect of blade center-of-gravity offset was studied at a constant value of advance ratio, with a collective pitch $\theta_{75\%}$ of 2 degrees and an inflow λ of 0.

This alternate method was necessary to demonstrate the existence of the practical operating limits appropriate to the torsional flexibility of the advancing blade. The excitation of the unloaded advancing blade was found to be very small at the predicted static stability boundary. Extensive penetration of this boundary without important blade response could occur for the completely unloaded rotor. However, the addition of a small load resulted in a torsional stress rise similar to that for the retreating blade.

In view of the objective of correlating the simple energy analysis for torsional divergence with practical operating limits, the advancing blade cases were carried out with the moderate loadings generated by the 2 degree collective pitch setting. One possible explanation for the lack of excitation on the advancing blade is the stabilizing center-of-pressure movement at high subsonic Mach numbers. This would tend to prevent torsional divergence until a relatively large section of the rotor disc, including the lower Mach number areas, is unstable. A small amount of cyclic pitch was used to eliminate rotor pitching and rolling moment for the nonarticulated rotor. The method of solution was otherwise identical to the other Normal Mode Transient Analysis cases for this section, with the starting values for the blade differential equations of motion being given as zero flapping, lagging, and elastic modal displacements and velocities at an azimuth angle ψ of 0 degrees.

The pitch-flap coupling effects were evaluated with the unloaded rotor as described previously. Inclusion of this type of coupling in the calculations is a routine provision of the Normal Mode Transient Analysis.

The study of the effect of a control gyroscope on torsional divergence is much more involved. The scope of this work is such that one typical gyroscope installation could be included. The control gyro parameters of interest are given in the descriptions of configurations to follow.

At this point in the discussion, it is appropriate to outline the manner in which the gyro is assumed to act. Consistent with the remainder of the investigation, no shaft or fuselage motion is included. In addition to the torsional moment, a small component of blade flapping moment at each of the blade roots is reacted by the pushrod, because of a small built-in angle between the blade axis and the feathering axis. This effect has been found to be small for this torsional divergence study, since bending moments are initially small for the unloaded blade. The blade moment about the feathering bearing is provided by the gyro reaction to pushrod force, acting through its moment arm. The gyro motion, and the resulting pitch position input to the blades, depends on the pushrod loads applied by all the blades.

In order to assess the effect of the gyroscope, blade response calculations were first performed with the gyroscope assumed as being fixed to the shaft. The loads on the gyroscope were calculated, and then its response to these loads was calculated. Finally, the gyro response was used to define new cyclic pitch control positions for another blade response calculation. The change in blade response due to the new control positions was then noted. The process could be repeated to improve accuracy, although one cycle was judged to be sufficient for the purposes of this study.

CONFIGURATIONS AND FLIGHT CONDITIONS STUDIED

The pertinent characteristics of the basic rotor system used for torsional divergence studies with the extended Normal Mode Transient Analysis are shown in Table I.

The chord, stiffness, mass, blade center-of-gravity chordwise position, and section properties of the blade are constant, except for the aerodynamic and structural cutouts. The elastic axis was assumed to lie along the 25% chord. The blades had an NACA 0012 airfoil section. The nonarticulated blade was identical to the articulated blade except for the removal of the flap-lag hinge. Control gyro parameters of interest are a lead angle of 1.5° between blade axis and feathering axis, and a gyro polar moment of inertia 0.01 times that of the rotor. The pushrod was assumed to lead the blade feathering axis by an azimuth angle of 45° . No mechanical damping was applied to gyro motion.

The various configurations used for this part of the torsional divergence study with the extended normal mode analysis are shown in Table II.

The various flight conditions used for this part of the study are shown in Table III. The advancing blade tip Mach number remained constant at $M_{t,90} = .85$.

The combinations of configurations and flight conditions are shown in Table IV.

RESULTS OF NORMAL MODE TRANSIENT ANALYSIS CALCULATIONS

Figure 15 shows a three-revolution time history of blade first torsion modal response, after being started with zero collective pitch, cyclic pitch, flapping, lagging and elastic modal displacements and velocities, at an azimuth of zero (directly aft). This figure is for the basic articulated rotor configuration, operating at an advance ratio of 1.6. Note that the retreating blade torsional response is more severe during the first revolution than during the following two, which justifies the use of a single revolution to evaluate peak torsional divergence response.

Figure 16 shows a similar two-revolution time history of blade first torsion modal response, with the 15% chord aft center-of-gravity position, which is the articulated blade configuration 6. The response is calculated with 2 degrees of collective pitch present to supply additional loading, as discussed earlier. Note that in this case the first and second revolution maximum response is virtually identical, again supporting the use of the first revolution to evaluate torsional response for the lightly loaded blade.

Figure 17 shows one-half peak-to-peak stresses calculated during the first revolution after starting the blade at $\psi = 0$, with no initial loadings, at various values of advance ratio. This is for the basic articulated rotor. Also shown is the stability boundary predicted by using Figure 6. Figure 6 was used by finding the intersection of the $X_{05} = .06$ stability boundary and a plot of μ versus S_R appropriate to standard sea level atmospheric conditions and the advancing blade tip Mach number of 0.85. The method of obtaining this relationship will be explained later, under the general discussion of preliminary design methods.

Figure 18 is similar to Figure 17, with calculations carried out at a value of air density ρ at 2/3 of that for standard sea level conditions. This corresponds to an altitude of approximately 13,000 feet.

Figure 19 shows the Normal Mode Transient Analysis one-half-peak-to-peak stress results for the basic rotor with control system flexibility. The effects of control system flexibility on the static torsional divergence of the blade with structural cutout was not determined with the simple analysis, since structural cutout was a parameter whose independent effect was determined. In order to estimate the static divergence boundary for the combined effects of structural cutout and control system flexibility, the independent effects of each were, in effect, superimposed. This procedure is not rigorous in a strict mathematical sense, but is justified by the approximations inherent in the static torsional divergence analysis. The procedure will be described mathematically in the following development. This particular discussion is limited to the case of the blade with uniform spanwise properties except for cutout, in order to present the procedure in as simple a manner as possible.

It can be observed that, in principle, the advance ratio for static divergence can be expressed as a function of all the variables considered.

$$\mu = f(S_R, 1/K, X_{OS}, X_{OA}, \bar{Y}_{CS}) \quad (117)$$

If μ is known for a particular set of values of S_R , $1/K$, X_{OS} , X_{OA} , and \bar{Y}_{CS} , a Taylor's series may be written about that value. The elements of that set are identified below by the "a" subscript.

$$\begin{aligned} \mu \cong \mu_a + \frac{\partial \mu}{\partial S_R} [S_R - S_{Ra}] + \frac{\partial \mu}{\partial (1/K)} \left[\frac{1}{K} - \frac{1}{K_a} \right] + \frac{\partial \mu}{\partial (X_{OS})} [X_{OS} - X_{OSa}] \\ + \frac{\partial \mu}{\partial (X_{OA})} [X_{OA} - X_{OAa}] + \frac{\partial \mu}{\partial \bar{Y}_{CS}} [\bar{Y}_{CS} - \bar{Y}_{CSa}] + \dots \end{aligned} \quad (118)$$

When values of the variables considered above remain suitably close to S_{Ra} , $1/K_a$, X_{OSa} , X_{OAa} , and \bar{Y}_{CSa} , the specific terms appearing in Eq. (118) furnish a satisfactory approximation. The derivatives in Eq. (118) are evaluated at S_{Ra} , $1/K_a$, X_{OSa} , X_{OAa} , and \bar{Y}_{CSa} .

The particular case at hand will now be treated by using Eq. (118). The values of the variables with the "a" subscript are chosen to be consistent with the available data. They are

$$\mu_a = 1.39 \quad (119)$$

$$S_{Ra} = .107 \quad (120)$$

$$1/K_0 = 0 \quad (121)$$

$$X_{0s_0} = 0 \quad (122)$$

$$X_{0\lambda_0} = 0 \quad (123)$$

$$\bar{Y}_{c0_0} = 0 \quad (124)$$

It is desired to find μ for the values of the variables given as

$$1/K = .2 \quad (125)$$

$$X_{0s} = .06 \quad (126)$$

$$X_{0\lambda} = .15 \quad (127)$$

$$\bar{Y}_{c0} = 0 \quad (128)$$

Note that \bar{Y}_{c0} is equal to \bar{Y}_{c0_0} , which causes the last term in Eq. (118) to vanish. The values of μ_0 and S_{R_0} were found from Figure 2, at the intersection of the appropriate divergence boundary and a plot of μ versus S_R calculated for the advancing blade tip Mach number of 0.85. This particular relationship will be defined later in Eq. (141). In the present case, Eq. (141) provides a relationship between μ and S_R which is written as the following equation.

$$S_R = .01855(1 + \mu)^2 \quad (129)$$

The values of the derivatives in Eq. (118) are found from Figures 2 and 6 by dividing an increment in μ by an increment in the variable. For example,

$$\frac{\partial \mu}{\partial (\frac{1}{K})} \cong \frac{\Delta \mu}{\Delta (\frac{1}{K})} \quad (130)$$

where the increments $\Delta \mu$ and $\Delta (1/K)$ are taken while all other variables are held constant. The values of the derivatives needed are

$$\frac{\partial \mu}{\partial S_R} \cong \frac{.08}{.025} = 3.2 \quad (131)$$

$$\frac{\partial \mu}{\partial (\frac{1}{K})} \cong \frac{-.18}{.20} = -.90 \quad (132)$$

$$\frac{\partial \mu}{\partial (x_{08})} \cong \frac{.08}{.06} = 1.33 \quad (133)$$

$$\frac{\partial \mu}{\partial (x_{0a})} \cong \frac{.02}{.25} = .08 \quad (134)$$

When the values given by Eq. (119) through (128) and by Eq. (131) and (134) are used in Eq. (118), the following equation is obtained:

$$\mu \cong 1.30 + 3.2(S_n - .107) = .98 + 3.2S_n \quad (135)$$

When Eq. (135) is used in Eq. (129) the final values of μ and S_n are found. These values are

$$\mu \cong 1.30 \quad (136)$$

$$S_n \cong .10 \quad (137)$$

The effects of pitch-flap coupling are reflected in Figure 20 for the re-treating blade. The combined effects of pitch-flap coupling and structural root cutout on the static torsional stability boundary were found by using Figures 6 and 14 with a method analogous to that demonstrated by Eq. (117) through (137).

The effects of a.t center of gravity on the articulated blade are shown in Figure 21 for an advance ratio of 0.60. The rotor was assumed to be in a lightly loaded condition, as mentioned earlier under the Discussion of Purposes and Methods. A specific static stability boundary was calculated with the simple energy analysis; the same values of tip loss and structural root cutout as those for the extended Normal Mode Transient Analysis calculations were used. This is the boundary that appears on Figure 21. Almost the same boundary is obtained from Figure 2 by defining the stiffness coefficient S_n in terms of the blade length from structural cutout to the outermost aerodynamically effective radius. When the strictly uniform blade without tip loss or structural and aerodynamic root cutout is considered, the static divergence analysis predicts a critical center-of-gravity offset of 7% chord. This offset is measured aft of the 25% chord, where the advancing blade center of pressure and elastic axis are located. The boundary shown on Figure 21 appears at a center-of-gravity offset of 10.3% chord. Thus a reasonably conservative result for critical center-of-gravity location can be obtained by ignoring tip loss and the normal amount of structural cutout.

The information on Figures 22 and 23 is for the nonarticulated rotor. It can be seen that the torsional stress response is very similar to that for the articulated blade. The absence of the blade hinges does, of course, cause the blade bending stresses to be somewhat higher. It should be remembered that this particular result is for a uniform blade and that design refinements can alter the stress distribution. The stress results presented here are intended only to show that a practical operating limit is being approached. The static torsional stability boundaries are virtually identical for articulated and nonarticulated blades at $\mu = .6$, as shown by Figure 13.

Figure 24 shows the results of the gyro feedback calculations. It can be seen that a fairly large increase in blade torsion response occurs because of the gyro action with the particular control gyro parameters chosen.

DISCUSSIONS OF TORSIONAL DIVERGENCE RESULTS

SIGNIFICANCE OF TORSIONAL DIVERGENCE DESIGN PARAMETERS

The scope of this study included independent variations in all of the important parameters affecting the torsional divergence calculations for helicopter blades. The various charts included in this volume show the relative significance of the various design parameters as well as quantitative data. The practical significance of changes in some of these parameters will, however, be clarified by additional discussion.

The basic relationship for the torsional divergence boundaries is between the familiar advance ratio μ and the nondimensional stiffness coefficient S_R , which is basically a ratio of elastic and aerodynamic torsional stiffness effects. It should be noted that the rotational tip speed is used in the formation of these parameters. Thus, an increase in S_R can signify a larger torsional elastic stiffness or a decrease in the quantity in the denominator in Eq. (108). This may occur for a given blade because of operation with lower air density or rotational speeds. As would obviously be expected, increasing the value of S_R raises the critical advance ratio in all cases. An increase in S_R resulting from a decrease in rotational speed does, however, result in a drop in critical aircraft forward speed for retreating blade divergence. Therefore, the typical appearance of the divergence boundaries of a representative blade on a tip speed versus forward speed plane is of important practical interest. Examples of this relationship are shown in Figures 25 through 28. These charts were prepared from Figures 2, 3, and 4, with S_R assumed to be 0.040 when tip speed is 660 ft/sec. This is a uniform blade comparable to the CH-3C blade when operating under normal conditions with a lift-curve slope of 2π .

The effect of changing the parameter $S_R(R\Omega)^2 = 2GJ_0 / \rho a_0 c_0^2 R^2$ is shown on Figure 25. Note that this parameter includes blade torsional stiffness, chord, radius, air density, and lift-curve slope. The boundaries shown on the chart for various values of this parameter include that for the representative blade and those for $2/3$ and $3/2$ of that value. Note also that any number of these boundaries may be plotted from a single S_R versus μ plot. Thus, this choice of parameters greatly condensed the number of charts necessary to evaluate the effects of any appreciable variations in $2GJ_0 / \rho a_0 c_0^2 R^2$.

The effect of blade chordwise center-of-gravity position is shown by the various corresponding boundaries in Figure 26. The aft center-of-gravity positions give rise to advancing blade boundary segments, which appear as lines nearly parallel to the constant advancing tip Mach number line. The effect of changes in blade lift-curve slope due to Mach number is not included on this chart, since only approximate quantitative information is desired. If the correction for Mach number is desired, the actual lift-curve slope for a given Mach number at the 75% radius can be used in the definition of S_R . The Mach number is generally low on the retreating blade, so the lift curve slope on the corresponding segment of the boundary will not be appreciably affected by compressibility effects.

The most inboard nondimensional radius for which significant aerodynamic blade torques are produced is called the aerodynamic root cutout, X_{0A} . This parameter has a significant effect on retreating blade torsional divergence, since the inboard blade sections are subjected to the highest velocity reversed flow. It can be seen from Figures 2, 3, and 4 that the beneficial effect of root cutout is more pronounced with the larger values of $1/K$, as would also be expected, since a smaller control stiffness causes greater blade deflections, particularly close to the root. For the representative blades, Figure 27 shows the effects of changing root cutout on the flight condition boundaries.

The control stiffness ratio, $K = K_r L_b / J_0 G$, can be also defined as blade deflection divided by the control system deflection when the blade and control system are subjected to a torsional couple at the tip. It will be noted that this parameter is treated in inverse form on the charts to permit plotting very large values of K . The value $K = 1,000$ is large enough so that only infinitely small effects on torsional divergence due to root flexibility occur. For the representative blades, Figure 28 shows the effects of changing control stiffness ratio.

It will be noted from Figures 25 through 28 that the practical variations considered for root cutout, center-of-gravity position, and control stiffness ratio generally have only moderate effects on the flight condition boundaries for the retreating blade. The aft center-of-gravity positions do, of course, make an advancing blade torsional divergence possible at much lower speeds.

The ratio of blade chord to rotor radius C_0/R , has a negligible effect on the two-degree-of-freedom torsional divergence analysis for variations of C_0/R between 0.04 and 0.06.

The independent effect of linear taper in chord is shown in Figure 5. It should be remembered that these variations were made with blade chord at the 75% radius remaining constant, and with the torsional stiffness coefficient defined using that chord. All other blade properties were the same as for the corresponding uniform blade. It is interesting to note that with the above definition of S_R , the addition of chord taper causes a moderate reduction in retreating blade divergence advance ratio. However, if S_R is defined further inboard, the boundaries could practically coincide or even be reversed in their relative positions. The practical conclusion for this type of taper is better suggested by Figure 5, with a moderate reduction in divergence speed because of larger inboard chord in the region of higher reversed velocity.

The structural cutout, or torsionally rigid inboard section has the straightforward effect shown in Figure 6.

The independent effect of tapered torsional stiffness on retreating blade divergence is shown in Figure 7. It can be seen that the nondimensional boundary is virtually unaffected, provided the torsional stiffness coefficient S_R is defined using blade stiffness at the 75% radius station. This result arises because smaller stiffness outboard of the 75% radius counteracts the benefit of increased stiffness inboard.

The independent effects of nonuniform inertia, which enter into the torsional divergence static stability calculations because of variations in the assumed torsional mode shape, are shown in Figure 8 and 9. Figure 8 was prepared for two values of aerodynamic cutout by assuming an inboard section with negligible torsional inertia. It can be seen that this variation has only a small effect. As would be expected, the generally smaller deflections inboard for the mode shape of the blade with inertial cutout cause a higher critical advance ratio to be predicted.

The effect of a linear variation in inertia is shown in Figure 9. This figure was prepared by assuming torsional inertia at the 75% radius equal to that of the uniform blade. It can be seen that the generally larger inboard deflections for the mode shape of the blade with inertial taper cause a small decrease in predicted divergence advance ratio.

Spanwise variations in center-of-gravity location, with the location at the 75% radius remaining constant at the 10% chord forward position, were considered. Inboard cutouts of center-of-gravity offset up to the 45% radius and linear tapers with the ratio of root offset to tip offset as high as three produced virtually no effect on the retreating blade cases considered.

The effect on advancing blade divergence of a lift-curve slope distribution due to the familiar Glauert Mach number correction is shown in Figure 10. Note that the torsional stiffness coefficient is defined by using the local lift-curve slope at the 75% radius. The value $S_c = .0286$ refers to a blade similar to a conventional blade with twice the torsional stiffness operating under normal conditions. It can be seen that with torsional stiffness coefficient defined in the manner described earlier, very little effect due to Mach number lift-curve slope variation can be noted on the nondimensional charts. Even less effect is noted on the retreating blade, shown in Figure 11, as would be expected. Even though the radial variation in Mach number effects has little effect on the nondimensional charts, it should be remembered that an effect will be felt on the actual flight condition boundary, since a larger average lift-curve slope is reflected in a smaller stiffness coefficient.

The effect of bending mode shape for a nonarticulated blade, as compared with the rigid flapping mode used for the articulated blade, is shown in Figure 12 and 13. It should be noted that the uniform blade natural bending mode shape and natural frequency to rotational speed ratio depend only on the parameter $El_r/m\Omega^2 R^4$, so that a definite mode shape and frequency ratio is defined by the product of S_n , the ratio of bending to torsion stiffness El_r/GJ_0 , and a parameter $\rho a_0 c_0^2/m$. The effect of articulation was determined for two values of El_r/GJ_0 with the standard value of $\rho a_0 c_0^2/m$. The same variations in critical advance ratio would occur for a change in the product of these two parameters $El_r \rho a_0 c_0^2/GJ_0 m$ by the same factors. The value El_r/GJ_0 of 0.598 is similar to conventional practice, while $\rho a_0 c_0^2/m$ is also appropriate to a lift-curve slope of 2π and standard sea level conditions. It is readily apparent that the values considered produce very little effect on torsional divergence for the retreating blade and a moderate effect for the advancing blade. The changes in the relative positions of the various boundaries are

probably caused by interacting favorable effects of bending stiffness and unfavorable effects of the various bending mode shapes.

The pronounced lowering of retreating blade torsional divergence advance ratio predicted by the simple energy method for pitch-flap coupling is shown in Figure 14. It should be noted that the studies with the extended Normal Mode Transient Analysis show this predicted effect to be very conservative. The effects of pitch-flap coupling for the initially unloaded rotor can be seen by comparing Figures 17 and 20. The peak-to-peak torsional stress is actually reduced by pitch-flap coupling for a given advance ratio while the peak-to-peak flatwise stress increases. However, the practical retreating blade advance ratio stress boundary is very little affected by the addition of $\delta_3 = 45^\circ$, according to these Normal Mode Transient Analysis results.

The provision of the control gyro configuration used in this study was found to increase blade torsional response, and, therefore, to lower slightly the permissible advance ratio for a given stress by a decrement of approximately .10. This is shown in Figures 22 and 24. It should be remembered that the effect of the gyro can be changed by altering the various parameters and that no general implications can be drawn without further analyses.

It has been demonstrated, as discussed earlier in this section, that the most significant improvements in torsional divergence speed may be brought about by changing the quantities involved in the torsional stiffness coefficient S_n . Thus, an increase in the quantity $GJ_0/\rho a_0 c_0^2 R$, which can be brought about by an increase in blade torsional stiffness or a decrease in chord, rotor radius, lift-curve slope, or air density, will raise the speed. On the other hand, decreasing rotor rotational speed will lower the aircraft divergence speed for retreating blade divergence, but will increase it for advancing blade divergence. If the blade has an excessively large aft chordwise center-of-gravity position, very large improvements in torsional divergence speed are possible by returning to the normal balanced blade configuration. Significant improvements may also be realized by providing stiff inboard blade sections, as illustrated by Figure 6. This should not be undone by decreasing the stiffness of outboard blade sections. In Figure 7, it can be seen that the divergence boundaries for a tapered blade and a uniform blade are almost identical. The beneficial high inboard stiffness indicated by Figure 6 must be derived from an inboard stiffness that is higher in an absolute sense rather than higher relative to the tip. It should be remembered that Figure 7 was prepared with the same stiffness at the 75% radius for tapered and untapered blades, with all other parameters, including chord, remaining unchanged. Other parameters investigated were found to have moderate independent effects, but it can be expected that significant improvements will be achieved through the combined favorable effects of changes in a number of them. The significance of the various parameters investigated has been discussed above, with respect to the torsional divergence calculated results. The practical significance of the torsional divergence concept itself should be reviewed, as it applies to a helicopter rotor blade. The most superficial inspection of the Normal Mode Transient Analysis results, such as Figures 15 and 16, shows that the calculated stability

boundary for torsional divergence corresponds generally to the onset of torsional oscillations of comparatively high frequency. Thus, the basic equations of static torsional divergence, which neglect all inertial effects, cannot be viewed as a mathematical model of a physical phenomenon in the usual sense. The torsional divergence calculated results should rather be viewed as a so-called "rule of thumb". The virtue of these results lies in the relatively simple manner in which they can be obtained and the fact that the results do indeed correspond with those of a much more elaborate method. The practical boundary for retreating blades, as limited by peak-to-peak torsional stress, is accurately predicted for all parameter variations considered with the Normal Mode Transient Analysis, except for the effect of pitch-flap coupling. The aft center-of-gravity advancing blade stress "boundary" is not as well defined, probably because of complicated compressibility effects. The torsional static stability boundary provides a conservative estimate of the rather gentle onset of high torsional stresses for the unloaded blade.

Therefore, in view of the above, the inclusion of a large number of elaborate features in a torsional divergence calculation is apparently not warranted. It should also be pointed out that predicted trends for parameters not investigated previously may not necessarily be accurate or correct. Torsional divergence results for parameter variations not yet considered and for radically different designs should therefore be checked with more elaborate methods, as was done under this contract for some parameters. The effect of inertia distributions on torsional divergence should be checked with particular thoroughness.

The ultimate objective of torsional divergence calculations should always be a guide for more elaborate methods. When a relatively large number of torsional divergence calculations have defined flight conditions and configurations critical for blade torsional stiffness, a much smaller number of dynamic solutions can be used to check these critical regions.

PERMISSIBLE ANALYTICAL ASSUMPTIONS

In the following, the torsional divergence calculations and results will be reviewed with the objective of outlining useful analytical assumptions for such calculations.

The results shown in Figures 2 through 4 establish that the basic advance ratio versus torsional stiffness coefficient relationship is affected by practical variations in the aerodynamic root cutout, control stiffness ratio, and blade chordwise center-of-gravity position. The effects of these parameters are interrelated in such a way that no generally useful statement concerning negligible values, which will be suitable for all cases can be given. The effect of root cutout, for example, is more pronounced when the control stiffness ratio is low.

Figures 5 and 6 show that spanwise variations in chord and structural cutout have moderately important effects.

Figure 7, on the other hand, shows that linear variations in torsional stiffness may be neglected in the simple torsional divergence calculation, if the value of stiffness at the 75% radius is used to represent an equivalent blade with uniform stiffness.

Figures 8 and 9 reflect variations in torsional mode shape consistent with quite extensive variations in blade mass distributions. These can be seen to produce rather small changes in calculated torsional divergence results, and the use of a uniform blade torsional mode shape will be adequate for most cases. This would not necessarily be true for even more extensive variations in modal properties, such as those appropriate to a weightless blade with tip mass. It should be pointed out again that the effect of mass on torsional divergence is not logically consistent with the basic assumption of no inertial effects. Earlier work, however, has indicated that the correct trends appear to be produced by using the natural mode shape corresponding to the mass distribution in the static torsional divergence calculations. While a basic inconsistency is present from a strictly logical point of view, the use of torsional divergence calculations for rule-of-thumb purposes makes this practice reasonable, since the effect of mass distribution on torsional stress appears to be predicted with the desired accuracy. This characteristics of the torsional divergence calculations should be checked with more elaborate analyses, as mentioned previously.

Figures 10 and 11 show that lift-curve slope corrections may be confined to the lift-curve slope at the 75% radius in the definition of torsional stiffness coefficient S_n . This will be true if the spanwise variation is no more severe than that due to the Prandtl-Glauert correction for an advancing blade 75% radius Mach number of approximately 0.70.

Figures 12 and 13 show that nonarticulated blades of conventional design will have calculated torsional divergence speeds close to those for articulated blades. This is confirmed by the Normal Mode Transient Analysis results shown in Figures 17, 21, 22, and 23.

Figure 14 shows a large drop in torsional divergence advance ratio due to pitch-flap coupling, which was not reflected in the results of the Normal Mode Transient Analysis shown in Figures 17 and 20. The effects of δ_3 should therefore be investigated with a more rigorous analysis.

In addition to the above considerations, the independent effects of variations in mass ratio M_r were found to be negligible. The effects of linear spanwise variation in chordwise center-of-gravity position were also small, if the position at the 75% radius was used to compare with the uniform blade results.

TORSIONAL DIVERGENCE PRELIMINARY DESIGN PROCEDURES

The following paragraphs include recommendations as to the use of the torsional divergence charts in the preliminary design stages of new rotor systems.

It should be recognized that a complete outline of preliminary design procedure is beyond the scope of this study. Examples of how information useful in preliminary design may be obtained from the charts are given. The designer should determine the specific studies to be made. These studies must determine advantageous combinations including not only required stiffness but also items such as weight, cost, and aerodynamic performance.

The torsional divergence charts can be used to define allowable relationships between torsional stiffness, blade geometry and operating conditions. It can be expected that large torsional stresses will arise if these relationships are exceeded significantly.

It should be remembered that high torsional stresses may arise for other reasons, even though the blade is satisfactory from the standpoint of torsional divergence. The presence of classical or stall flutter, which may occur well below the torsional divergence boundary, will also result in high torsional stresses. Excessive flapping motion may also result in large torsional stresses, depending on the modal coupling present. Torsional resonance with rotor orders must also be avoided.

It must be assumed that certain parameters have been defined at the start of a preliminary design effort by the basic mission requirements and the resulting aerodynamic preliminary rotor design. In particular, it is assumed that rotor diameter, blade chord, aircraft forward velocity, rotor rotational speed, and air density are known or chosen. In preliminary design, it is recommended that Figures 2 through 4 be used. If the normal amounts of tip loss and structural root cutout are neglected, an appropriate amount of conservatism will be introduced.

With the quantities just mentioned, the advance ratio is calculated, and Figures 2, 3, or 4 entered to find a required S_n for the desired values of aerodynamic root cutout X_{oa} . Then the definition of S_n given in Eq. (108) is used to find the torsional stiffness GJ_0 required. The lift-curve slope a_0 is appropriate for the conditions at the 75% blade radius on the advancing or retreating blade.

The above procedure can be carried out quickly for systematic variations in control stiffness ratio and center-of-gravity location by using the trade-off charts in Figure 3 and 4. The blade weight for each combination of torsional stiffness, control stiffness ratio, and center-of-gravity position can then be determined to find the minimum weight configuration for the given flight condition.

Another possible procedure might begin with blade stiffness, chord, approximate lift-curve slope, and radius defined, so that variations in the quantity $S_n (R \Omega)^2$ are determined by air density and rotational tip speed. Then flight condition boundaries similar to those shown in Figures 25 through 28 can be determined for various values of altitude, root cutout, or control stiffness ratios. This is done by choosing a list of advance ratios, determining the corresponding list of critical S_n values from Figures 2, 3, or 4, and then solving for rotational tip speed ΩR from the value of $S_n (R \Omega)^2$, consistent with the assumed altitude. Note

that the altitude is reflected in the value of air density. The exact Mach number and lift-curve slope will not be known until the boundary is determined if this method is used; therefore, it may be desired to repeat the process with the lift-curve slope appropriate to the approximate Mach number for each of the advance ratio and rotational tip speed solutions.

An alternate procedure to obtain flight condition boundaries, such as those described in the preceding discussions, is based on the assumption of various advancing blade tip Mach numbers. This procedure permits the use of the correct lift-curve slope without need for trial and error, but it is slightly more elaborate. This method is especially useful for the high advance ratio and high Mach number conditions.

The advancing blade tip and 75% radius Mach numbers on the advancing and retreating blades are given respectively by

$$M_{1,90} = \frac{\Omega R(1+\mu)}{A^*} \quad (138)$$

$$M_{.75,90} = \frac{\Omega R(.75+\mu)}{A^*} = M_{1,90} \frac{(.75+\mu)}{(1+\mu)} \quad (139)$$

$$M_{.75,270} = \frac{\Omega R|\mu-.75|}{A^*} = M_{1,90} \frac{|\mu-.75|}{1+\mu} \quad (140)$$

When Eq. (138) is used in the definition of S_R ,

$$S_R = \frac{2GJ_0}{\rho a_0 C_0^2 R^2 (\Omega R)^2} = \frac{2GJ_0(1+\mu)^2}{\rho a_0 C_0^2 R^2 (A^* M_{1,90})^2} \quad (141)$$

When the advancing blade tip Mach number $M_{1,90}$ and the value of advance ratio μ are defined, Eq. (141) can be used to calculate a value of S_R . The lift-curve slope at the 75% radius is used in this calculation. The lift-curve slope is corrected for the Mach number at the 75% radius which is calculated by using Eq. (139) or Eq. (140) for the advancing or retreating blade respectively. Thus, two curves of μ versus S_R are obtained, one for the retreating blade and one for the advancing blade if there is an aft center-of-gravity location. These are plotted on the appropriate chart in Figure 2, and the intersection with the divergence boundaries is noted. The same μ and $M_{1,90}$ intersection is then plotted on a rotational tip speed ΩR versus forward speed (V) chart to give a point on the flight condition boundary. This is repeated for other values of $M_{1,90}$ until a torsional divergence boundary is defined. Other boundaries can be determined as desired by using a new value of the quantity $2GJ_0/\rho C_0^2 R^2$ in Eq. (141). Obviously, changes in this group of parameters can come about because of variations in torsional stiffness, air density, and blade area. The effects of aerodynamic root cutout, control stiffness ratio, and center of gravity are considered by using the proper curves in Figure 2.

Approximate corrections for chord taper, structural cutout, inertia variations and nonarticulation may be made if desired. This can be done by adding the appropriate increment to S_n , as indicated at each value of μ in Figures 5 through 10 and 12 and 13.

A few procedures have been outlined above for the rapid definition of satisfactory relationships between blade torsional stiffness and rotor performance objectives using the design charts presented. These should not be considered as restrictions, however, since other procedures will probably occur to various users. Detailed explanations of how the charts were obtained have been given to allow individual users to develop their own procedures. The major restriction on the development of other procedures is that they be simple, rapid, and consistent with the approximate nature of the torsional divergence concept for helicopter blades. In the later stages of design work, the more critical flight conditions must be reevaluated with more elaborate methods, including those for the prediction of forced blade motions and stresses, classical flutter, and stall flutter.

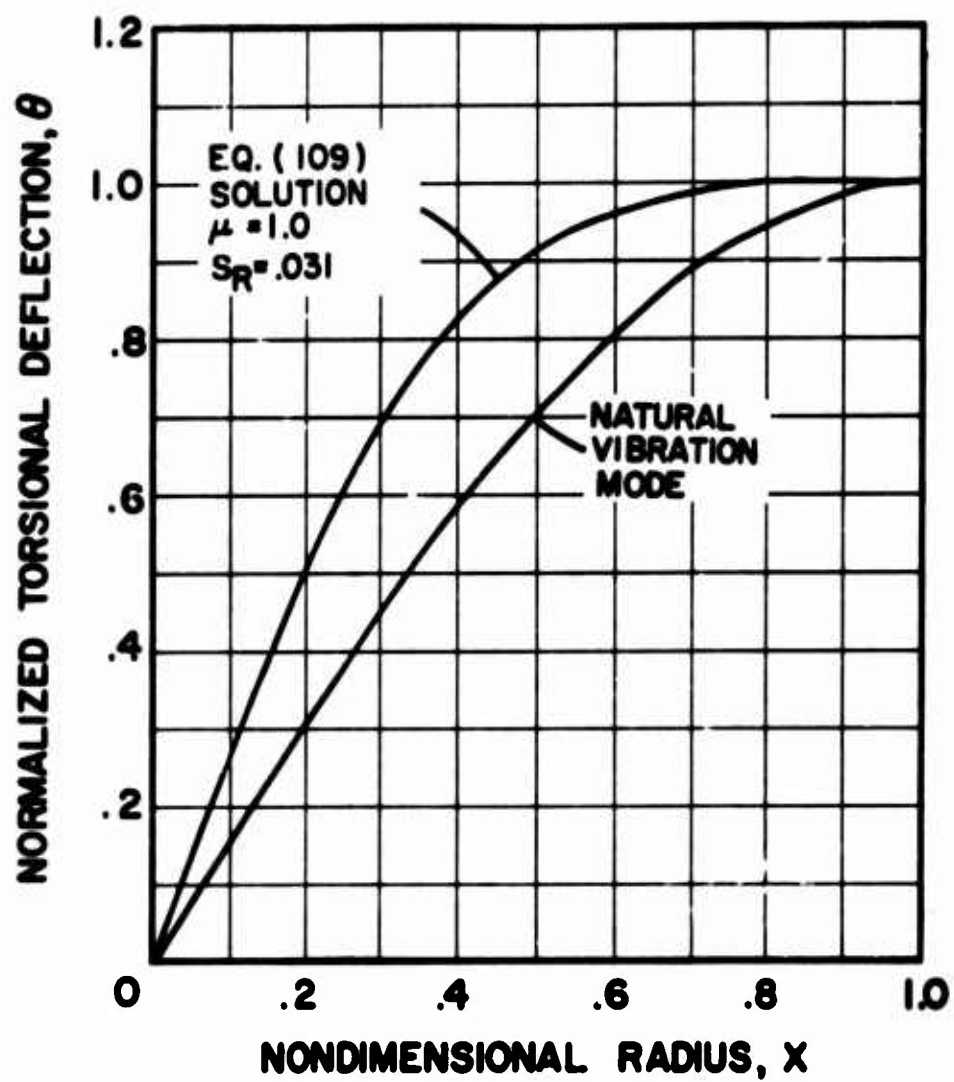


Figure 1. Comparison of Differential Equation Solution and Assumed Divergence Mode .

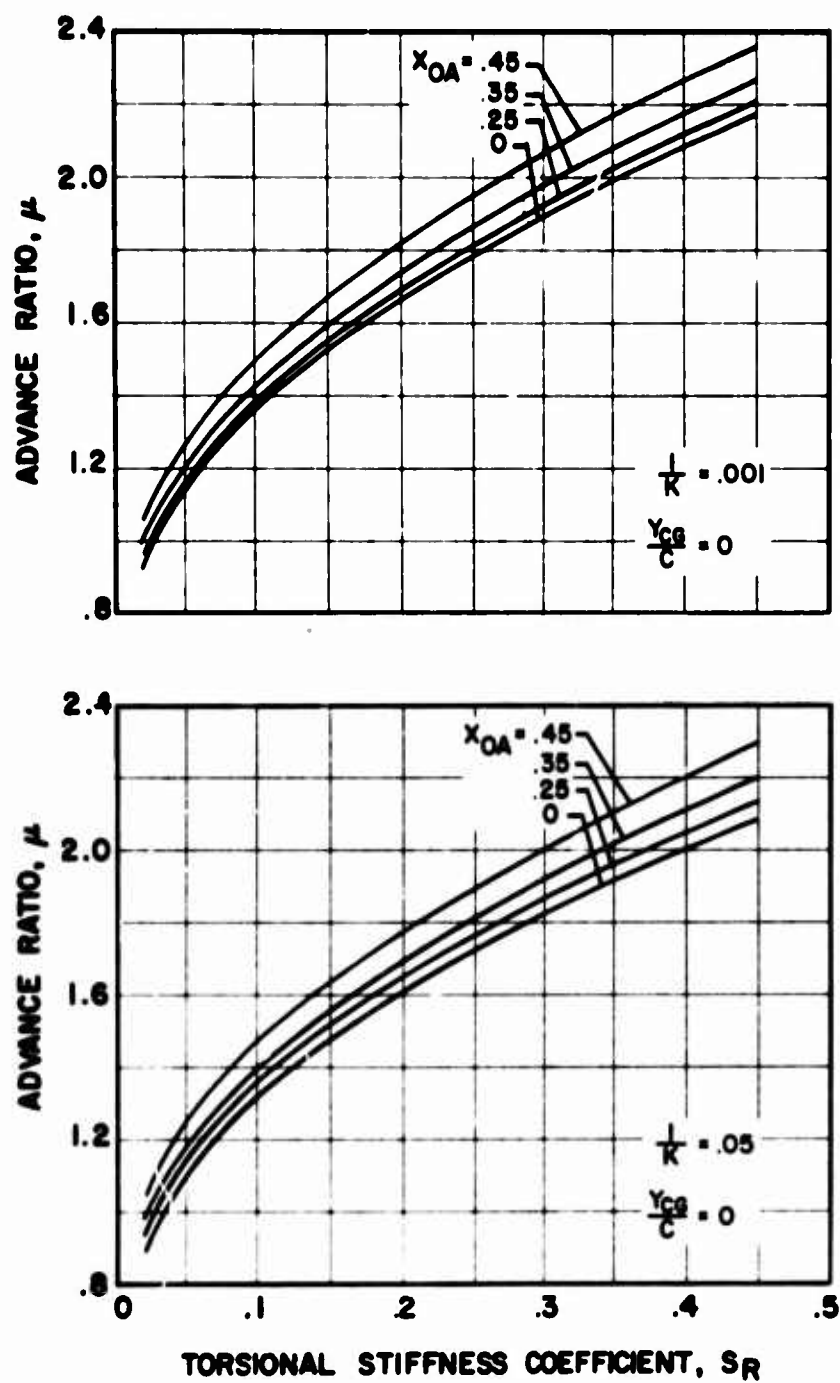


Figure 2. Advance Ratio Versus Torsional Stiffness Coefficient for Various Control Stiffness Ratios and Center-of-Gravity Positions; $x_{CG} = 0$, $\alpha_0 = 2\pi$.

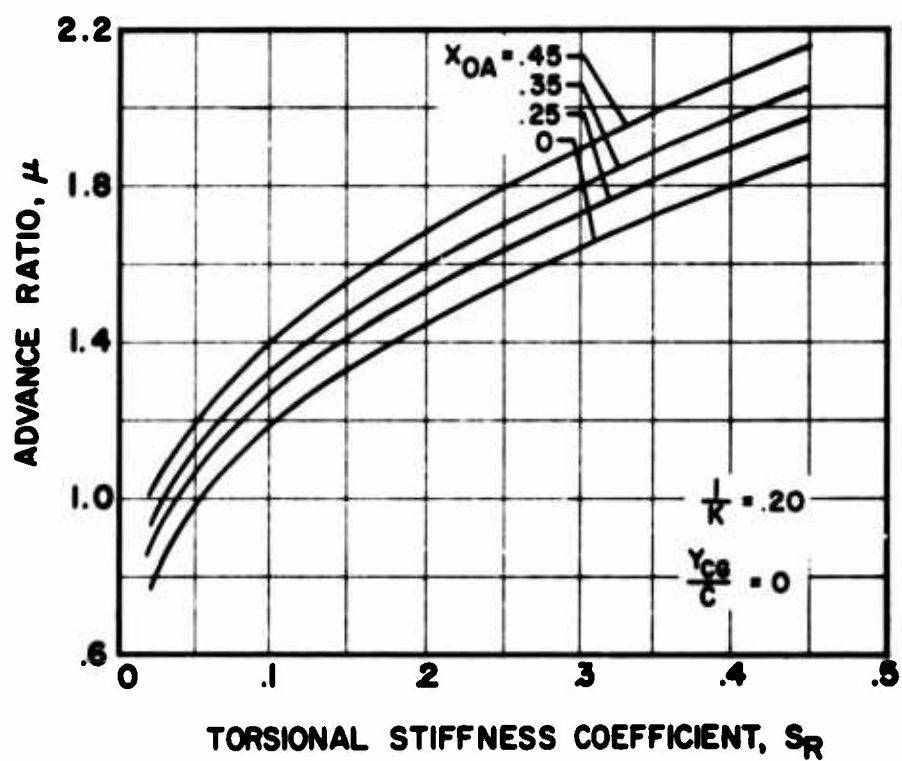
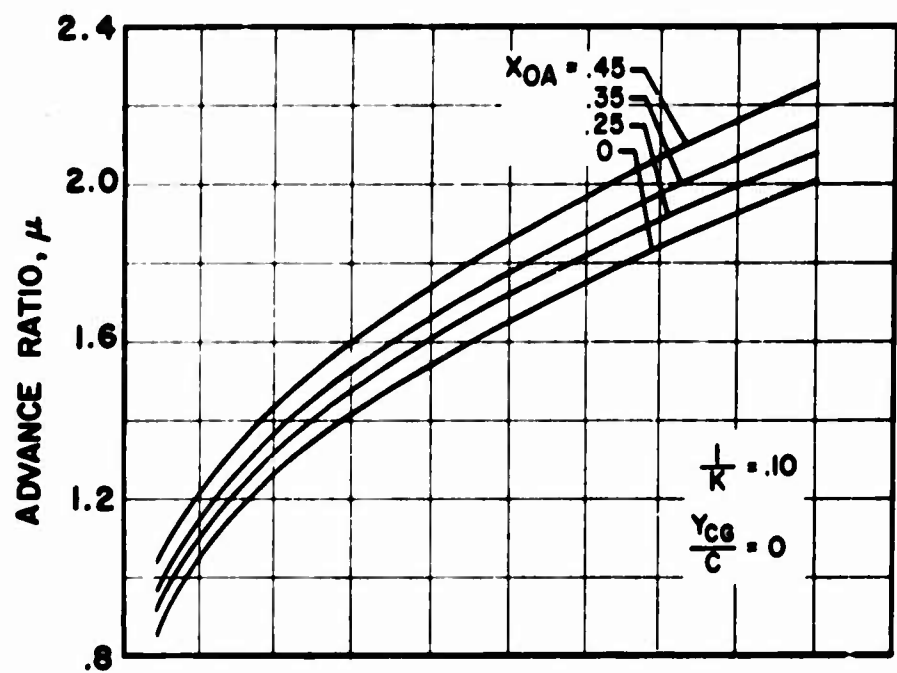


FIGURE 2. CONTINUED.

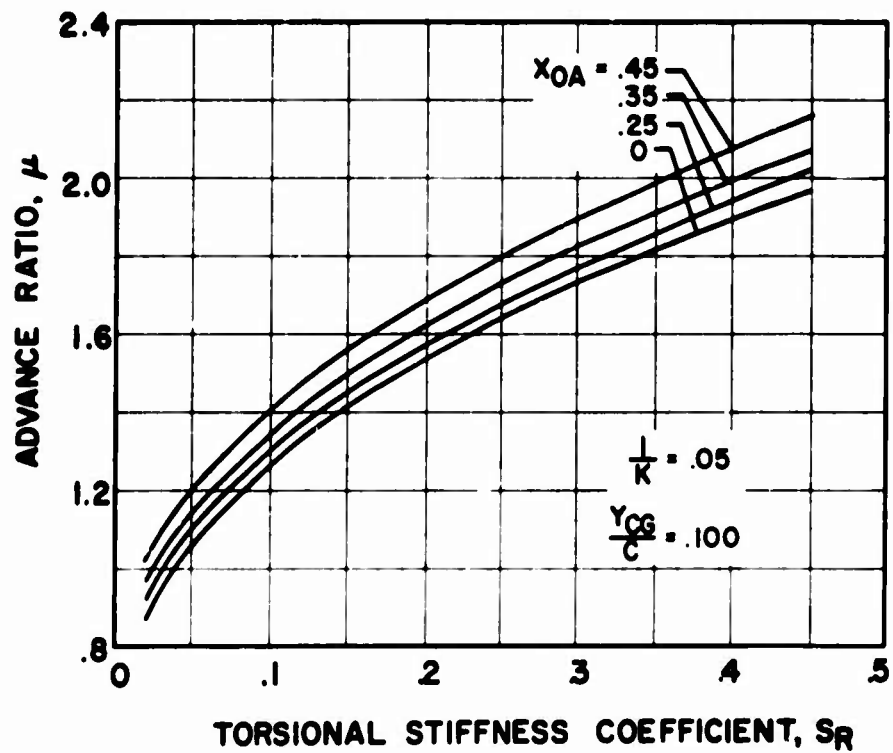
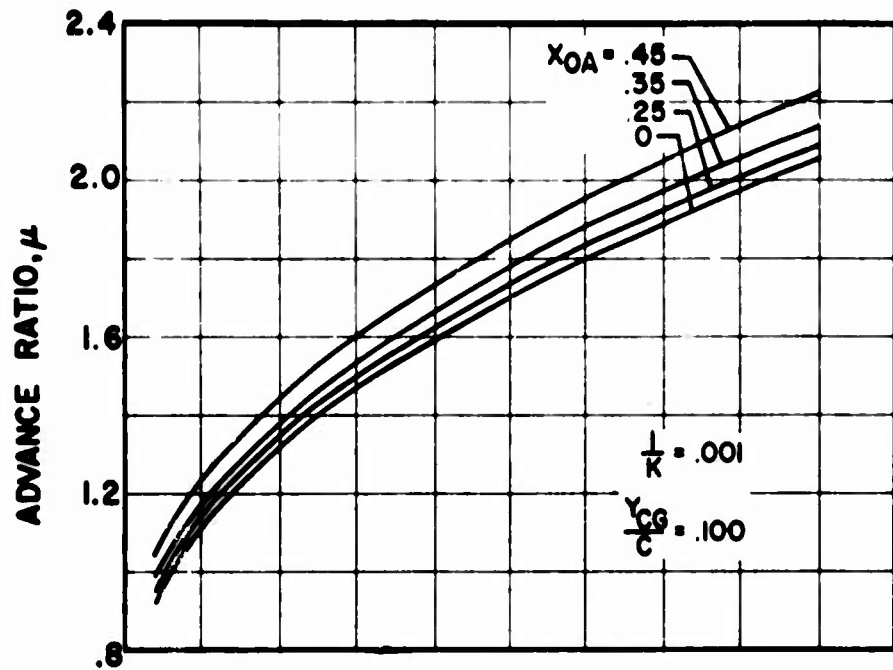


FIGURE 2. CONTINUED.

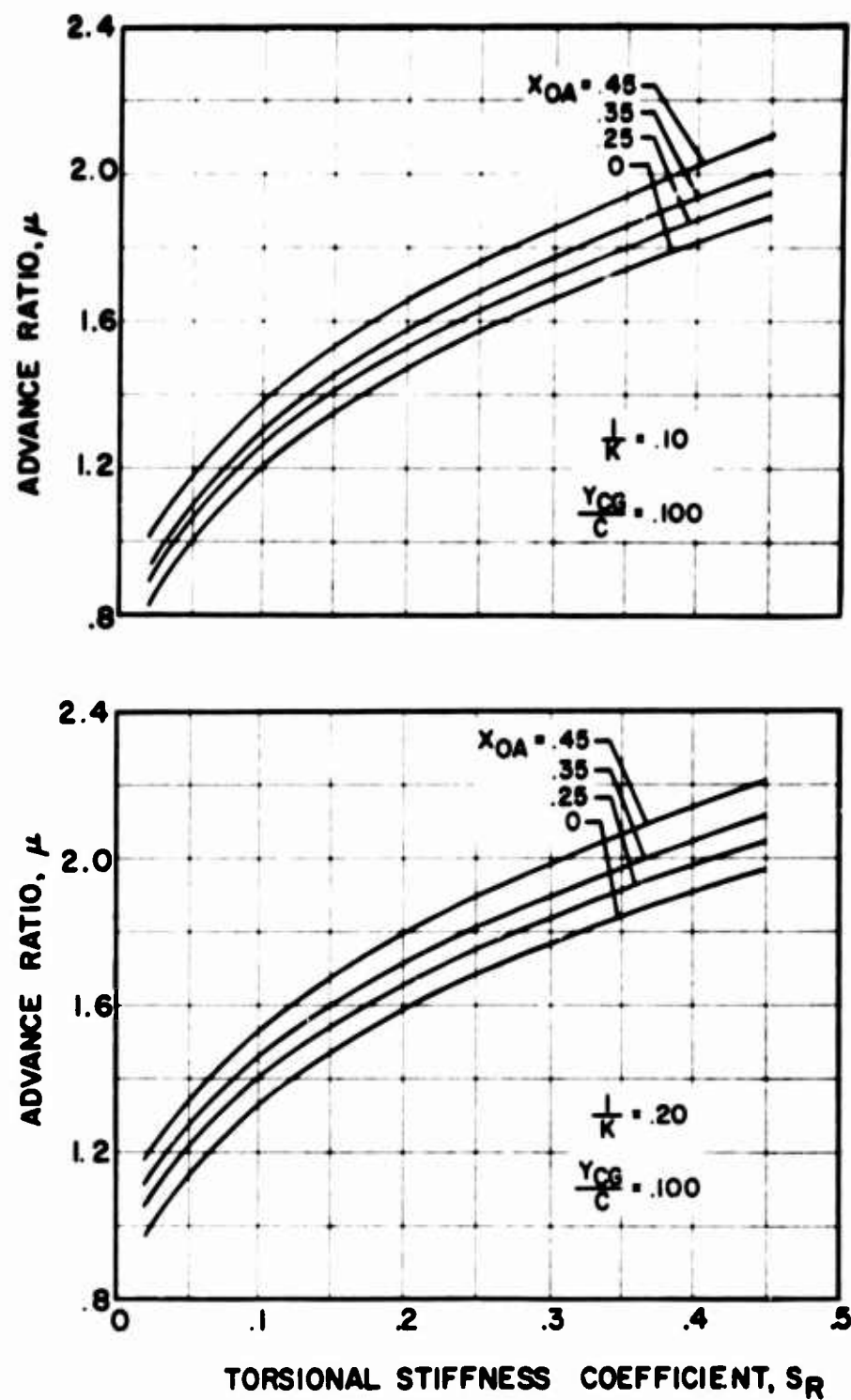


FIGURE 2. CONTINUED.

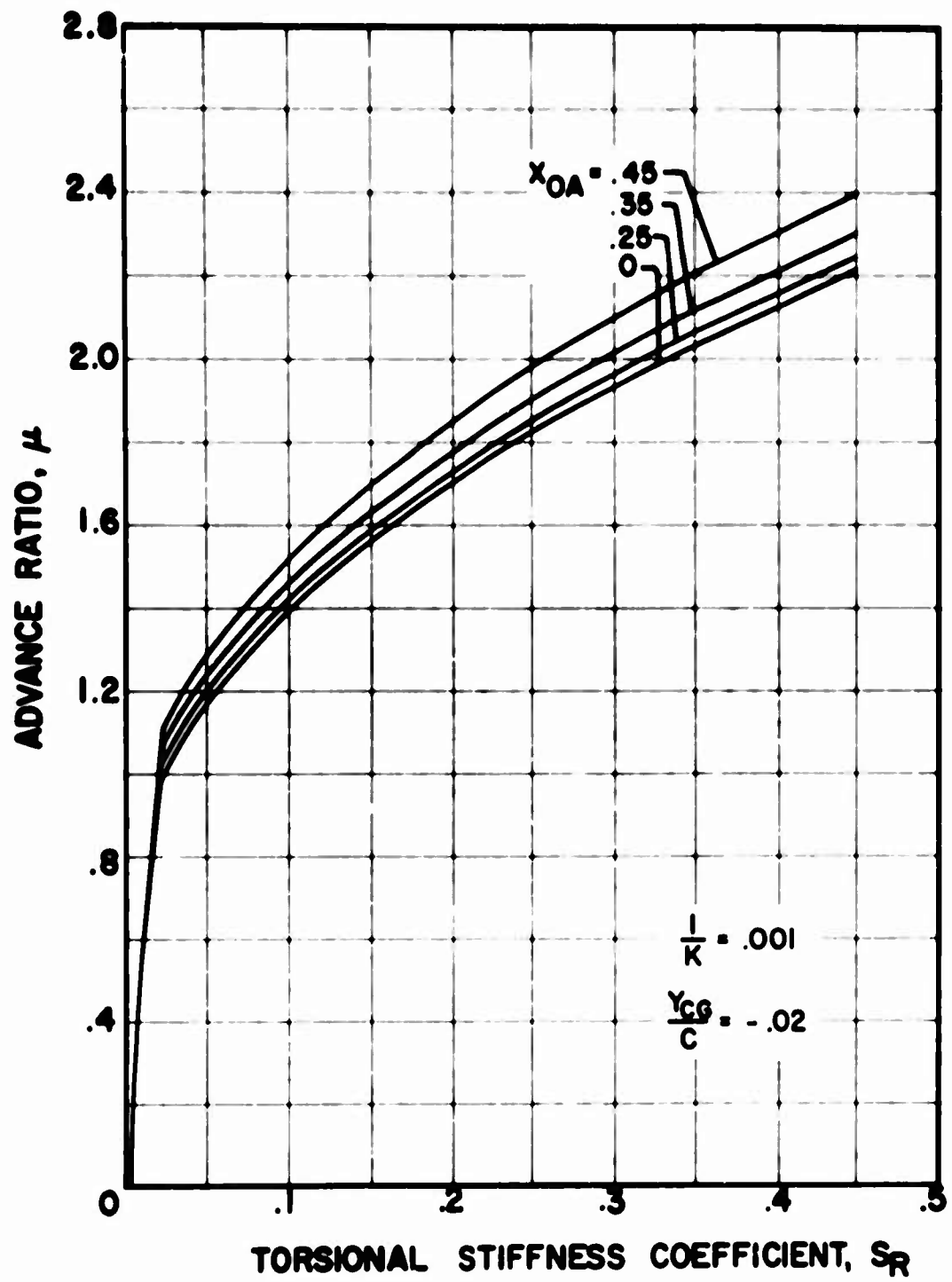


FIGURE 2. CONTINUED.

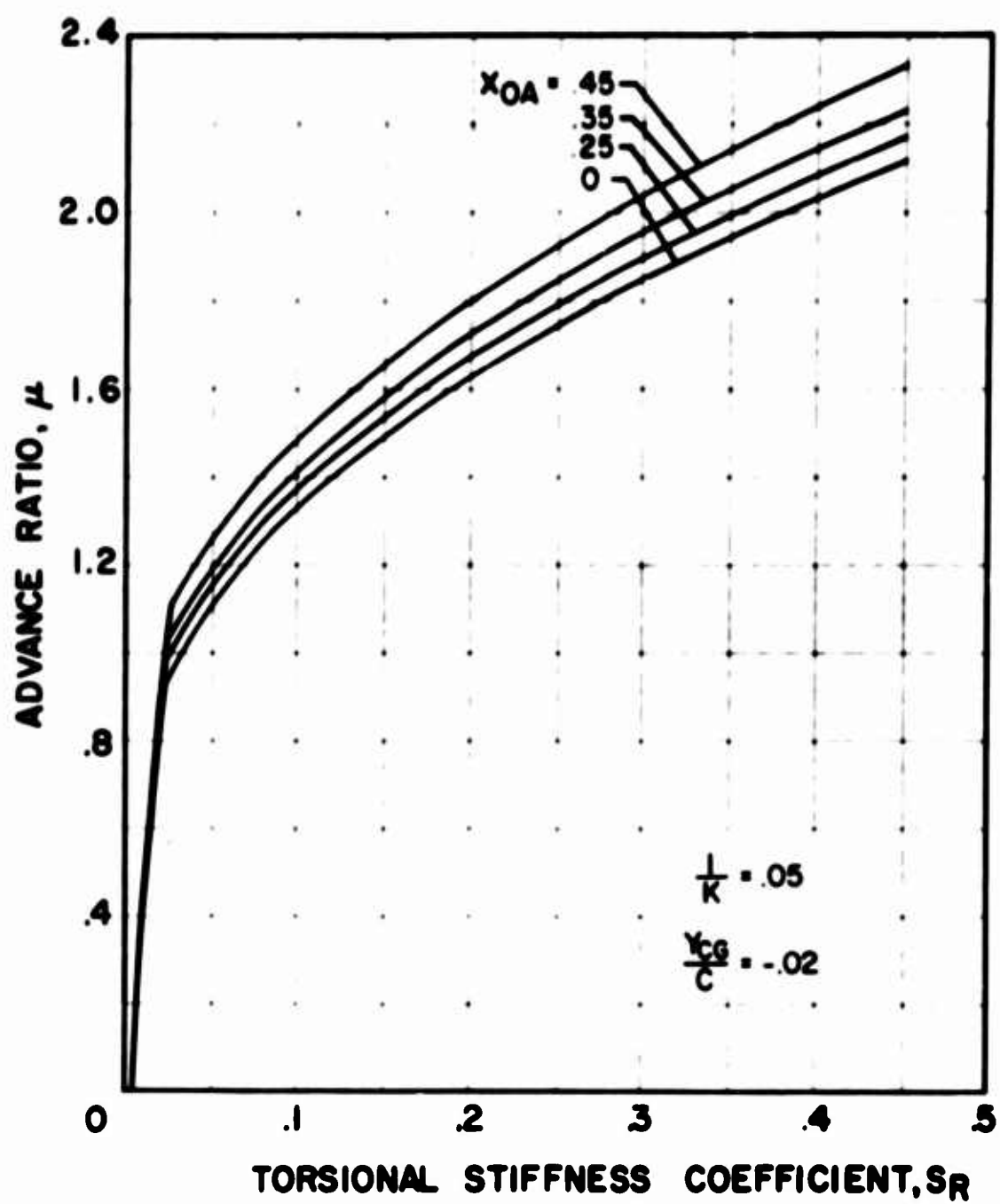


FIGURE 2. CONTINUED.

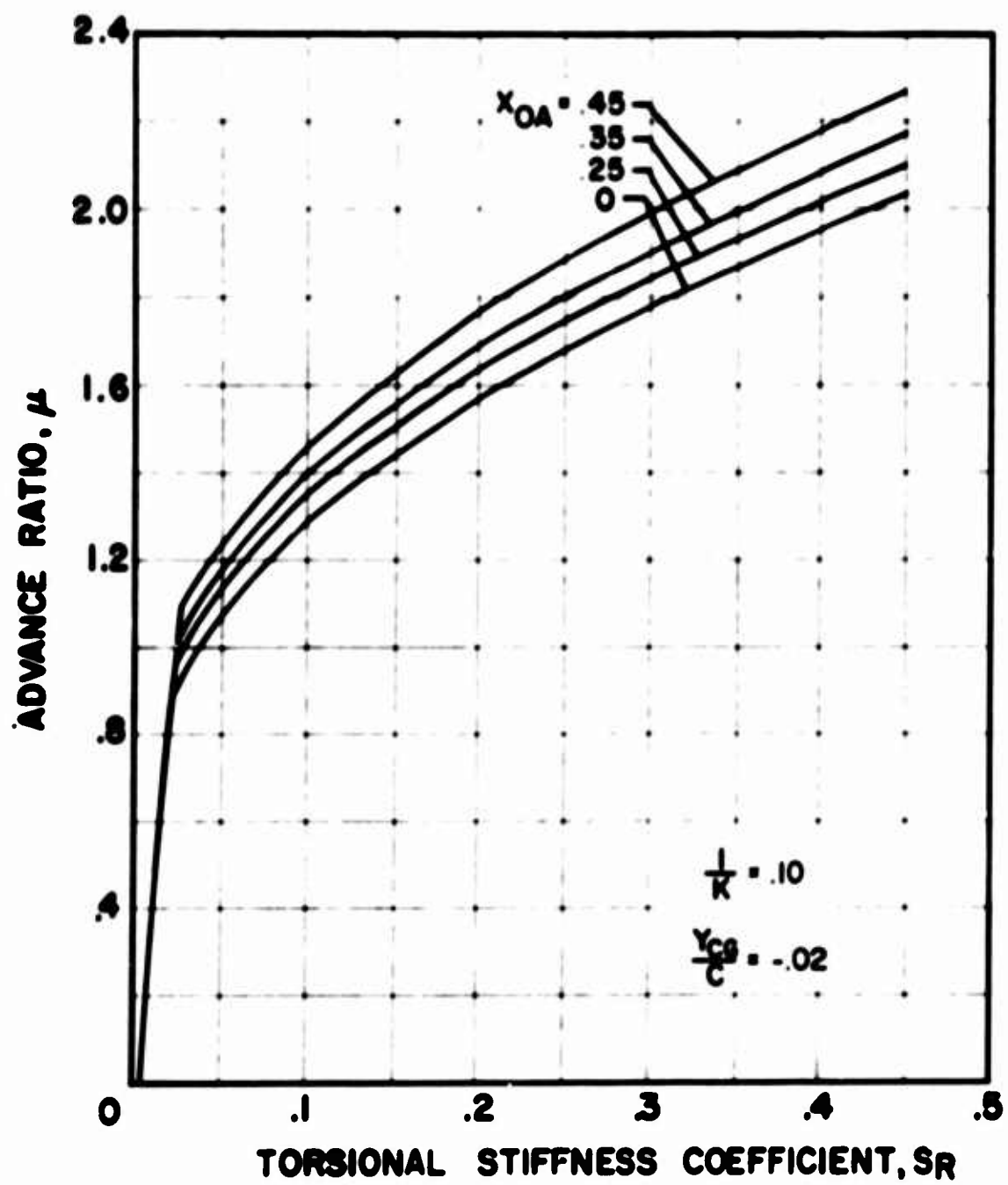


FIGURE 2. CONTINUED.

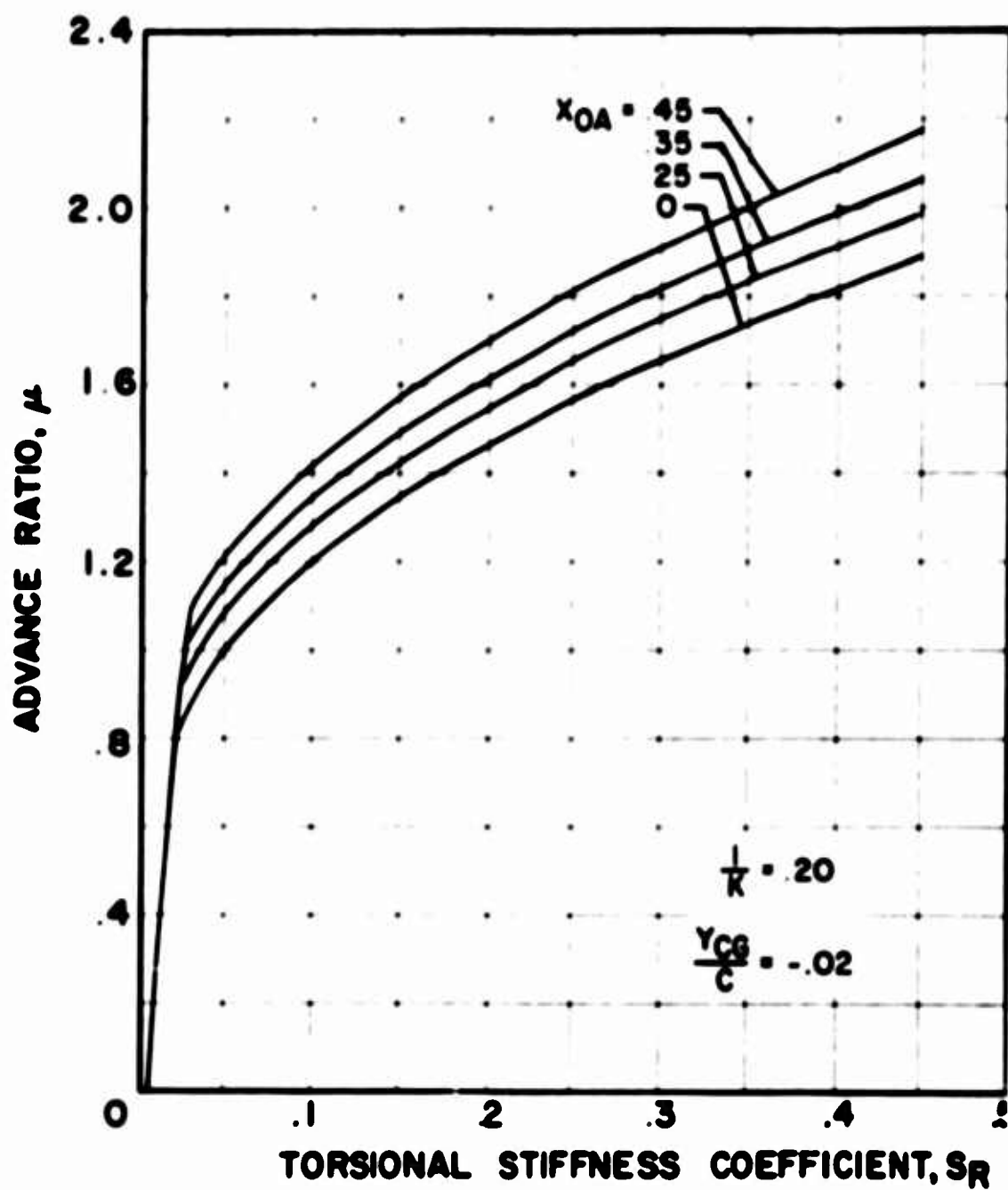


FIGURE 2. CONTINUED.

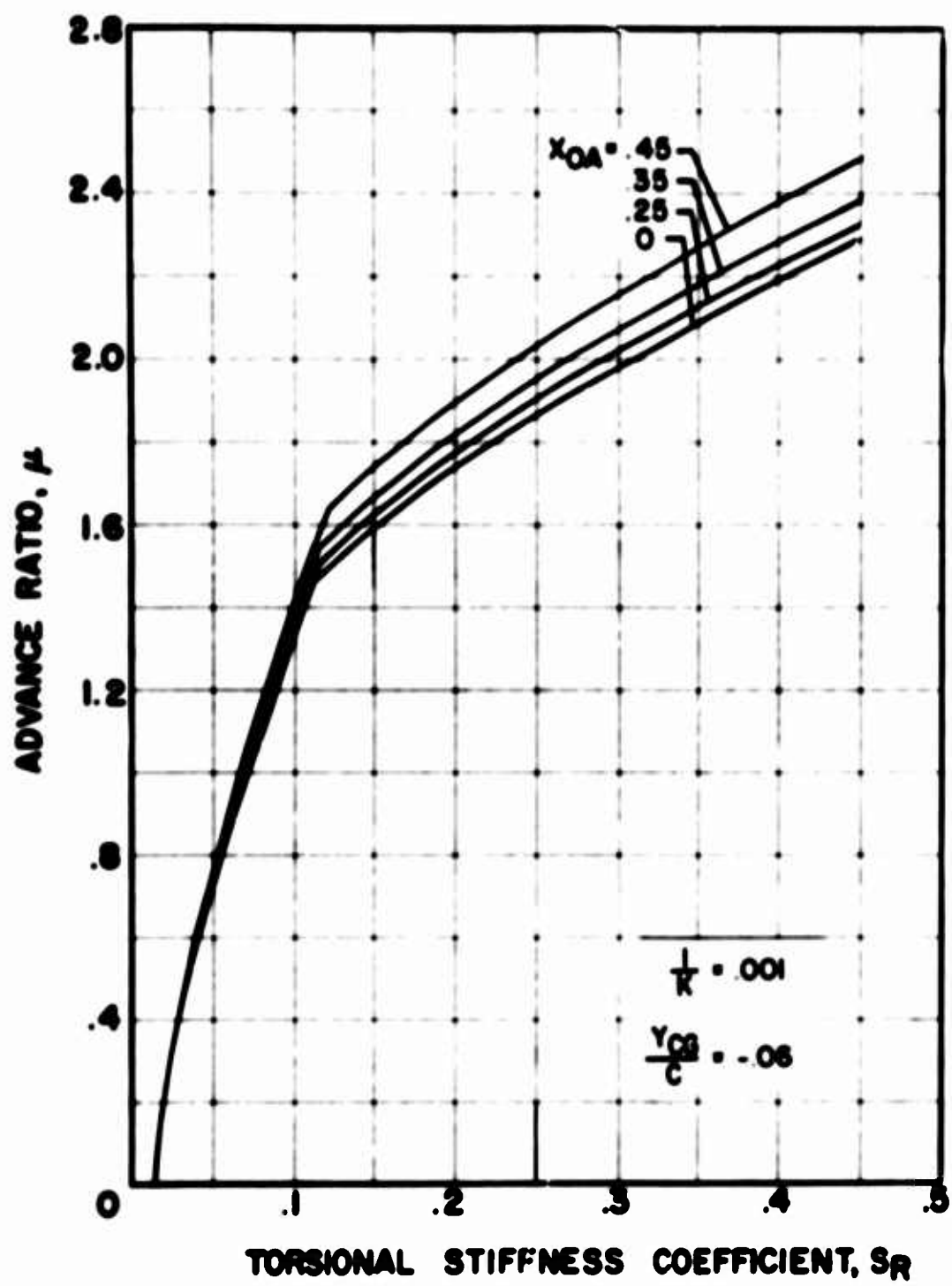


FIGURE 2. CONTINUED.

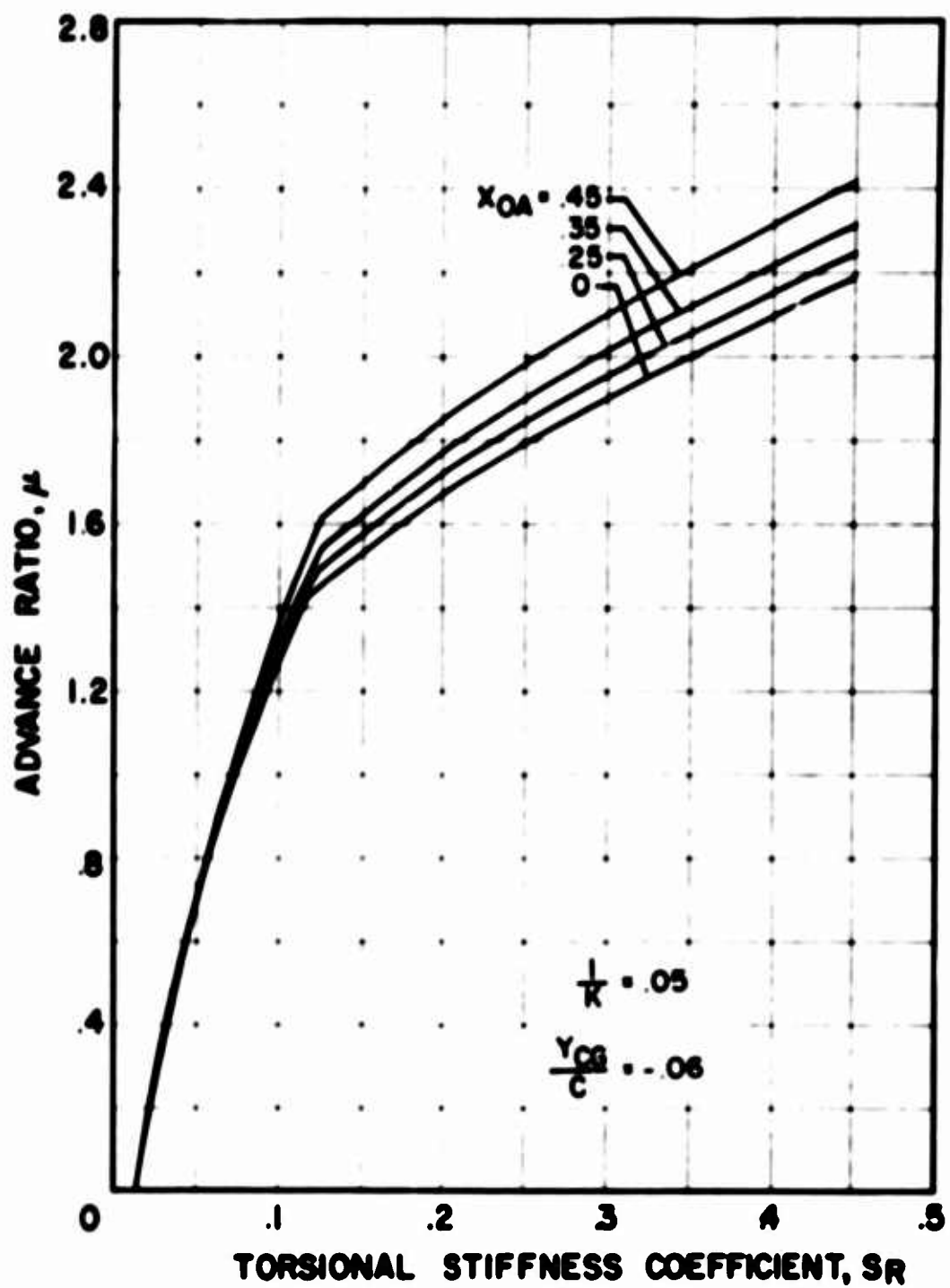


FIGURE 1. ADVANCE RATIO.

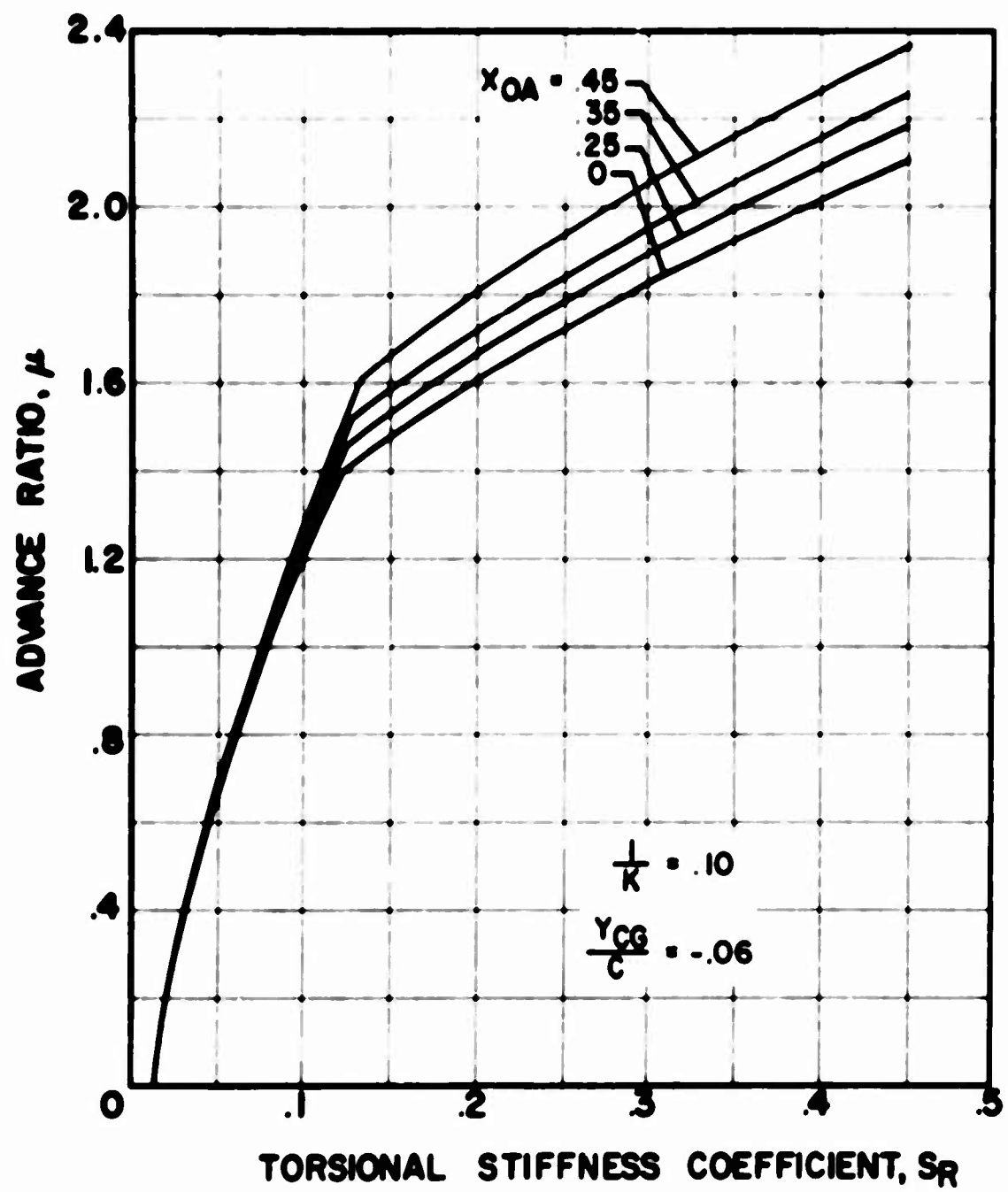


FIGURE 2. CONTINUED.

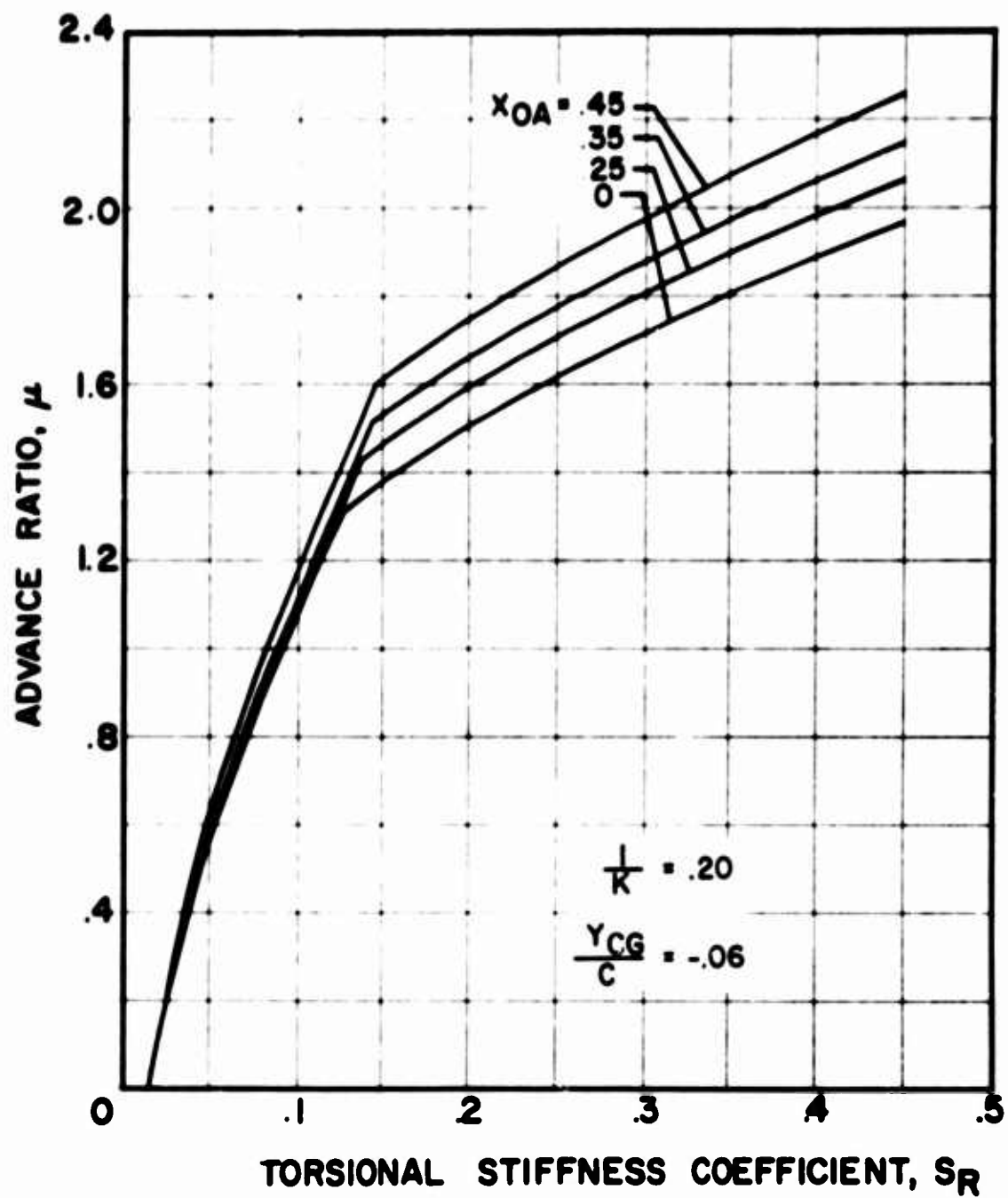


FIGURE 2. CONTINUED.

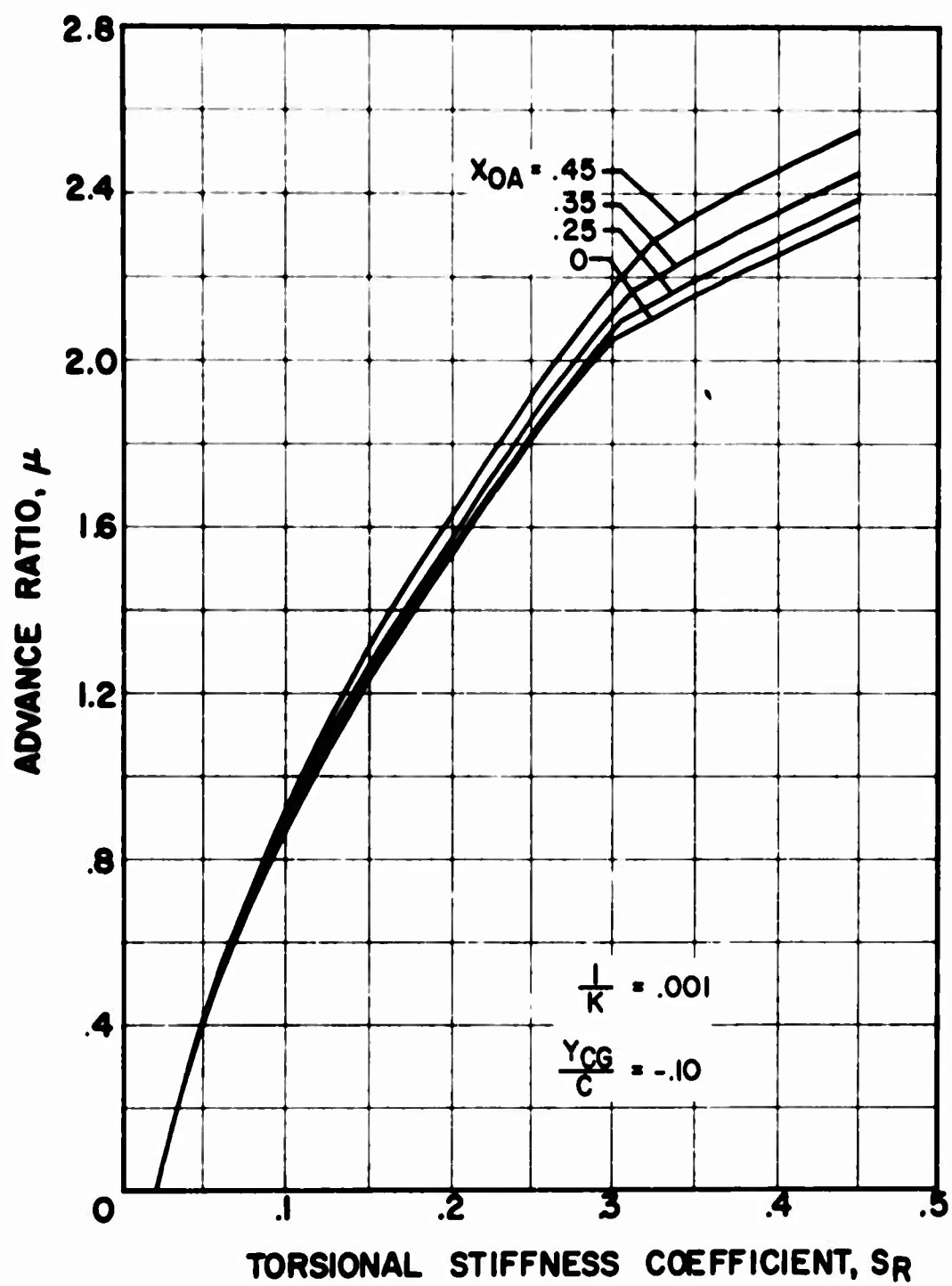


FIGURE 2. CONTINUED.

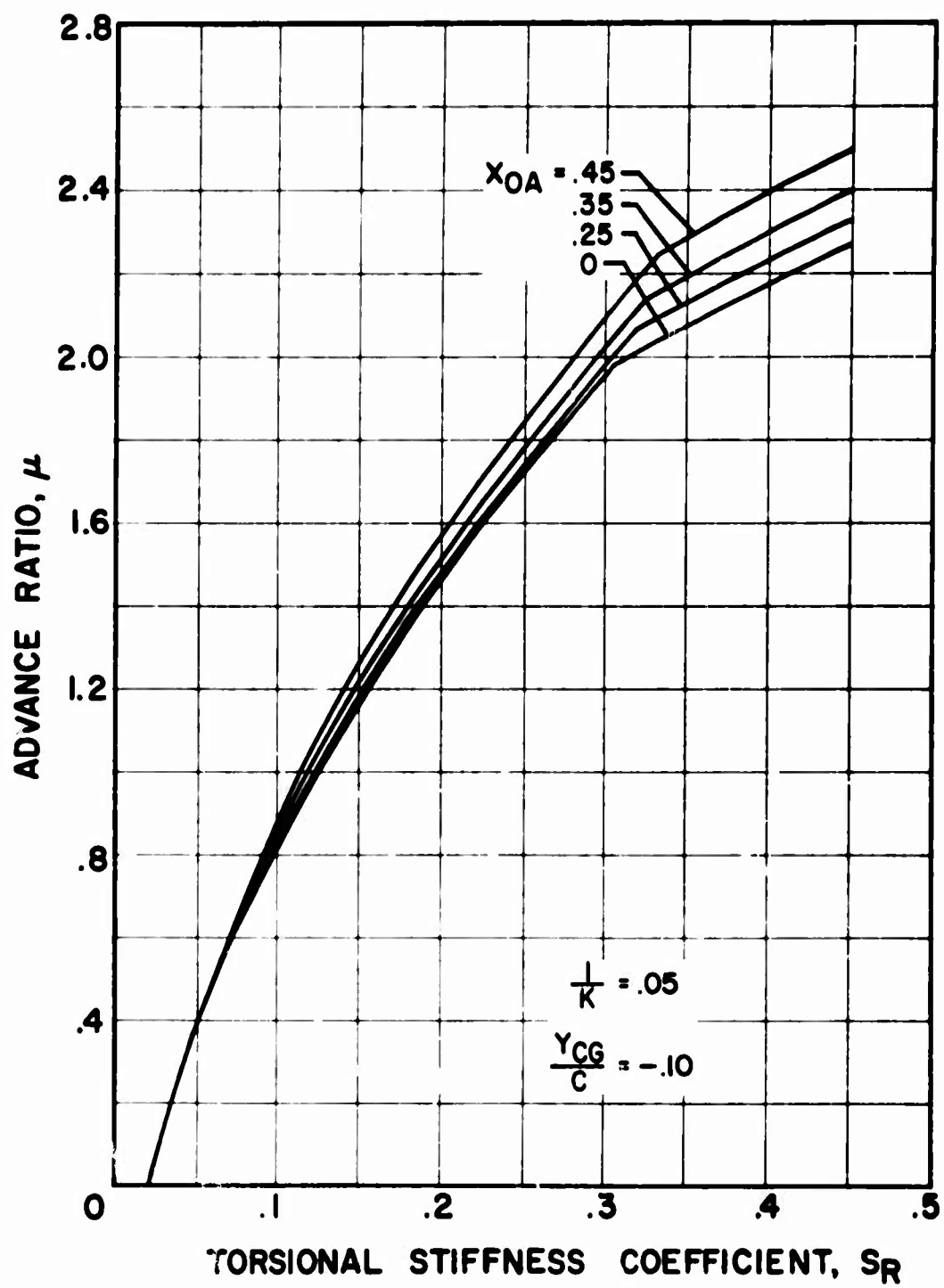


FIGURE 2. CONTINUED.

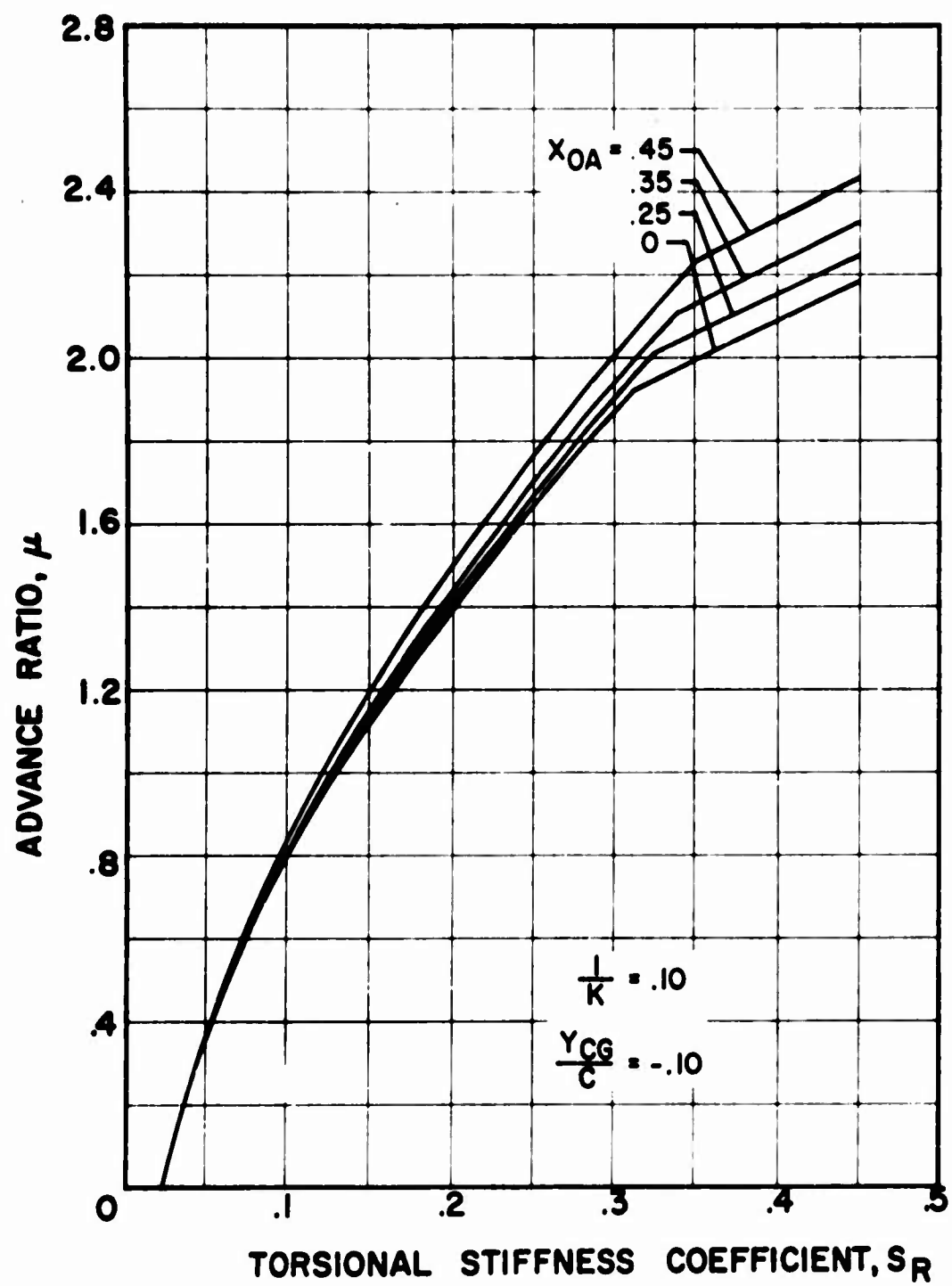


FIGURE 2. CONTINUED.

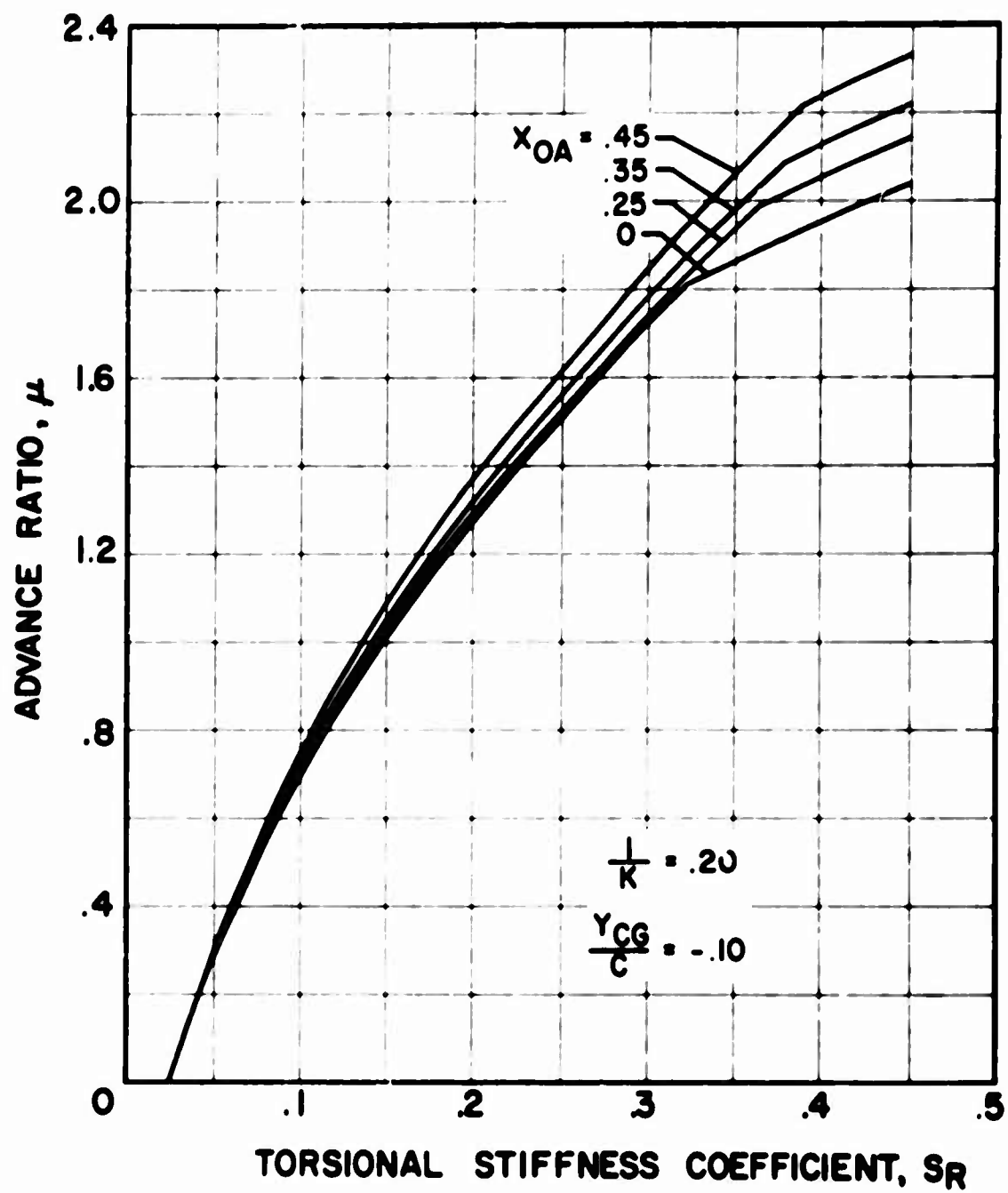


FIGURE 2. CONCLUDED.

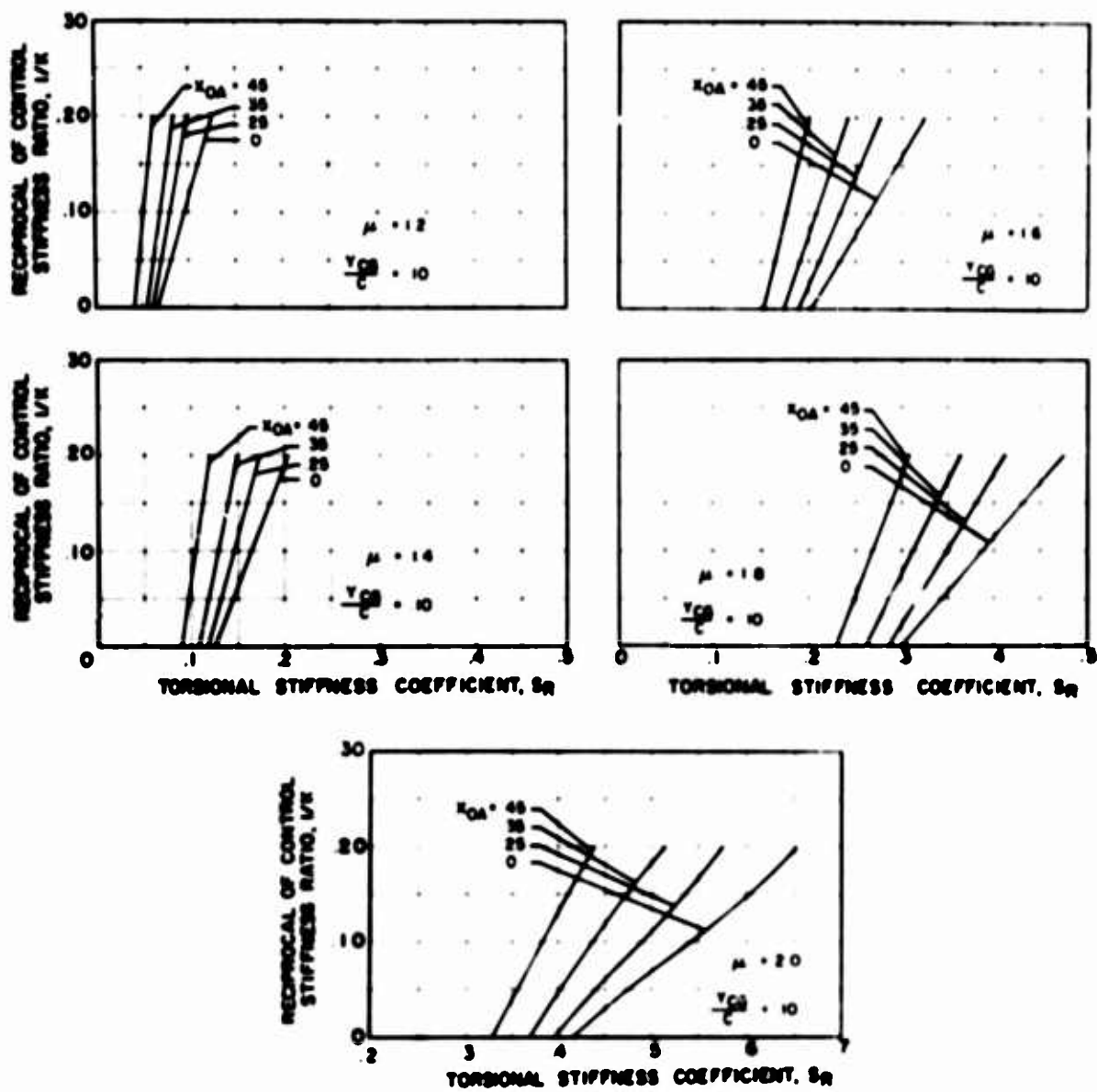


Figure 3. Reciprocal of Control Stiffness Ratio Versus Torsional Stiffness Coefficient; $X_{O3} = 0$, $\omega_0 = 2\pi$.

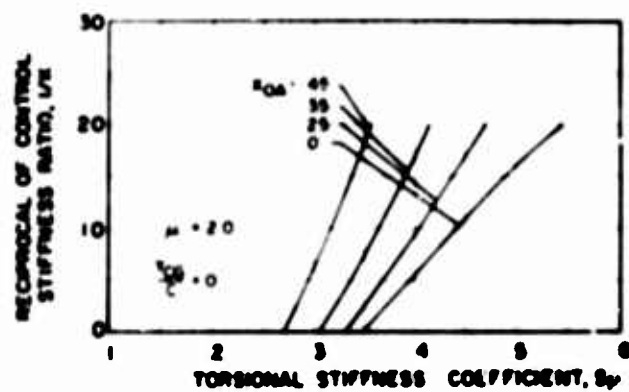
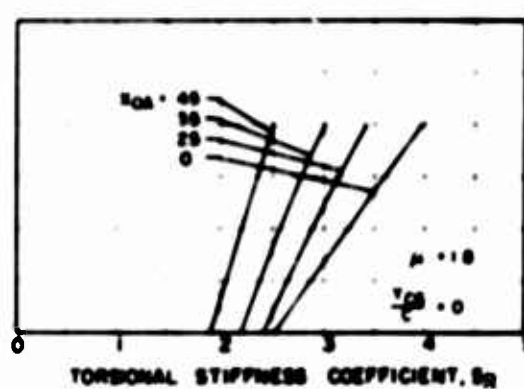
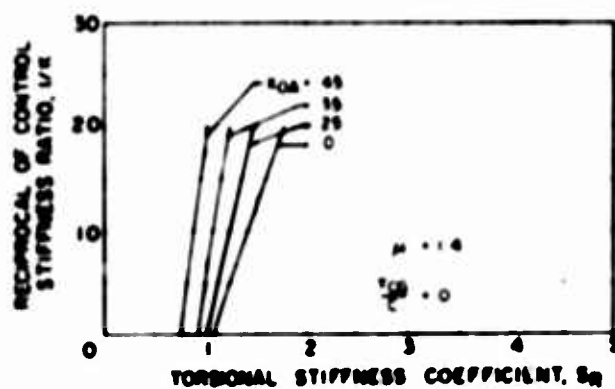
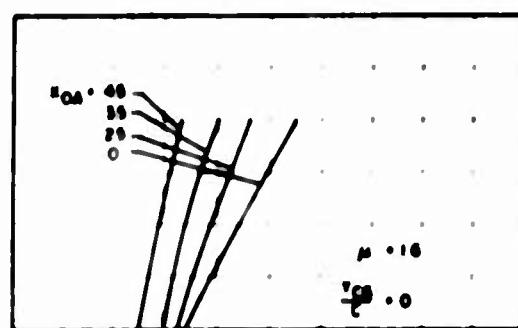
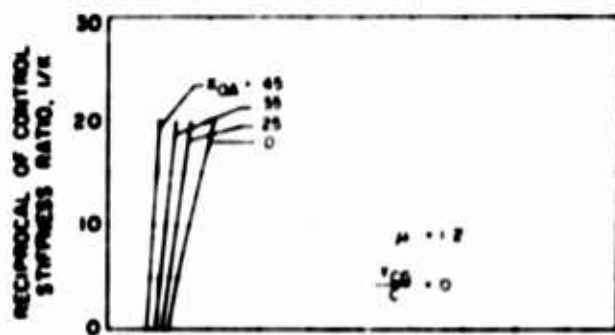


FIGURE 5. (CONTINUED).

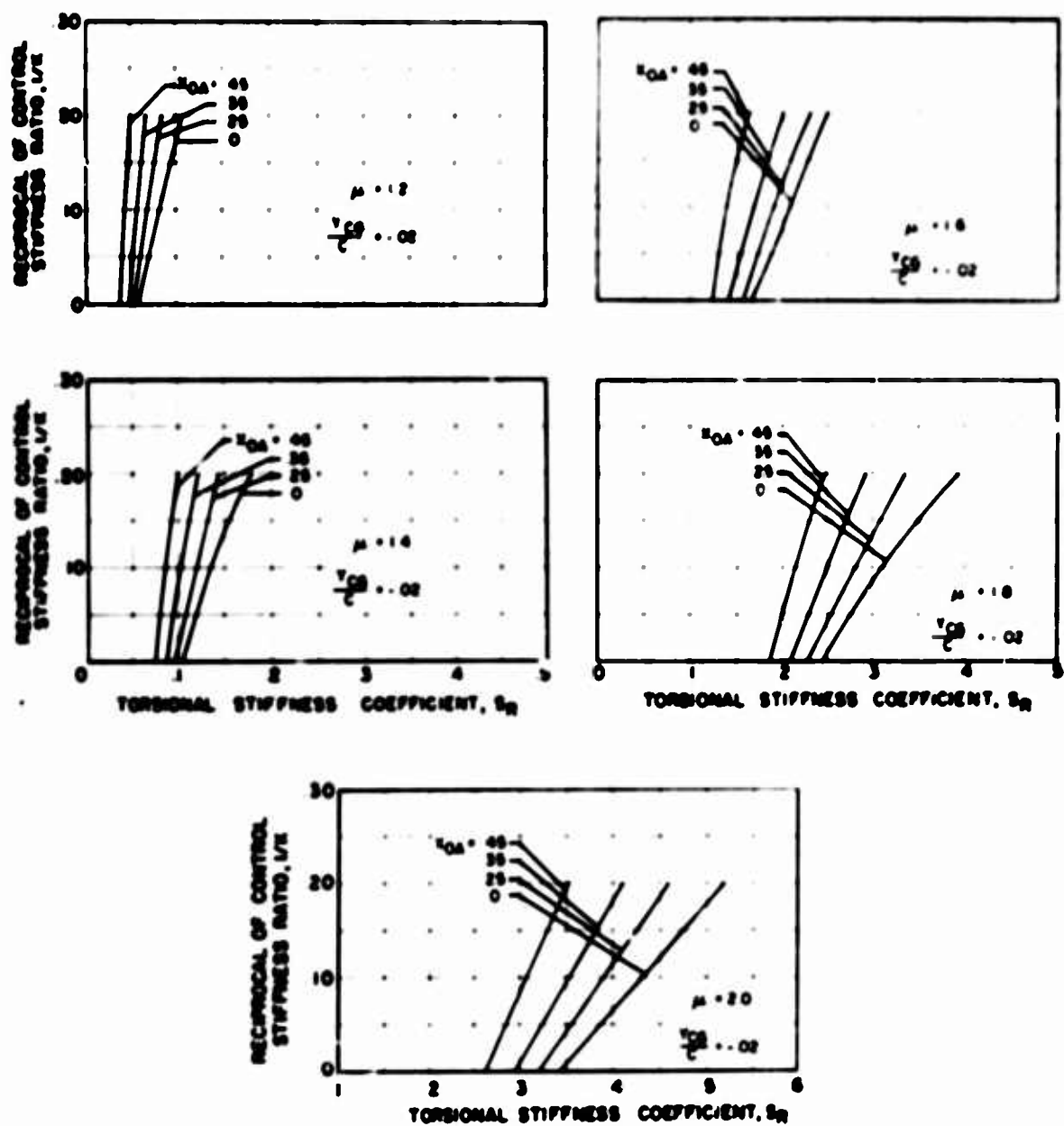


FIGURE 3. CONTINUED.

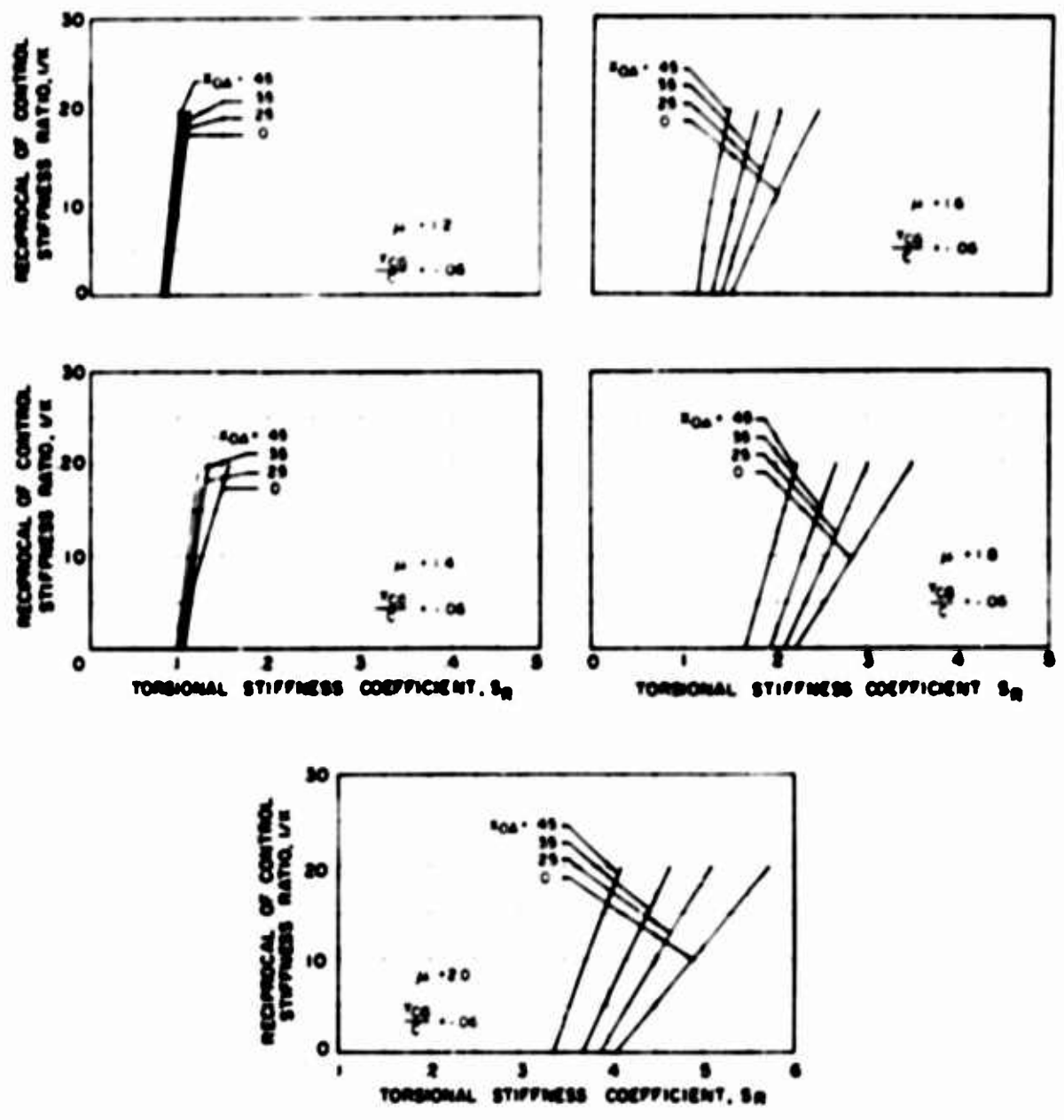


FIGURE 3. CONTINUED.

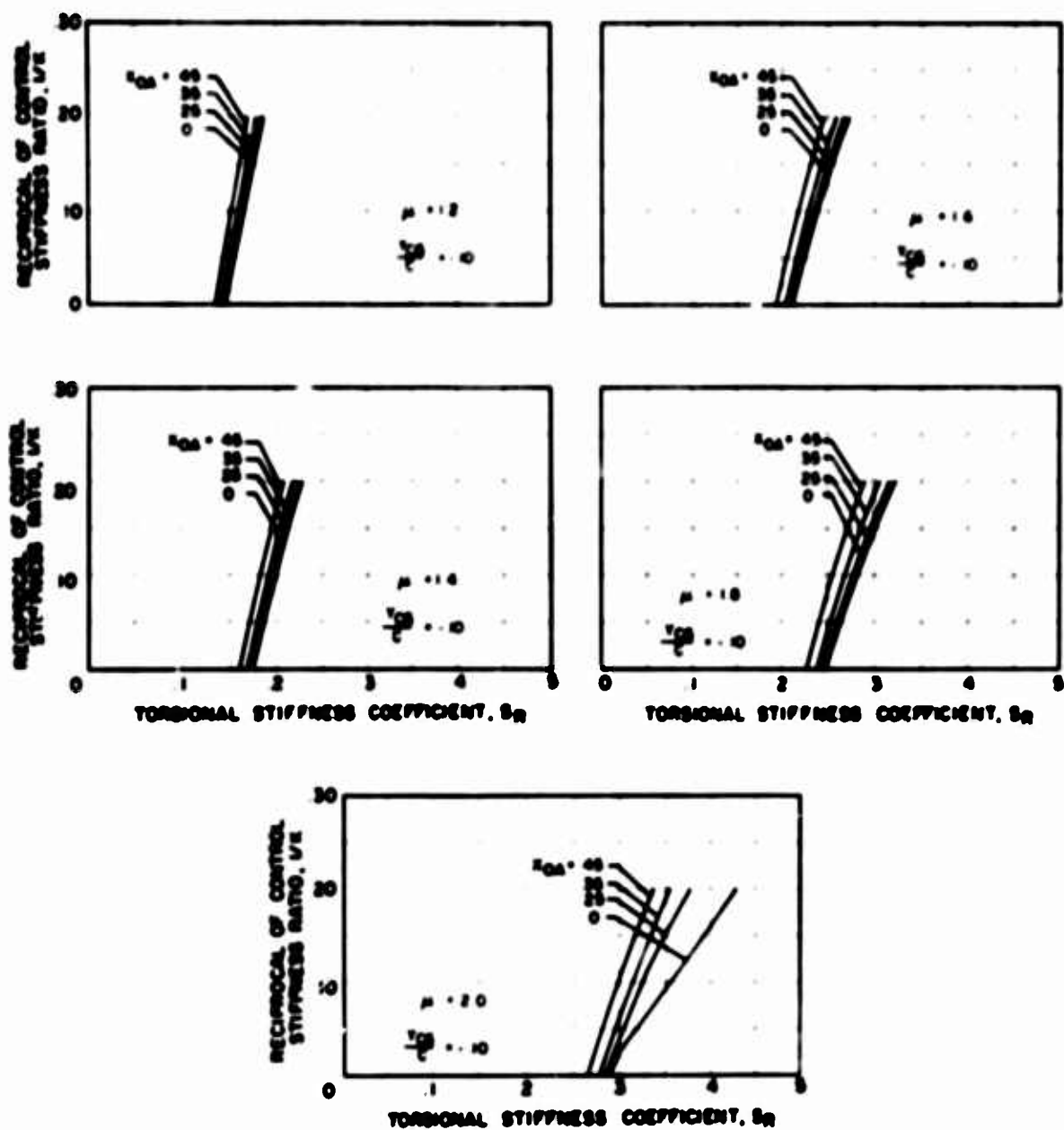


FIGURE 3. (CONCLUDED).

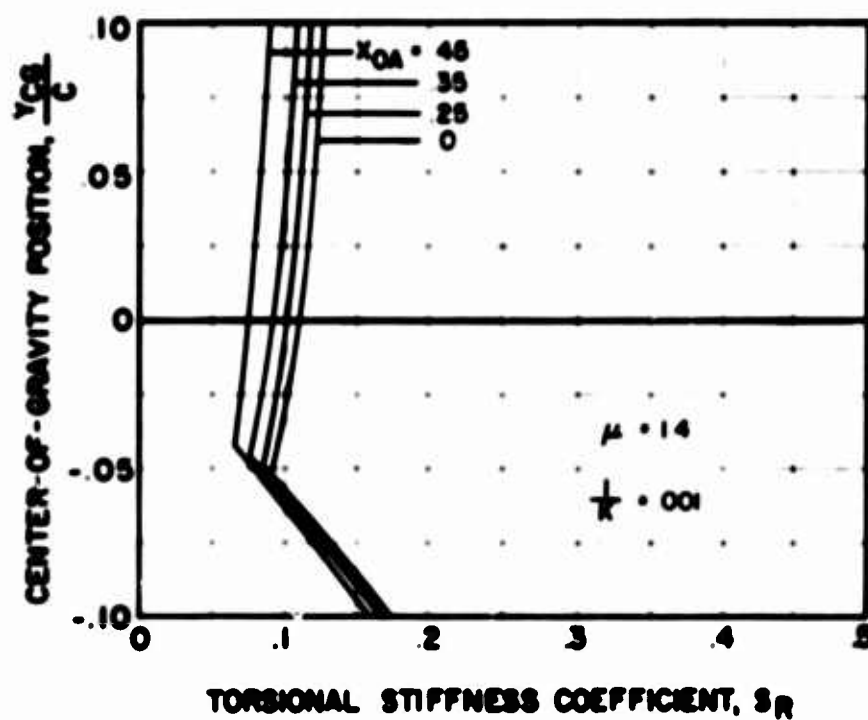
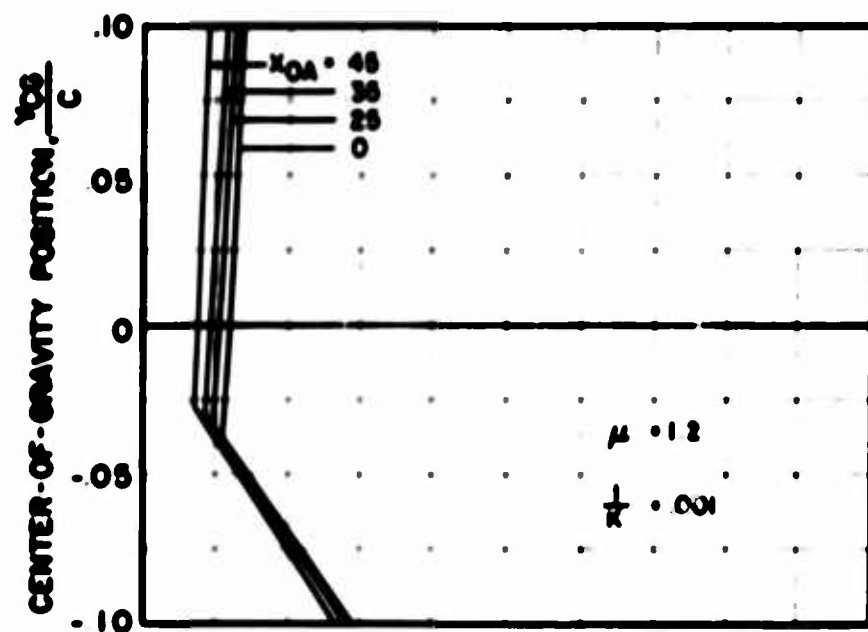


Figure 4. Center-of-Gravity Position With Respect to 25° Chord Versus Torsional Stiffness Coefficient;
 $x_{OA} = 0$, $\phi_0 = 2\pi$

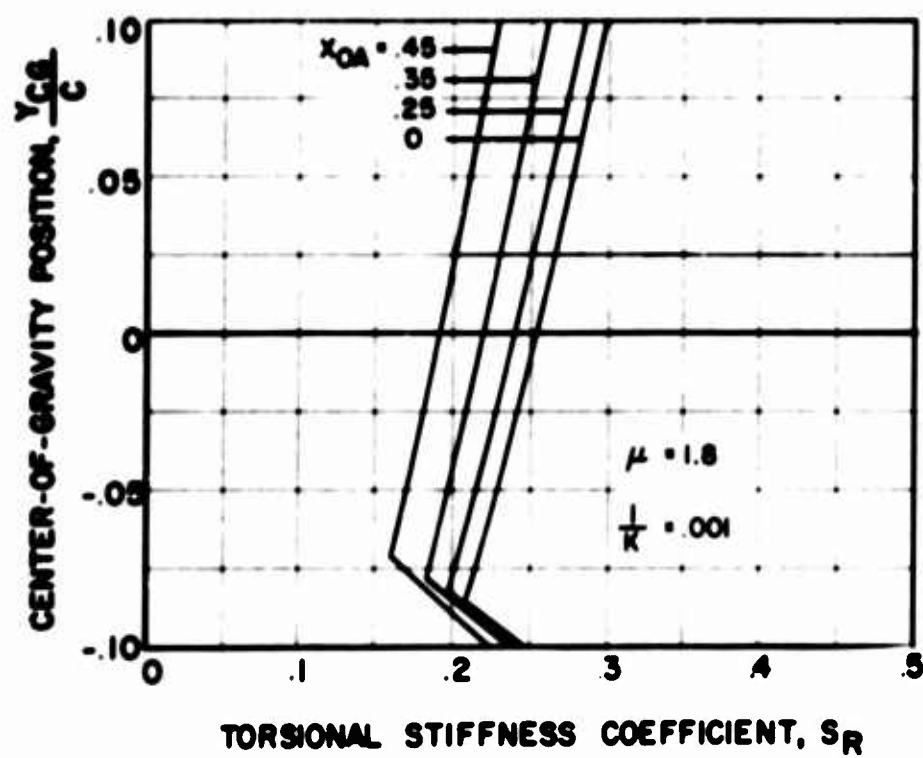
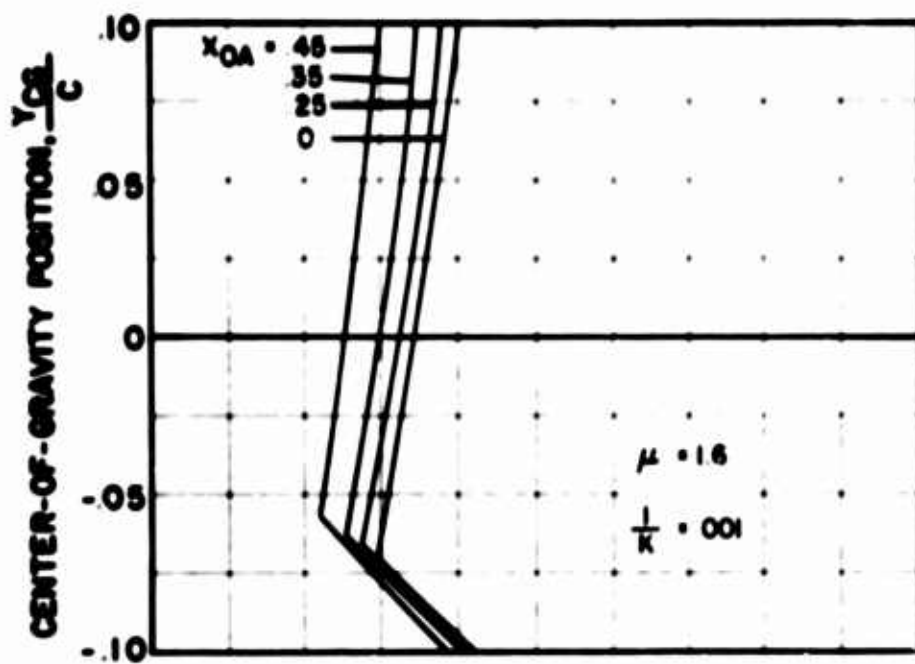


FIGURE 4. CONTINUED.

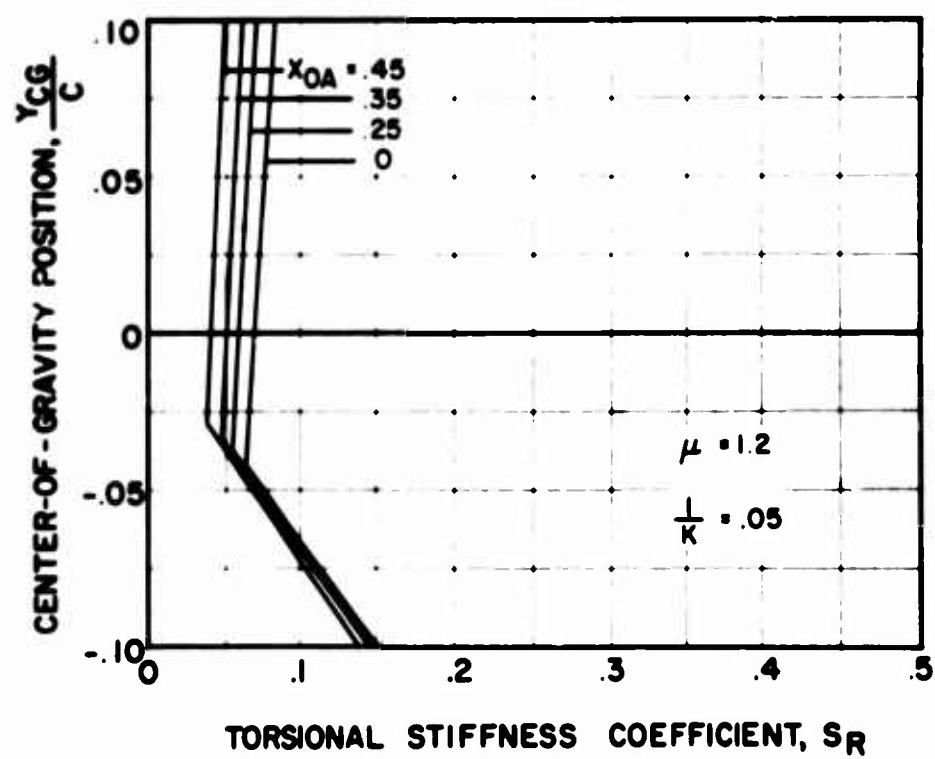
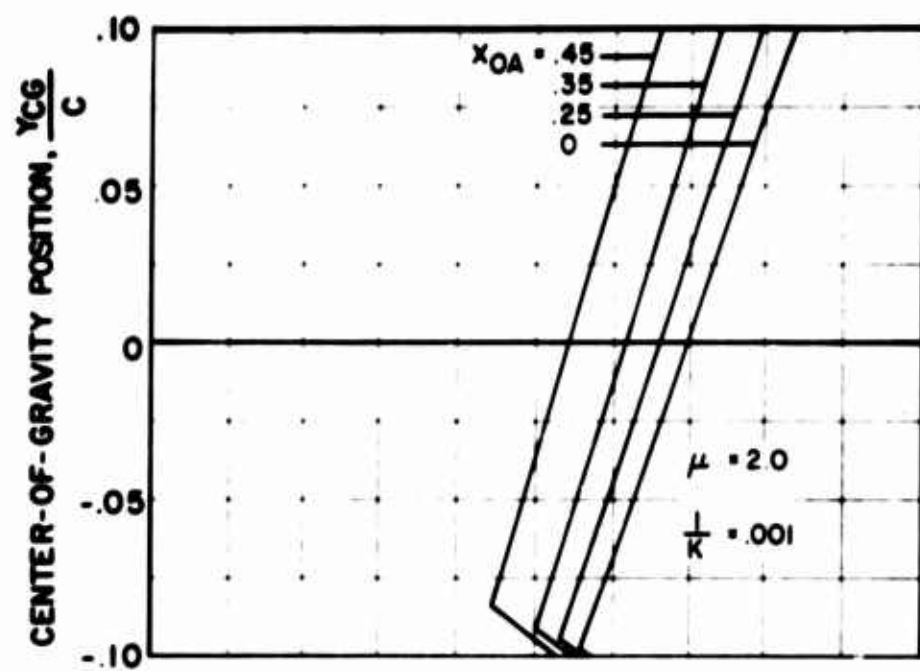


FIGURE 4. CONTINUED.

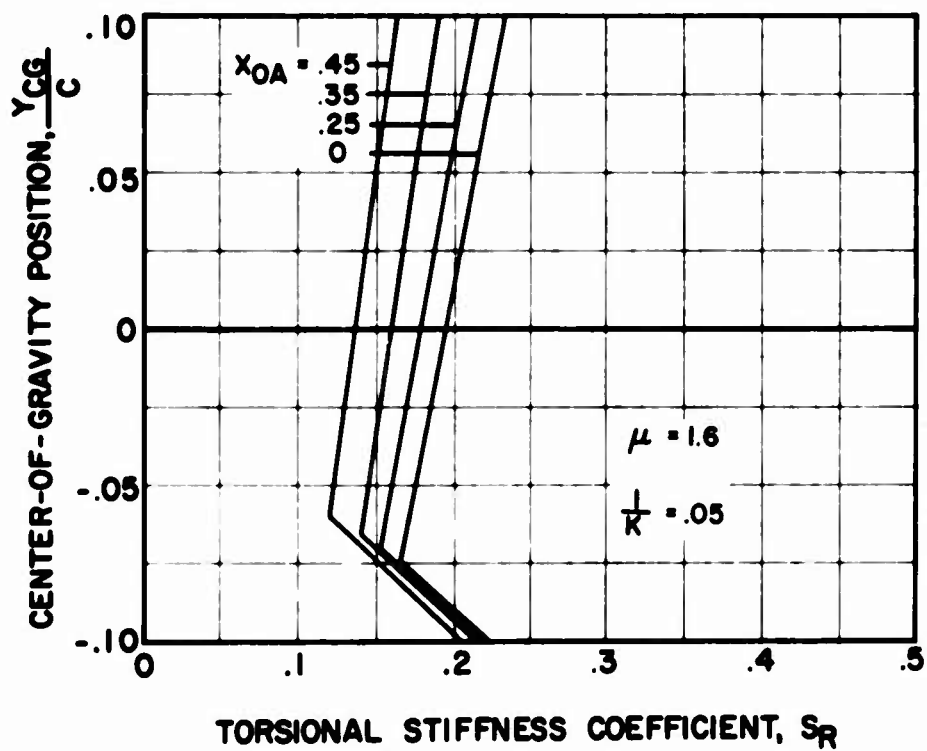
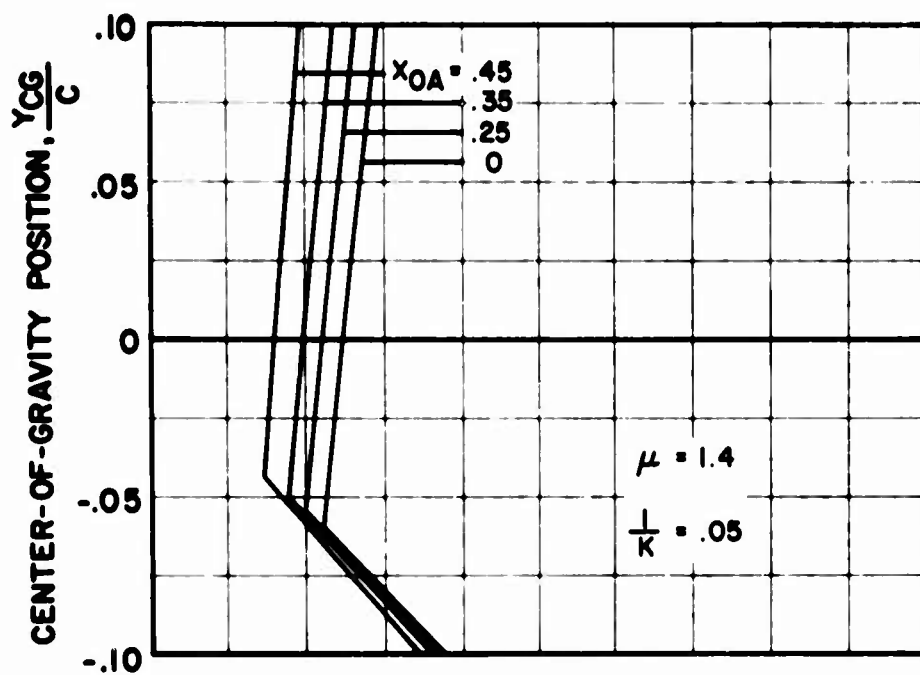


FIGURE 4. CONTINUED.

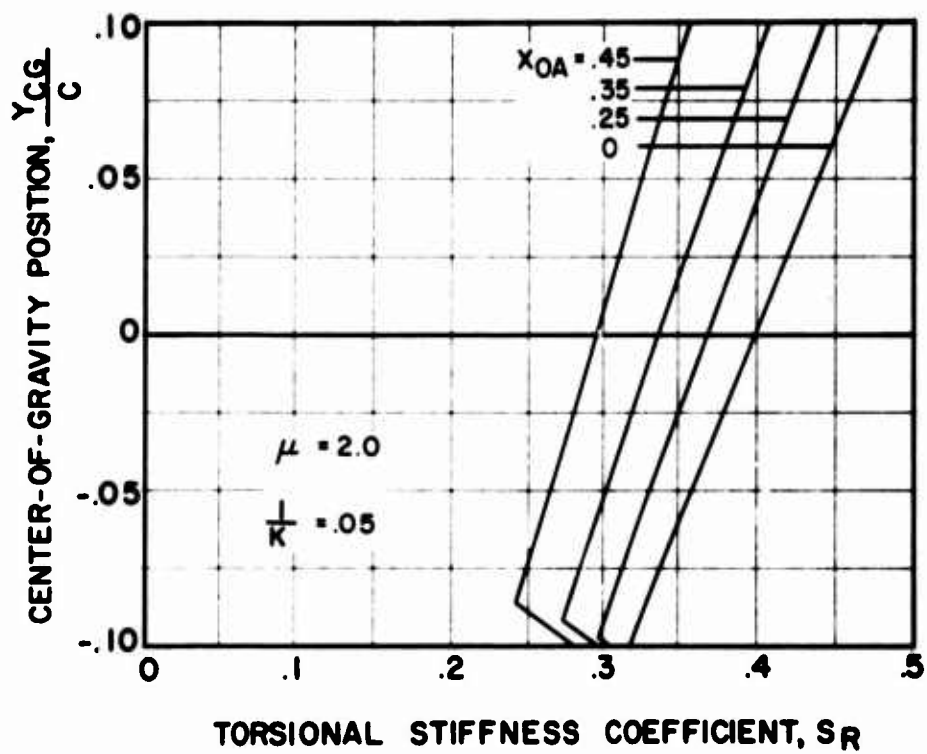
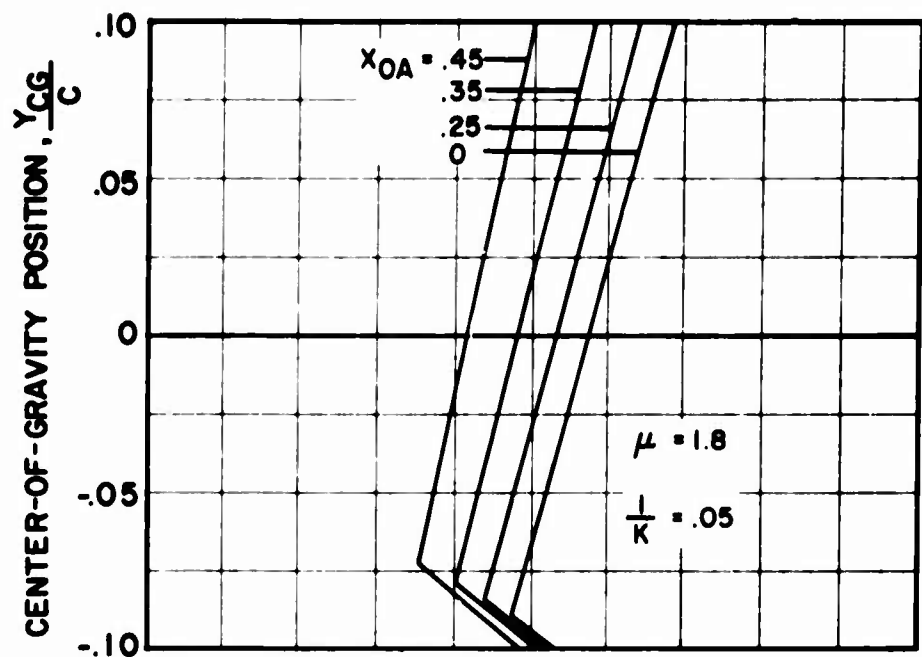


FIGURE 4. CONTINUED.

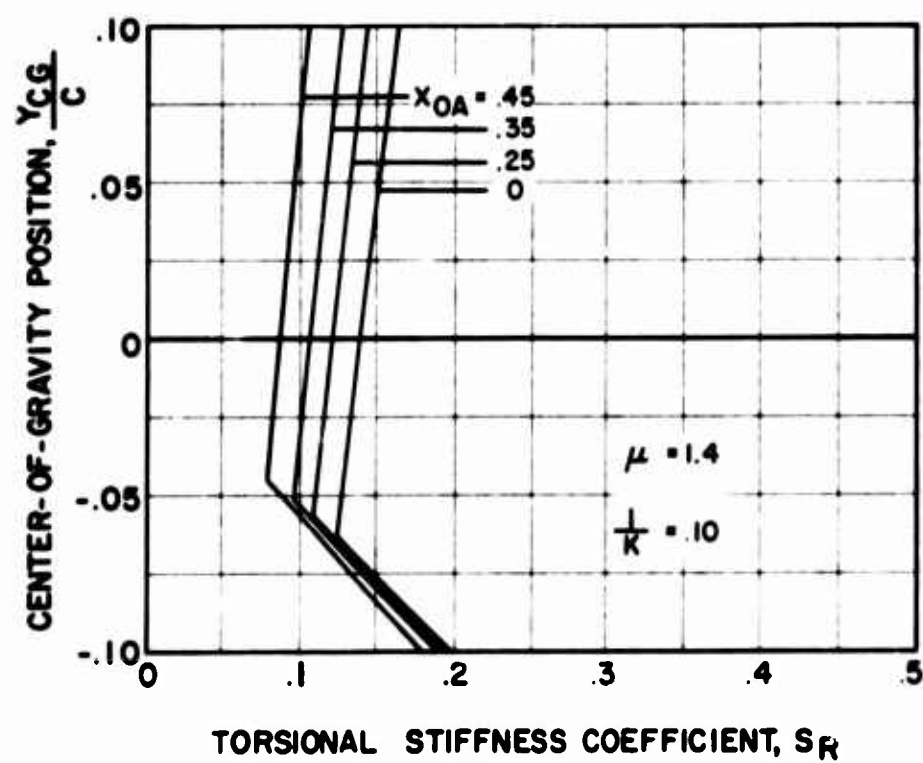
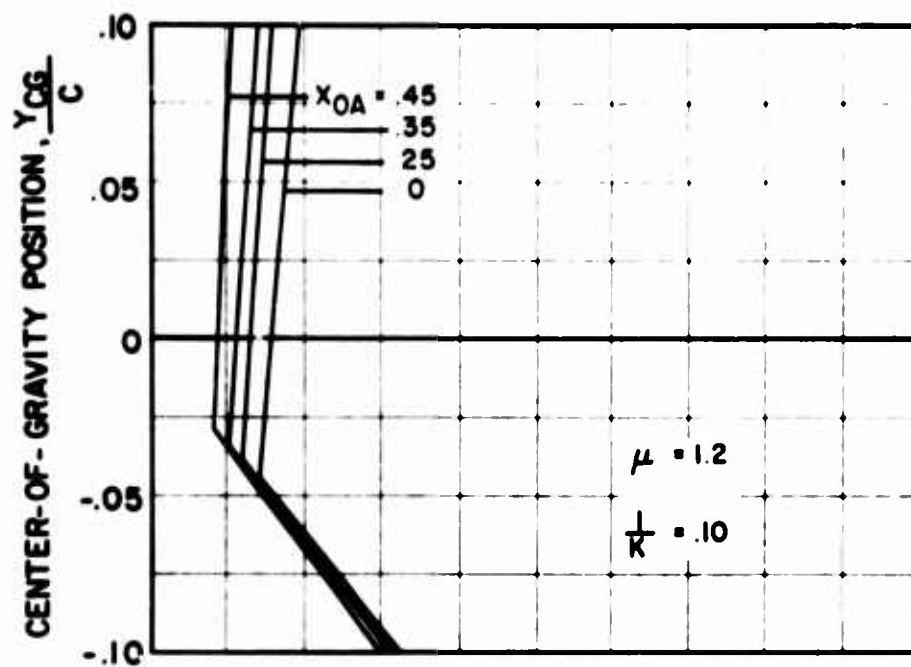


FIGURE 4. CONTINUED.

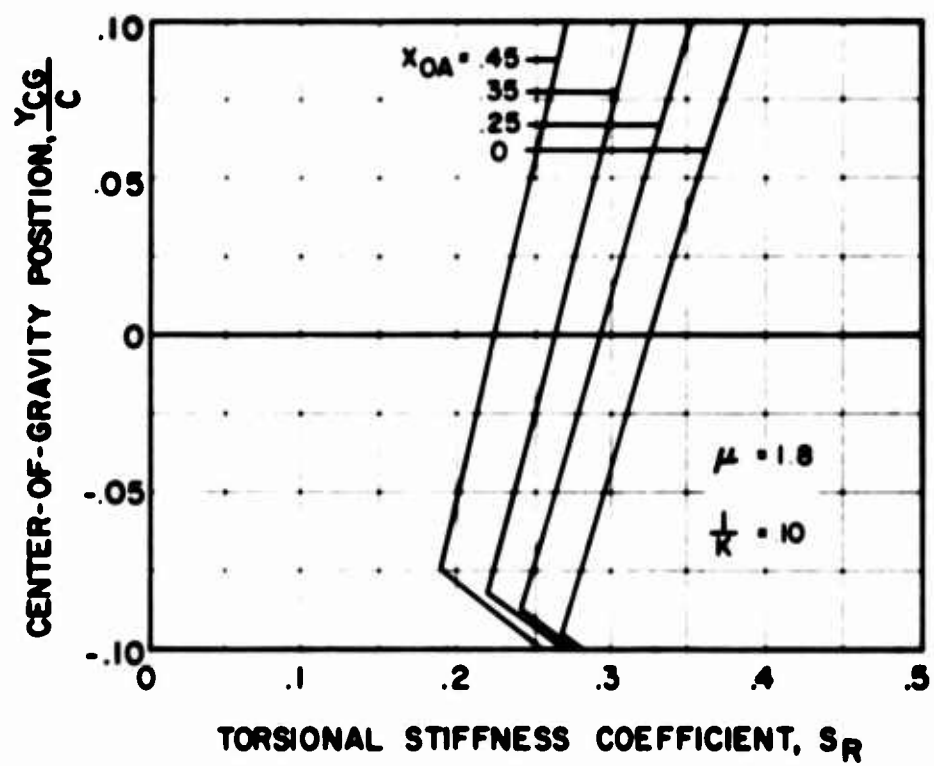
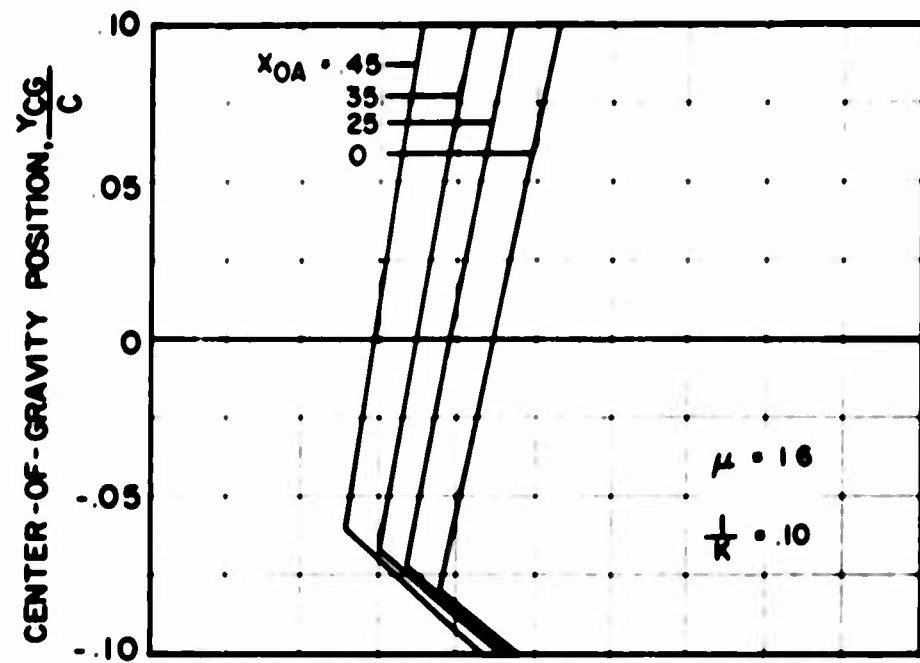


FIGURE 4. CONTINUED.

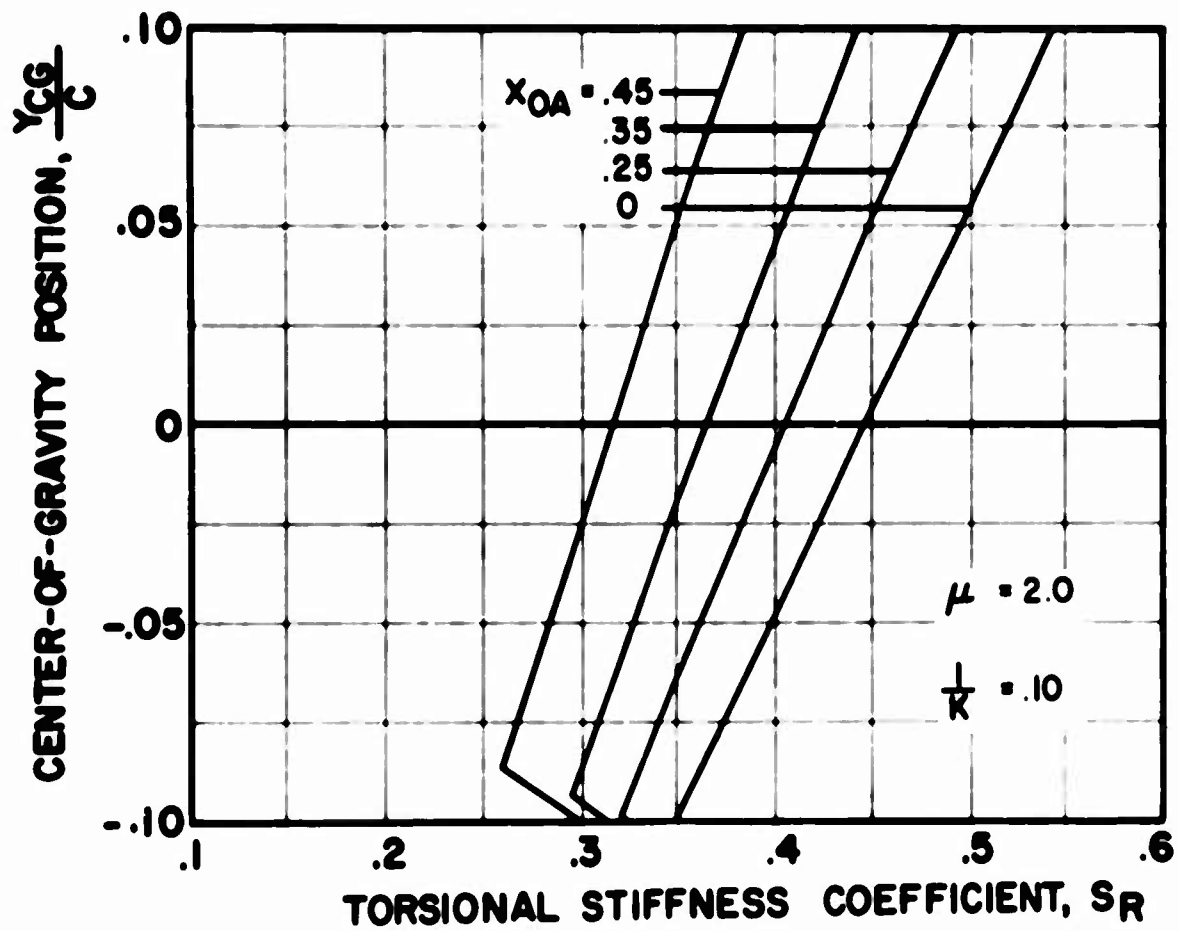


FIGURE 4. CONTINUED.

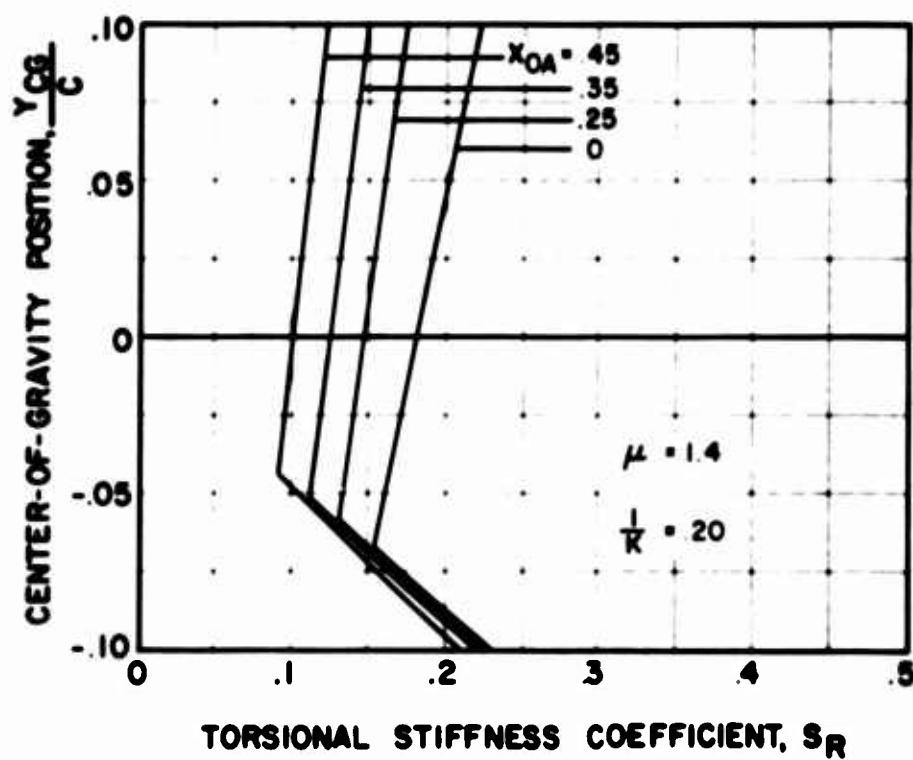
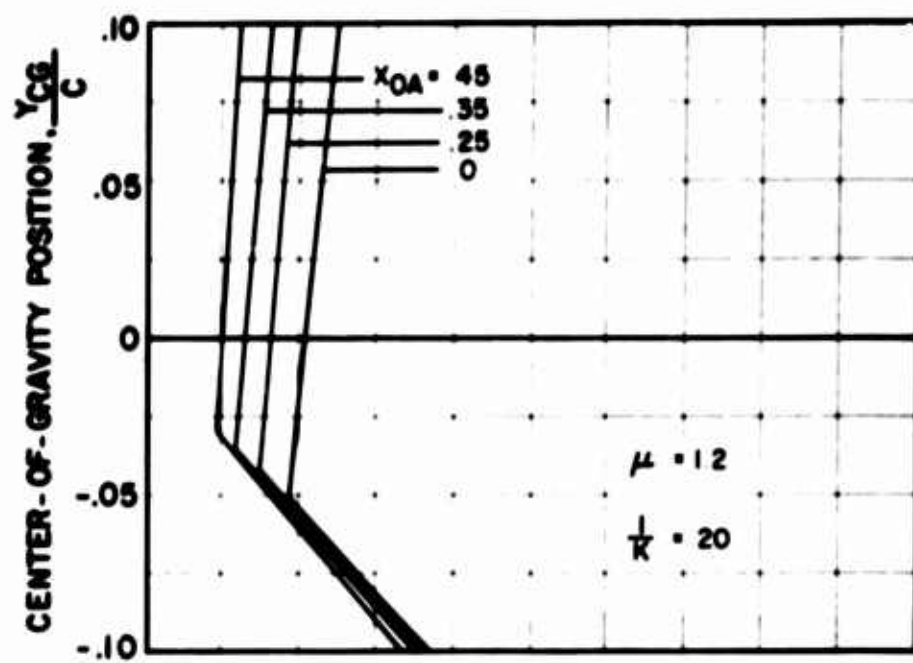


FIGURE 4. CONTINUED.

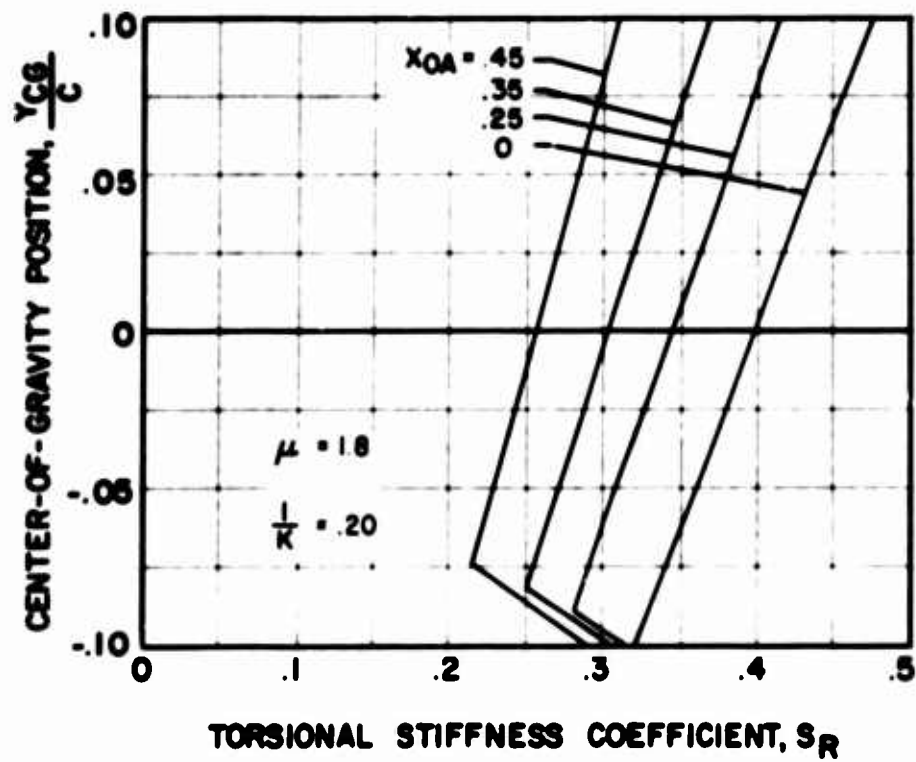
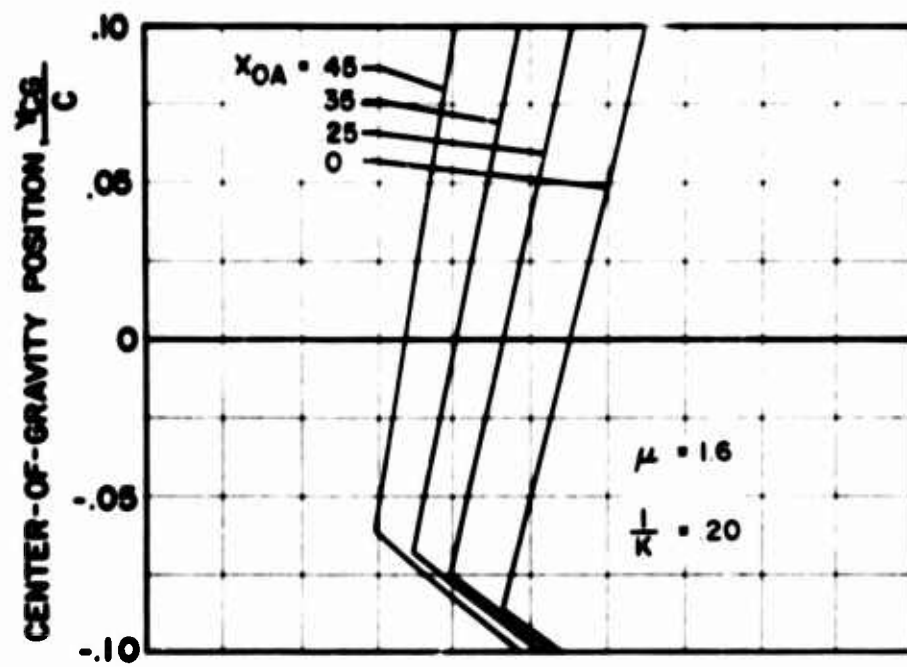


FIGURE 4. CONTINUED.

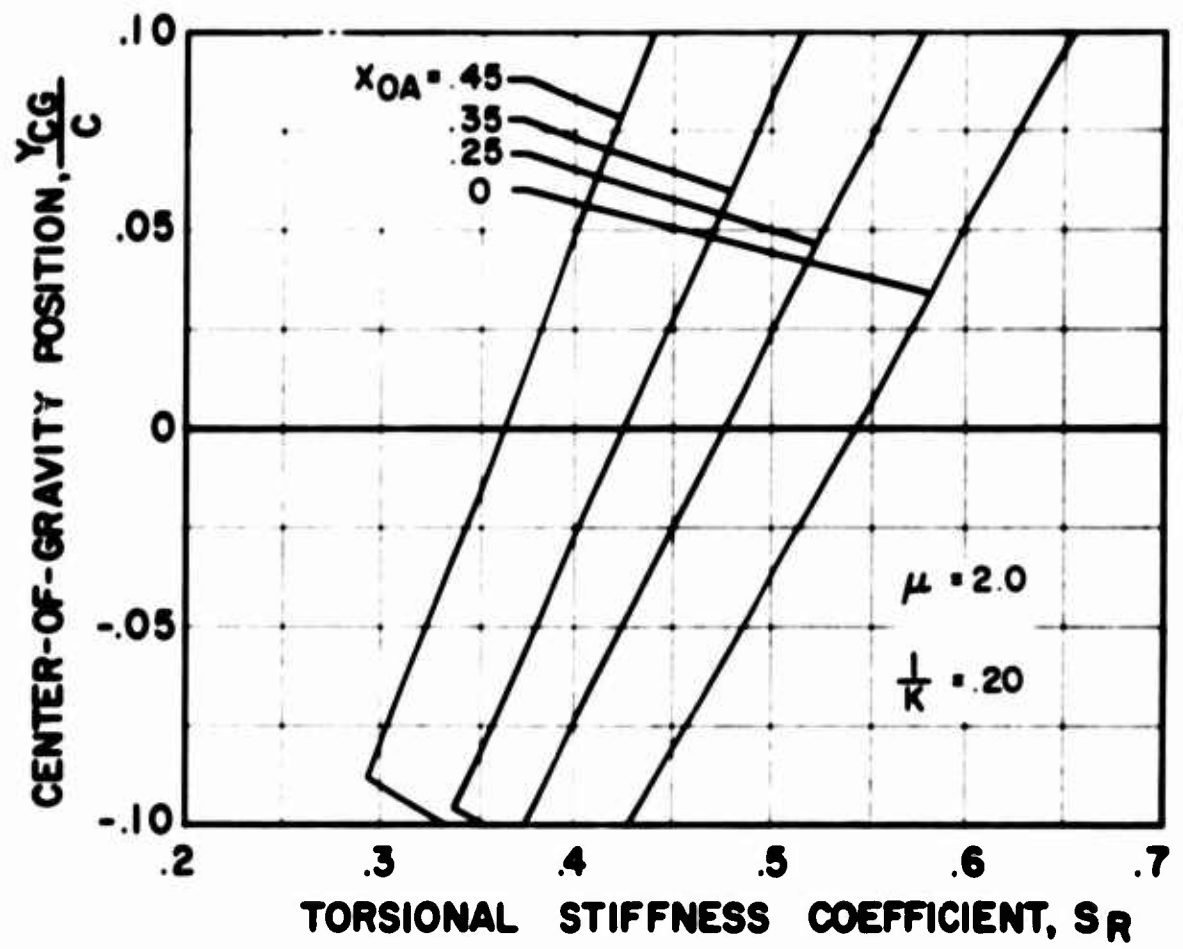


FIGURE 4. CONCLUDED.

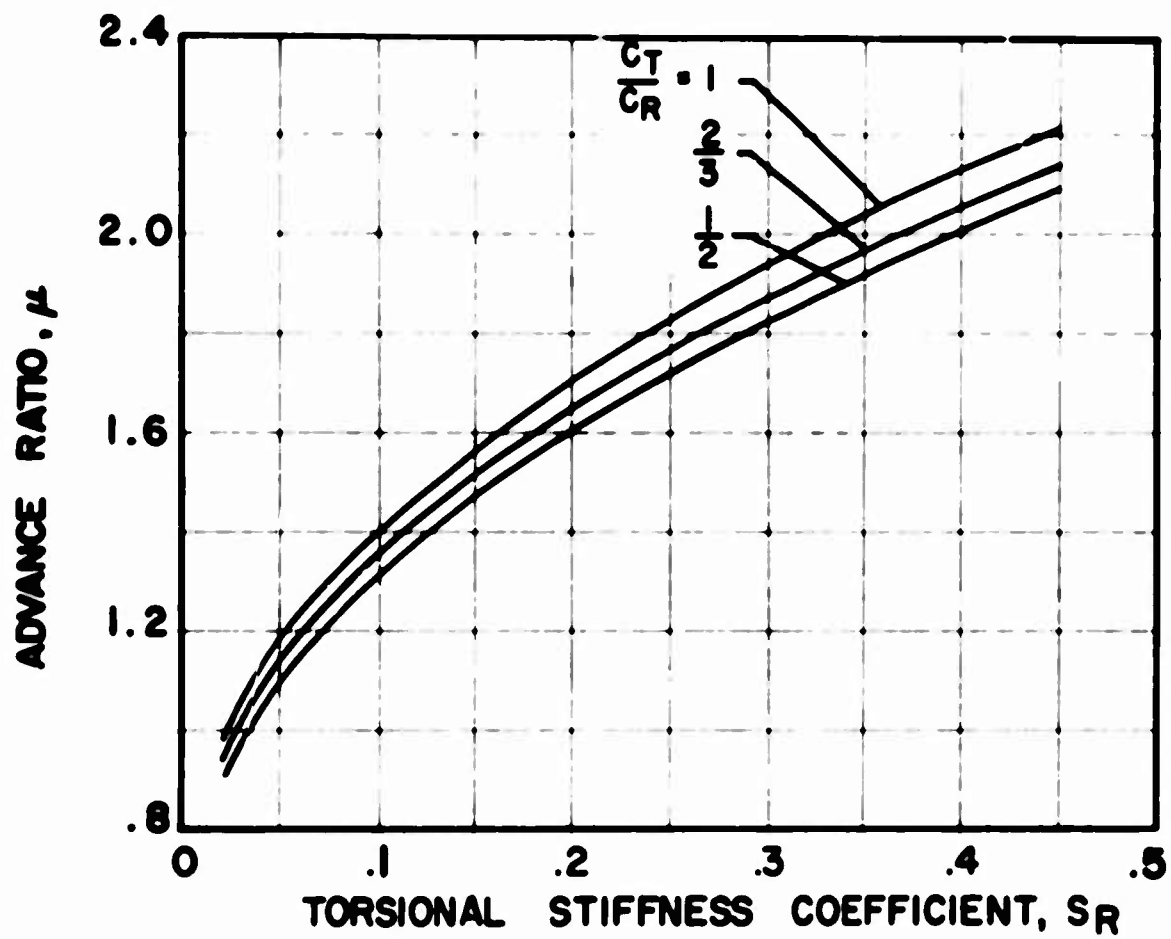


Figure 5. Effect of Linear Variation in Chord on Retreating Blade Torsional Divergence ; $1/K = \infty$, $Y_{CG}/C = 0$, $X_{OA} = .25$, $X_{OC} = 0$, $\alpha_0 = 2\pi$.

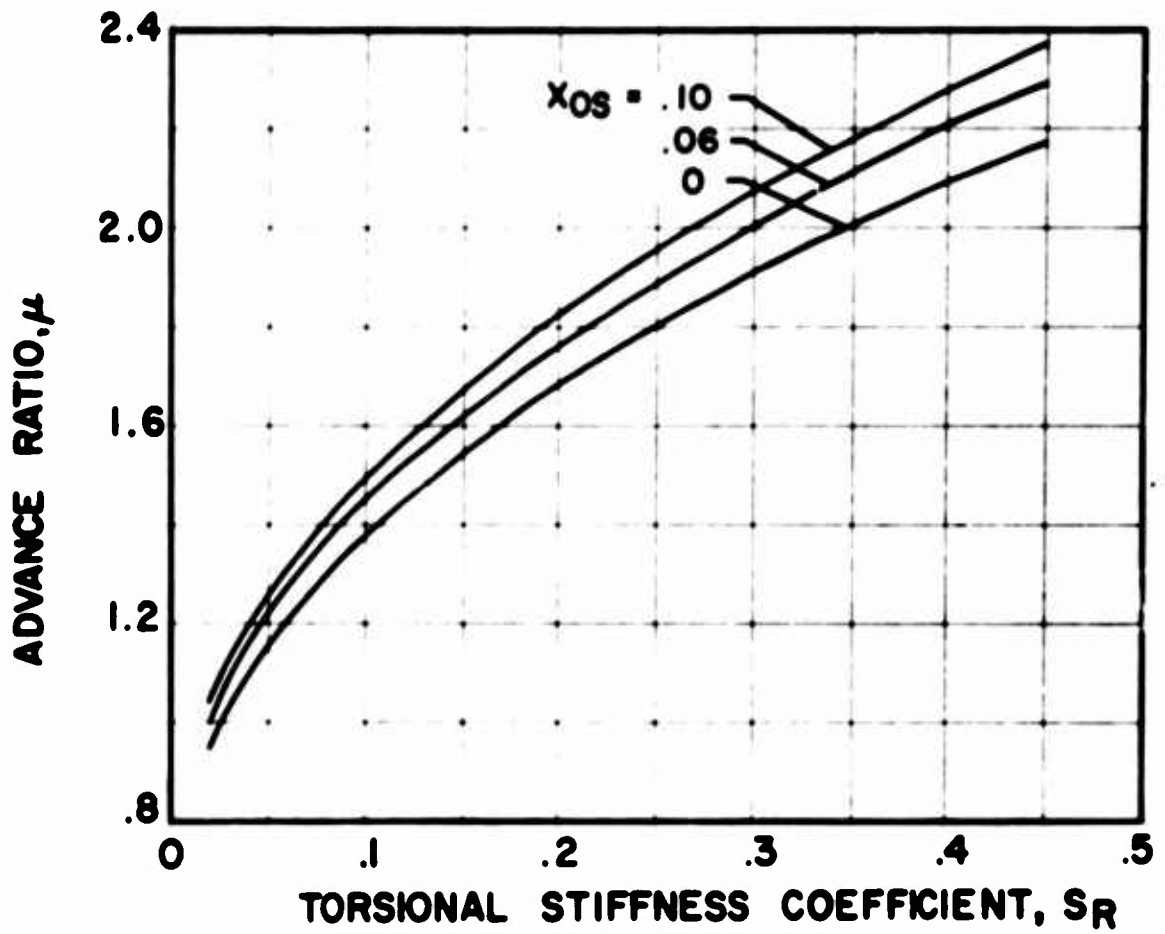


Figure 6. Effect of Structural Cutout on Retreating Blade Torsional Divergence; $1/K = .001$, $Y_{CG}/C = 0$, $X_{OA} = 0$, $\alpha_0 = 2\pi$.

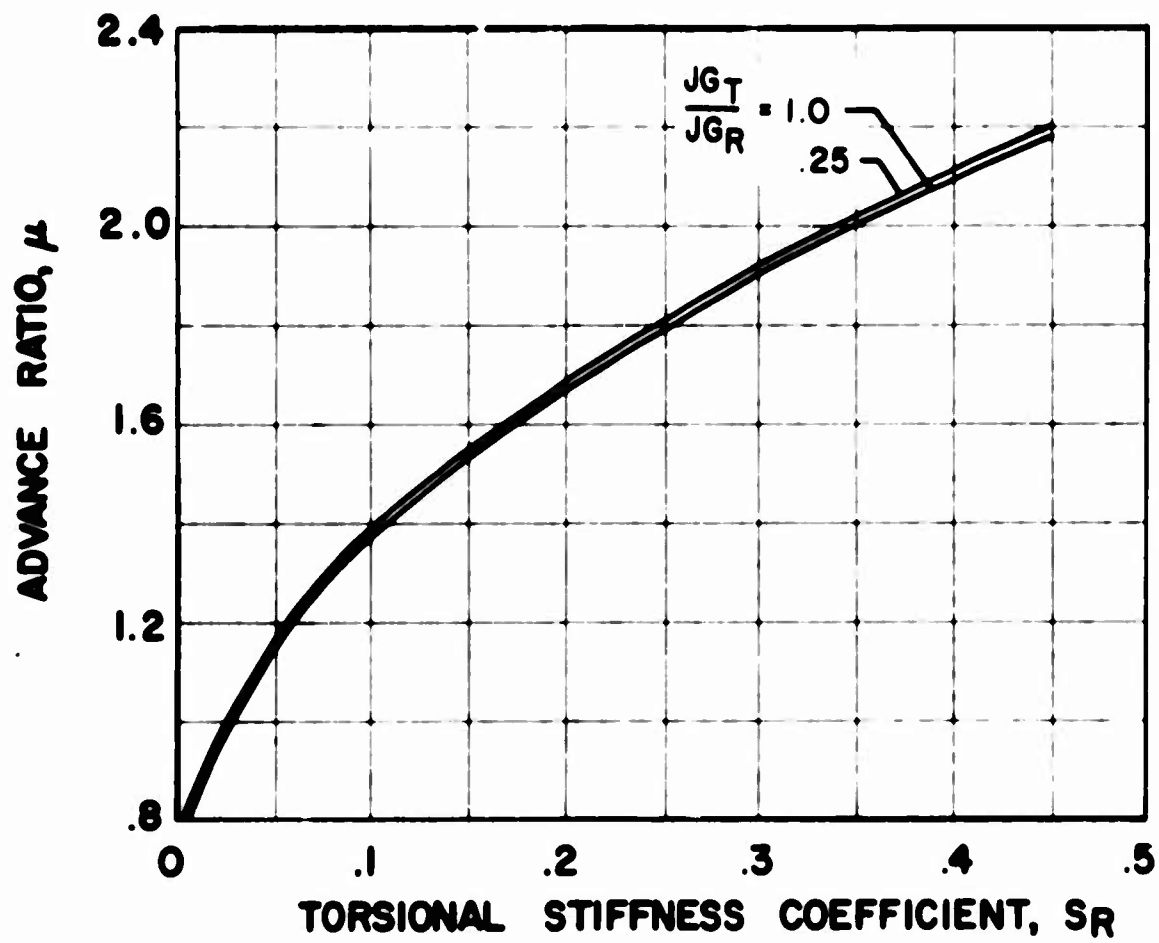


Figure 7. Effect of Linear Variation in Stiffness on Retreating Blade Torsional Divergence; $l/K = .001$, $Y_{CG}/C = 0$, $X_{0A} = 0$, $X_{0S} = 0$, $\alpha_0 = 2\pi$.

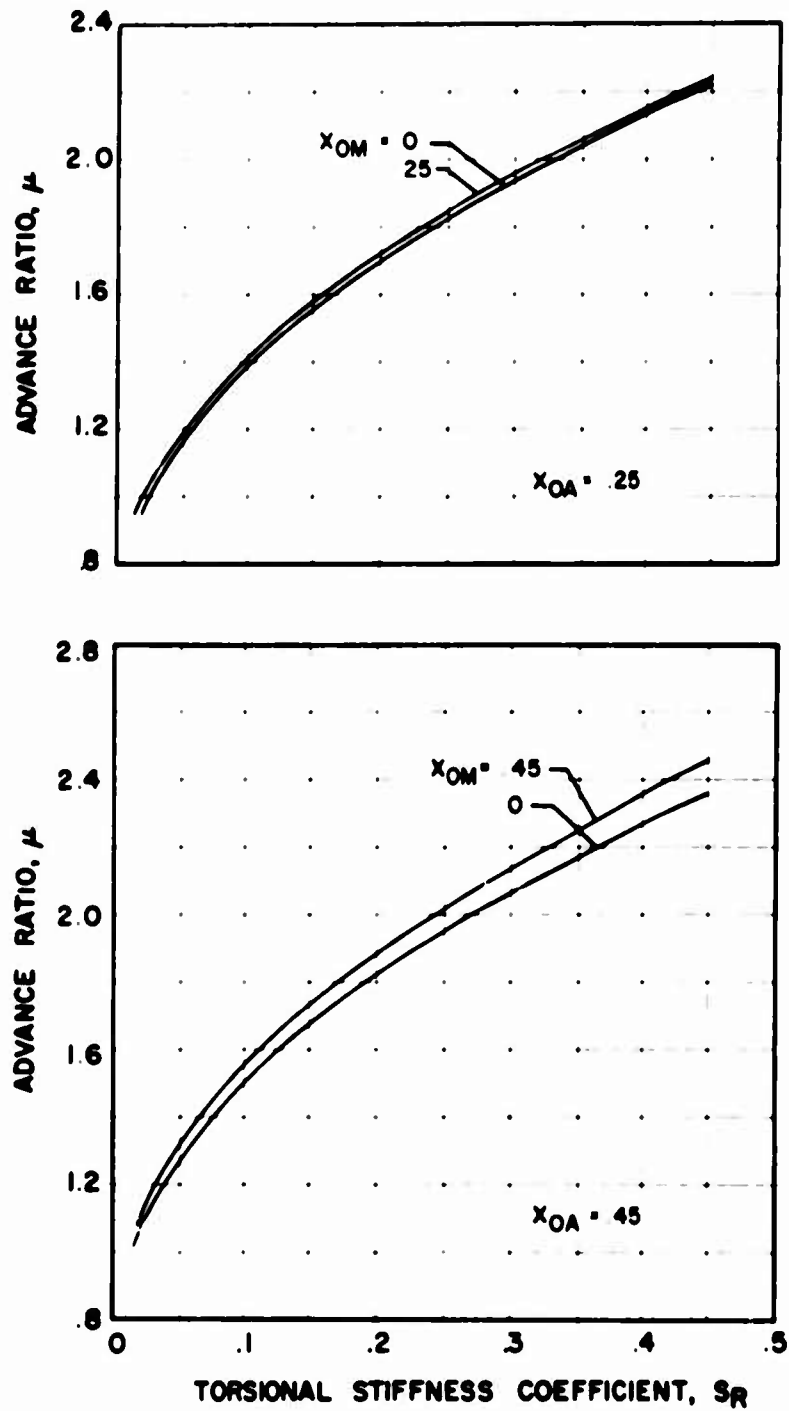


Figure 8. Effect of Inertial Cutout on Retreating Blade Torsional Divergence, $1/K = .001$, $Y_{CG}/C = 0$, $X_{O3} = 0$, $\alpha_0 = 2\pi$.

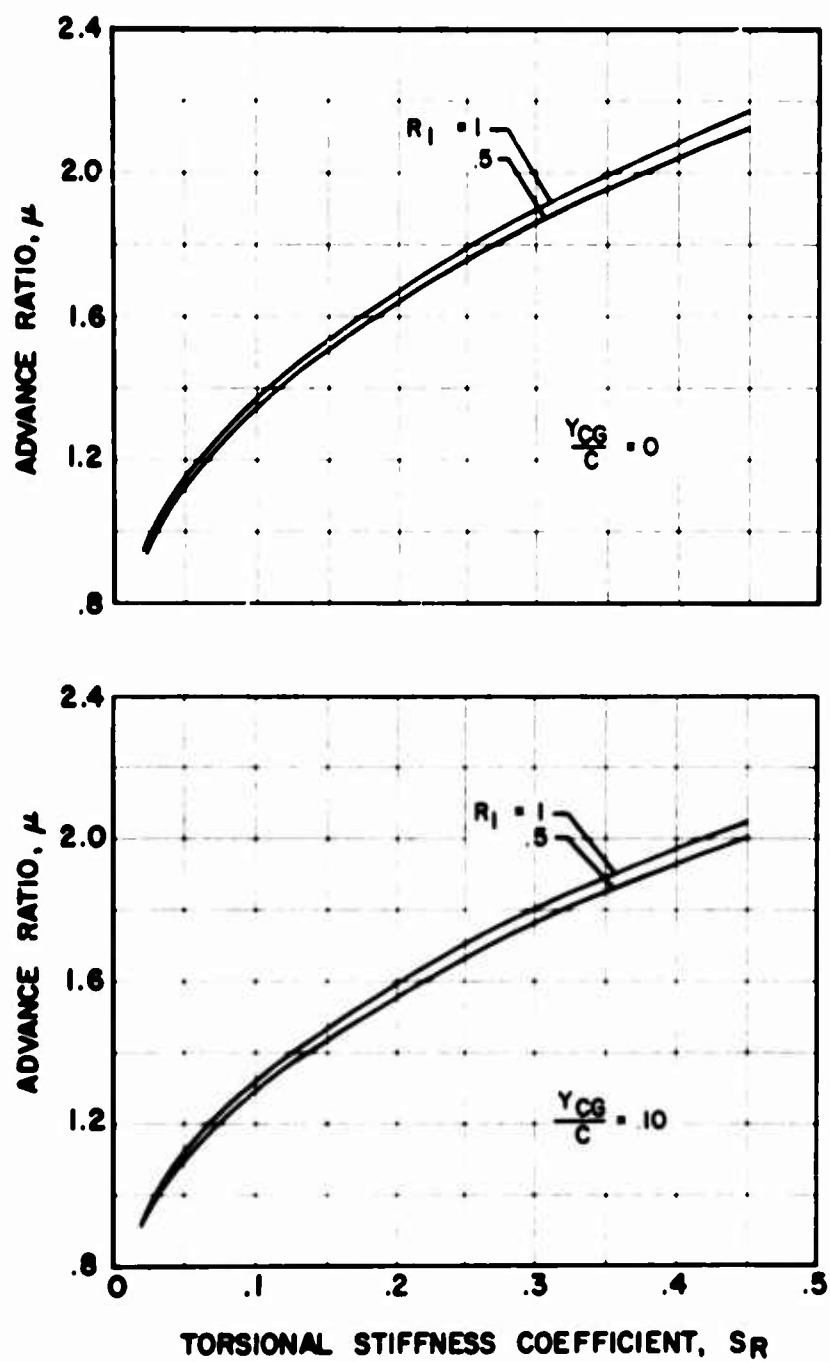


Figure 9. Effect of Linear Variation in Inertia on Retreating Blade Torsional Divergence; $1/K = .001$, $x_{0A} = 0$, $x_{0s} = 0$, $\alpha_0 = 2\pi$

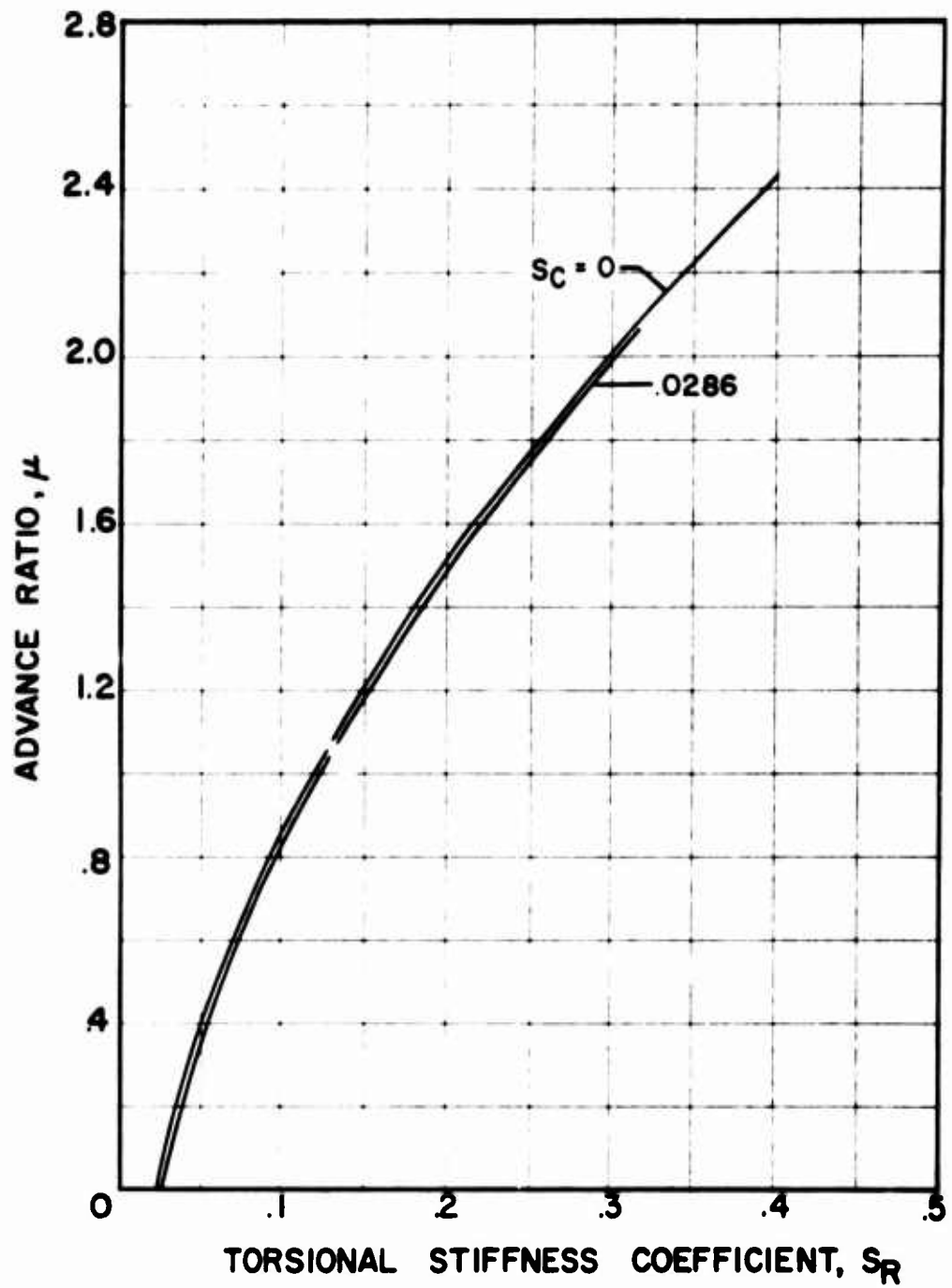


Figure 10. Effect of Prandtl-Glauert Mach Number Correction on Advancing Blade Torsional Divergence; $1/K = .001$, $Y_{CG}/C = -.10$, $X_{OA} = 0$, $X_{OS} = 0$

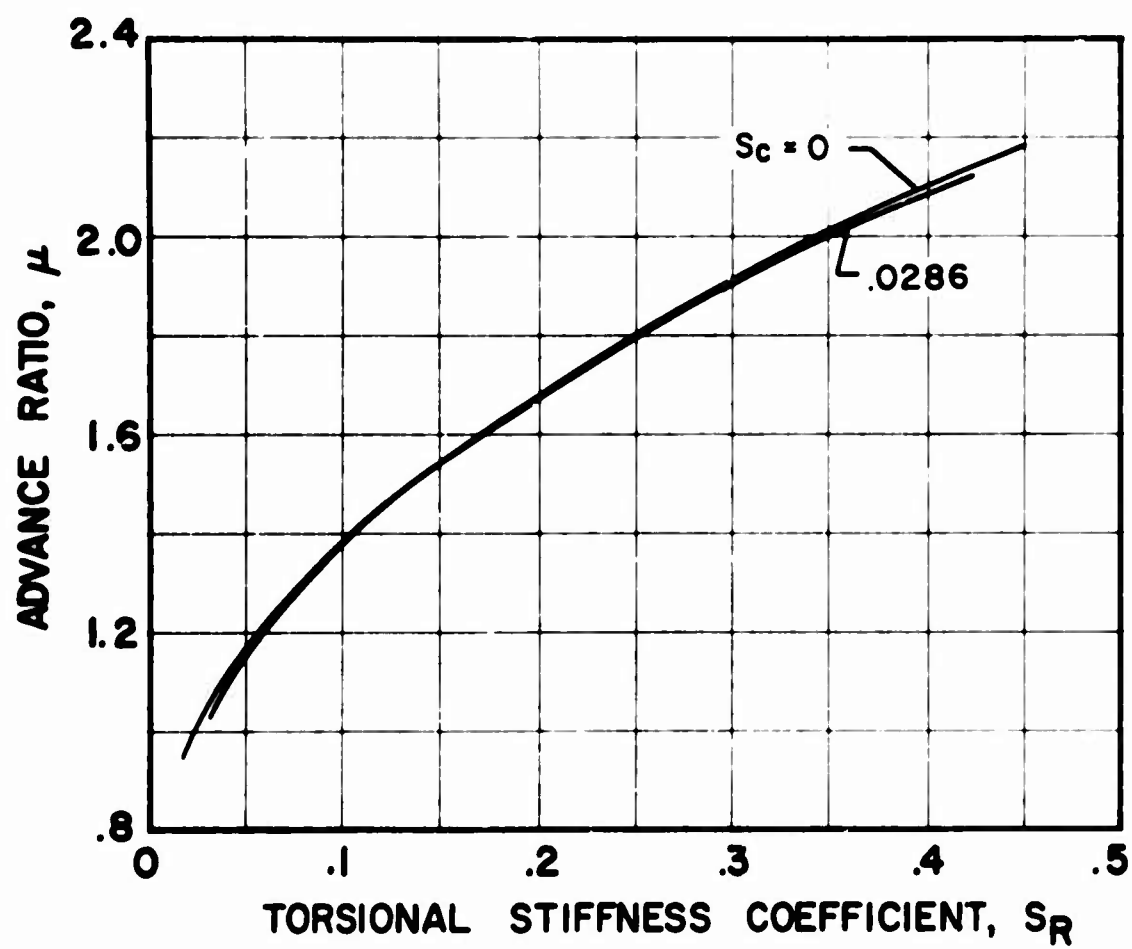


Figure 11. Effect of Prandtl-Glauert Mach Number Correction on Retreating Blade Torsional Divergence; $1/K = .001$, $Y_{CG}/C = 0$, $X_{OA} = 0$, $X_{OS} = 0$

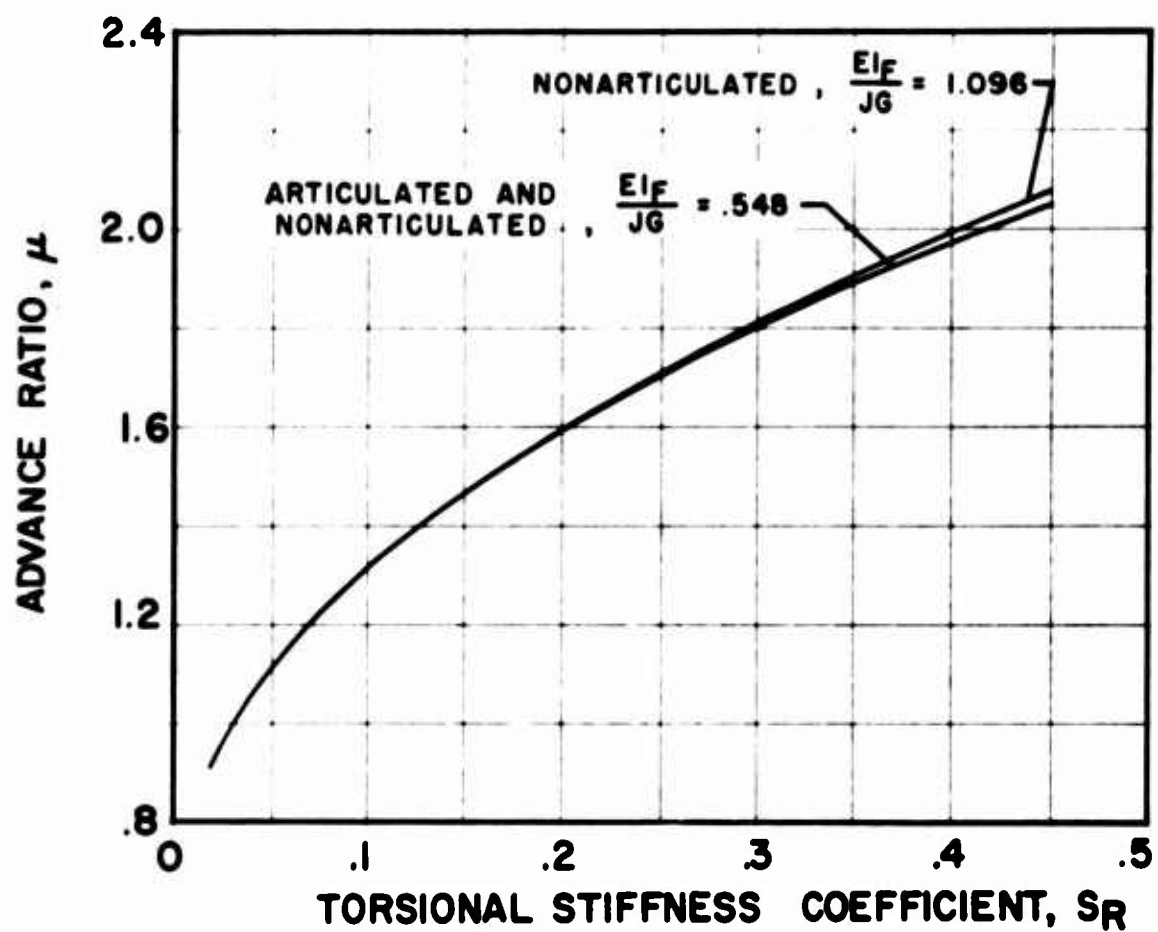


Figure 12. Retreating Blade Torsional Divergence on Articulated and Nonarticulated Blades; $1/K = .001$, $Y_{CG}/C = .005$, $X_{OA} = 0$, $X_{OS} = 0$, $\rho a_0 C_0^2/m = .168$.

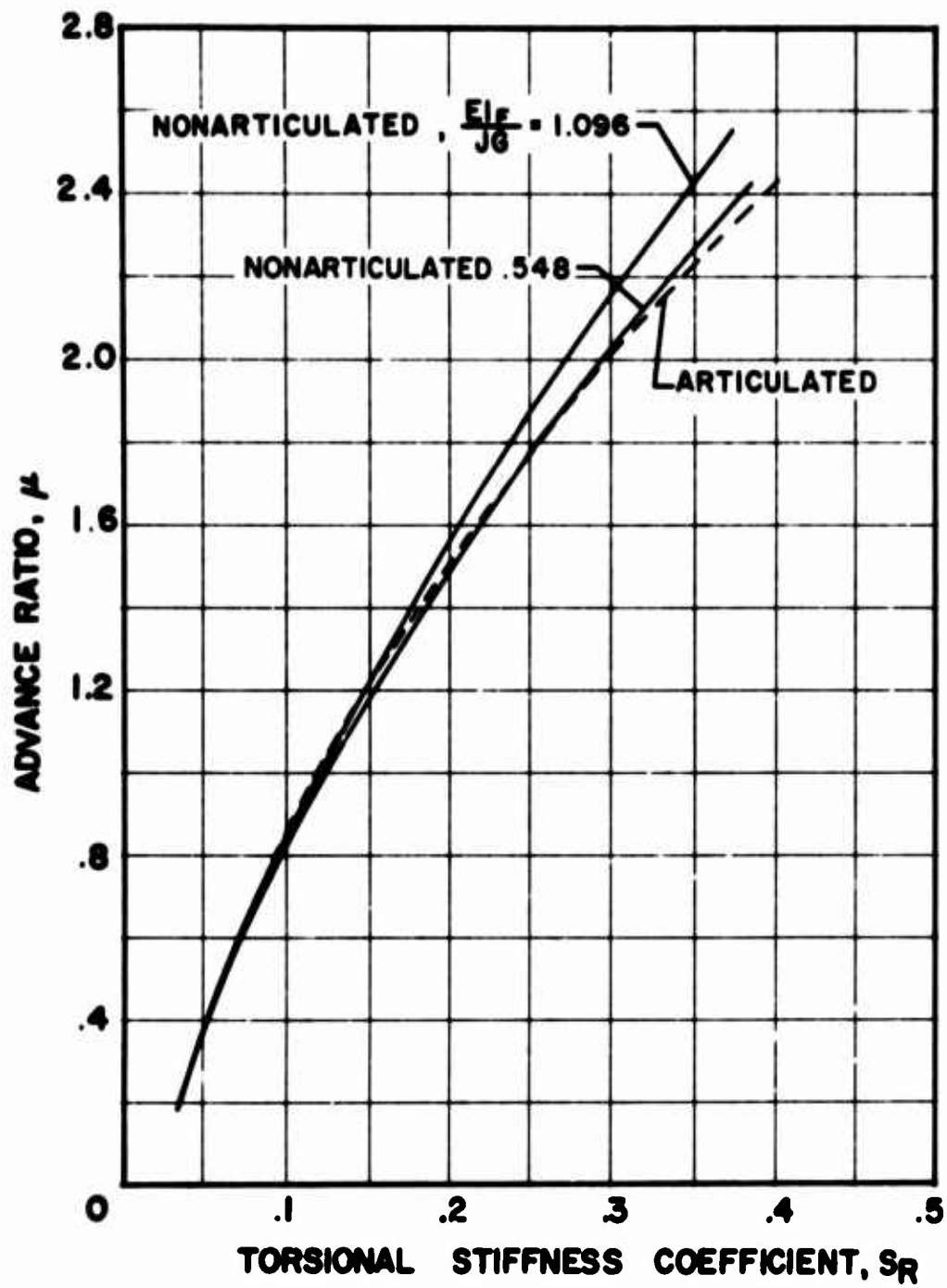


Figure 13. Advancing Blade Torsional Divergence on Articulated and Nonarticulated Blades; $1/K = .001$, $Y_{CG}/C = -.005$, $X_{OA} = 0$, $X_{OS} = 0$, $\rho a_0 C_0^2/m = .168$.

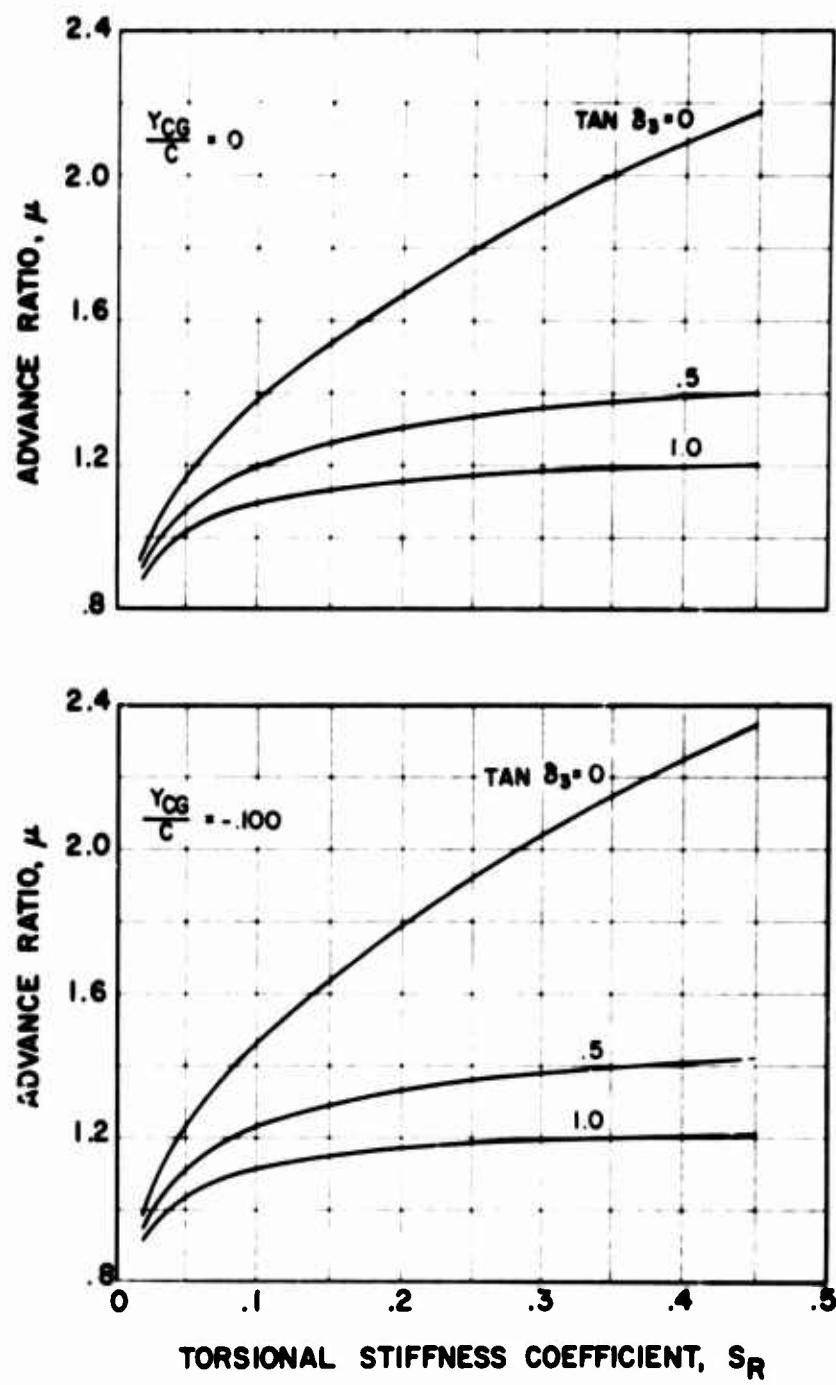


Figure 14. Effect of Pitch-Flap Coupling on Retreating Blade Torsional Divergence; $1/K = .001$, $X_{0A} = 0$, $X_{0S} = 0$, $\alpha_0 = 2\pi$.

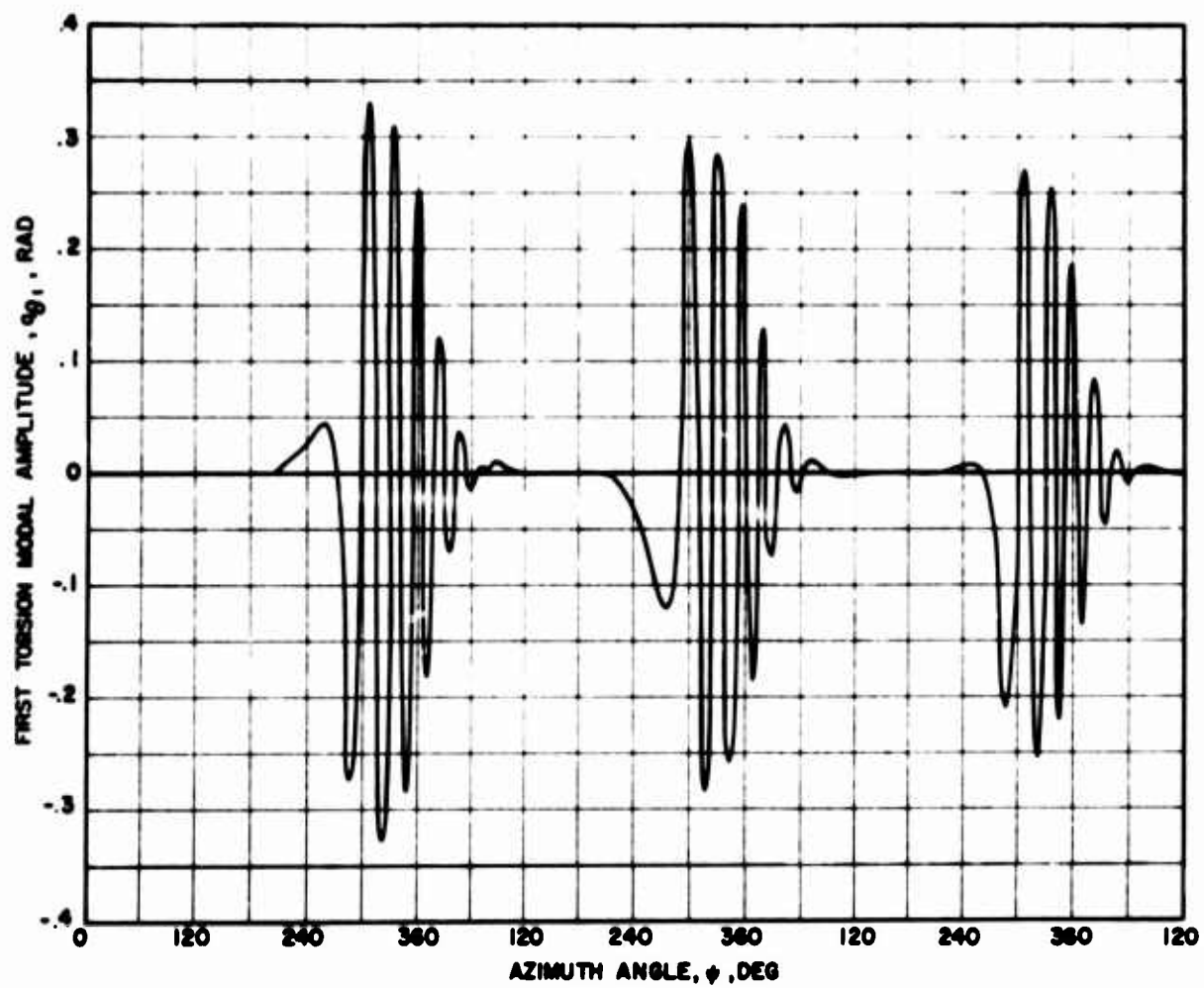


Figure 15. Blade First Torsion Modal Response Versus Azimuth Angle for the Basic Articulated Rotor; $\mu = 1.6$, $\theta_{75R} = 0^\circ$, $\alpha_s = 0$, $Y_{CG}/C = 0$, $M_{1,90} = .85$.

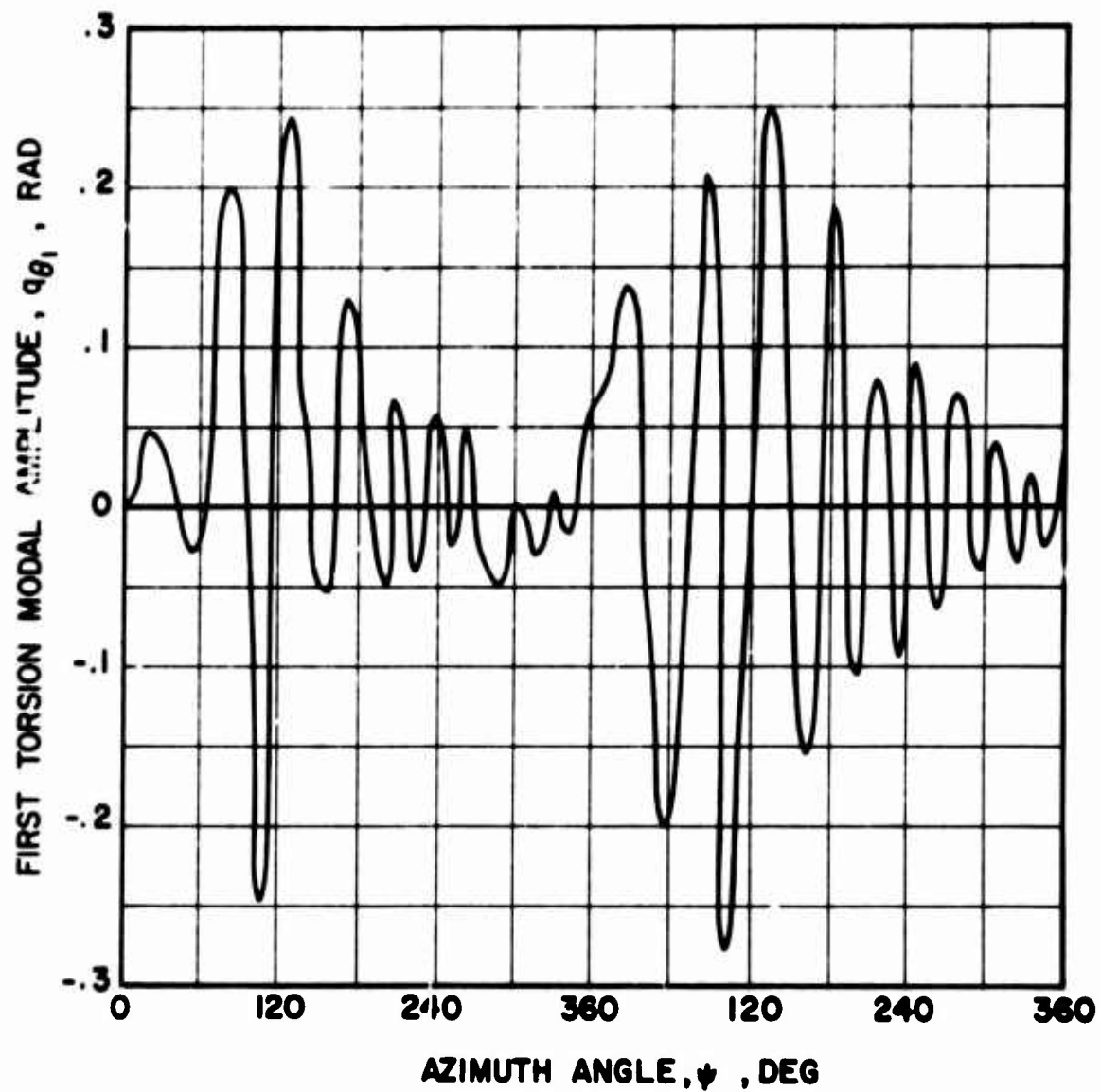


Figure 16. Blade First Torsion Modal Response Versus Azimuth Angle for the Articulated Rotor with Aft Center of Gravity; $\mu = .6$, $\theta_{75R} = 2^\circ$, $\alpha_s = 0$, $Y_{CG}/C = -.15$, $M_{1,90} = .85$.

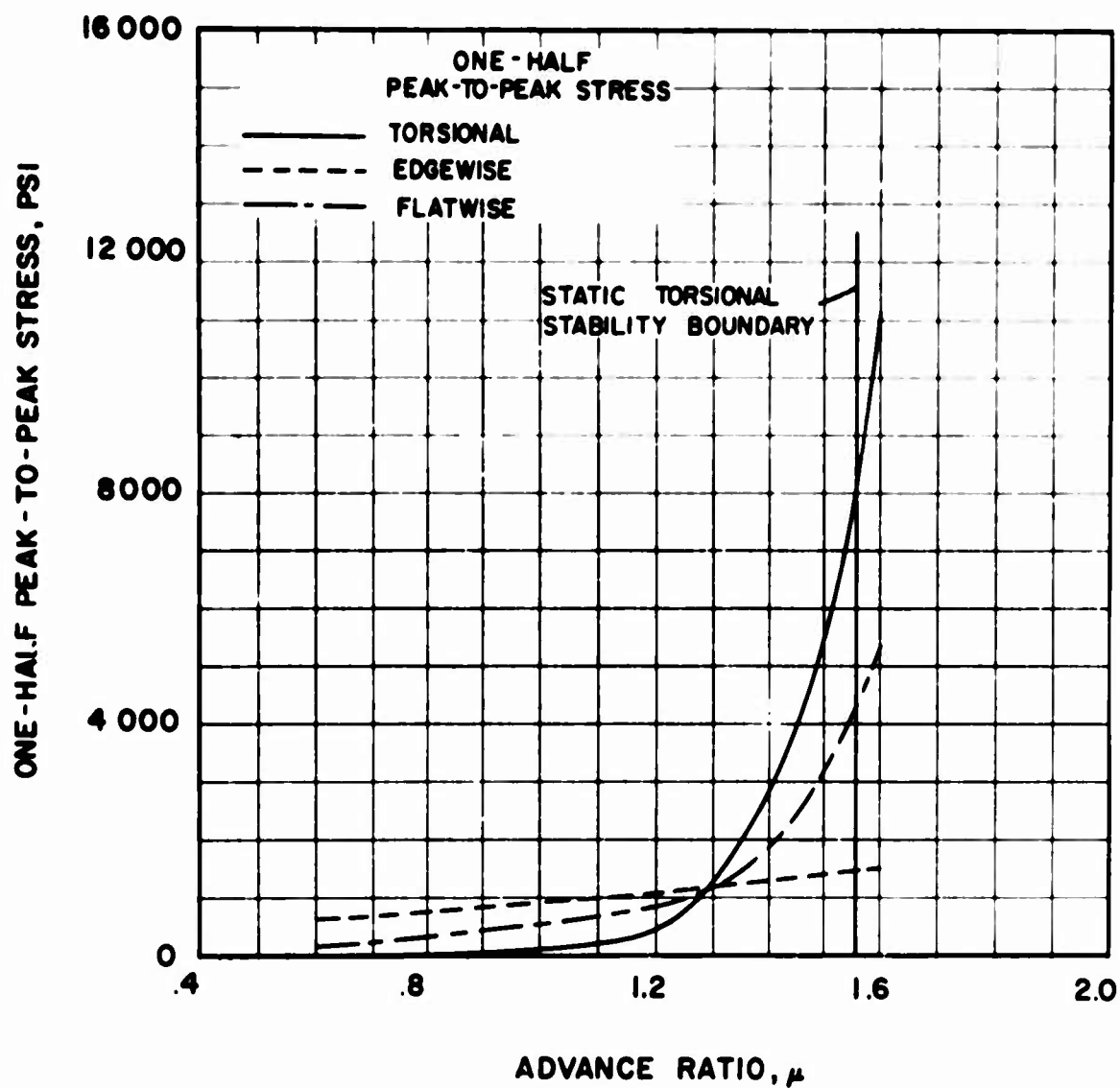


Figure 17. Vibratory Stress Versus Advance Ratio for the Basic Articulated Rotor; $1/K = 0$, $Y_{CG}/C = 0$, $X_{0A} = .12$, $X_{0S} = .060$, $M_{1,90} = .85$, $\delta_3 = 0$, $\alpha_0 \Omega^2 S_R = 96$

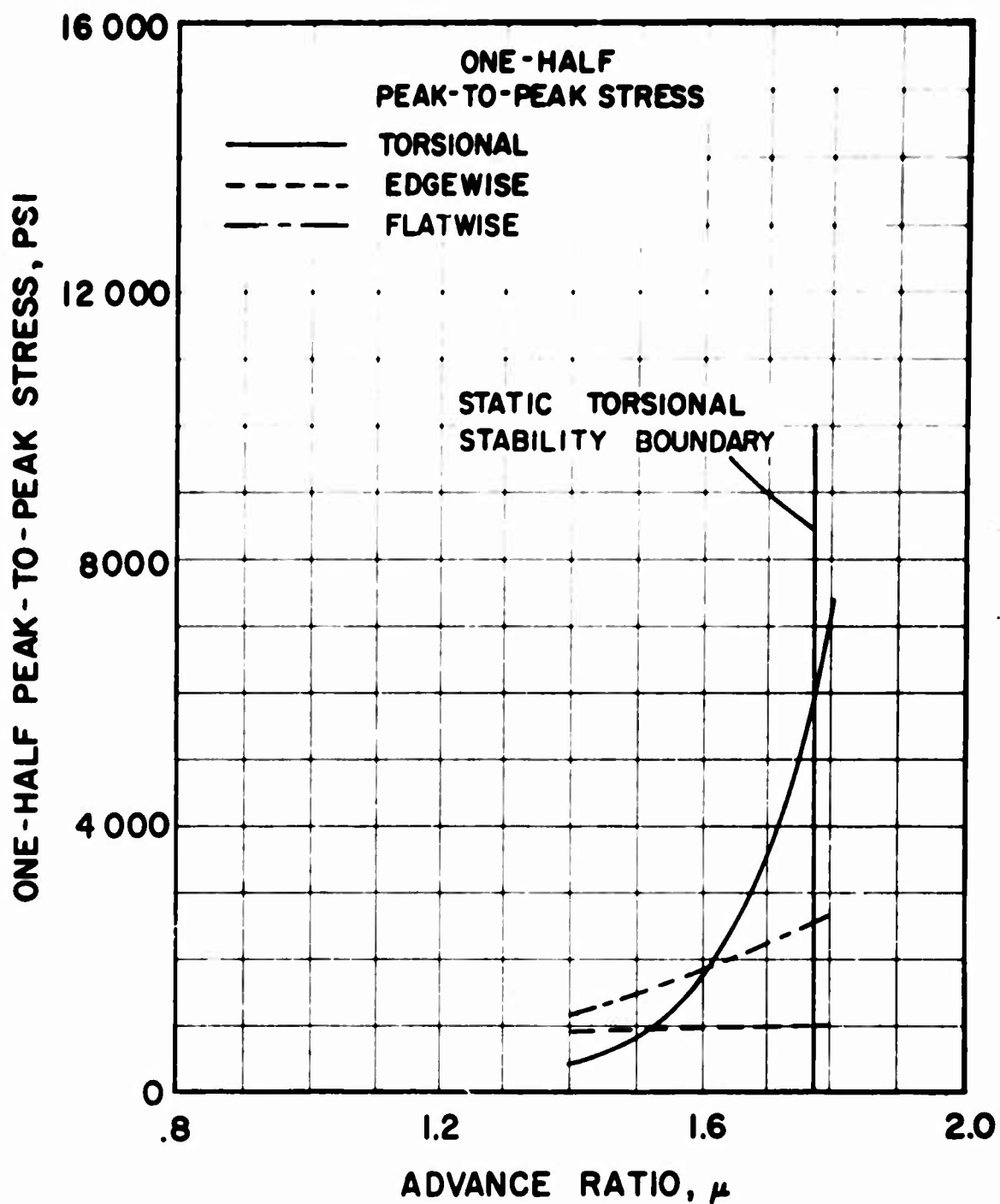


Figure 18. Vibratory Stress Versus Advance Ratio for the Basic Articulated Rotor with Reduced Air Density; $1/K = 0$, $Y_{CG}/C = 0$, $x_{0A} = .12$, $x_{0S} = .060$, $M_{1,90} = .85$, $\rho = .001585$ SLUGS/FT³, $\delta_3 = 0^\circ$, $a_0 \Omega^2 S_R = 144$.

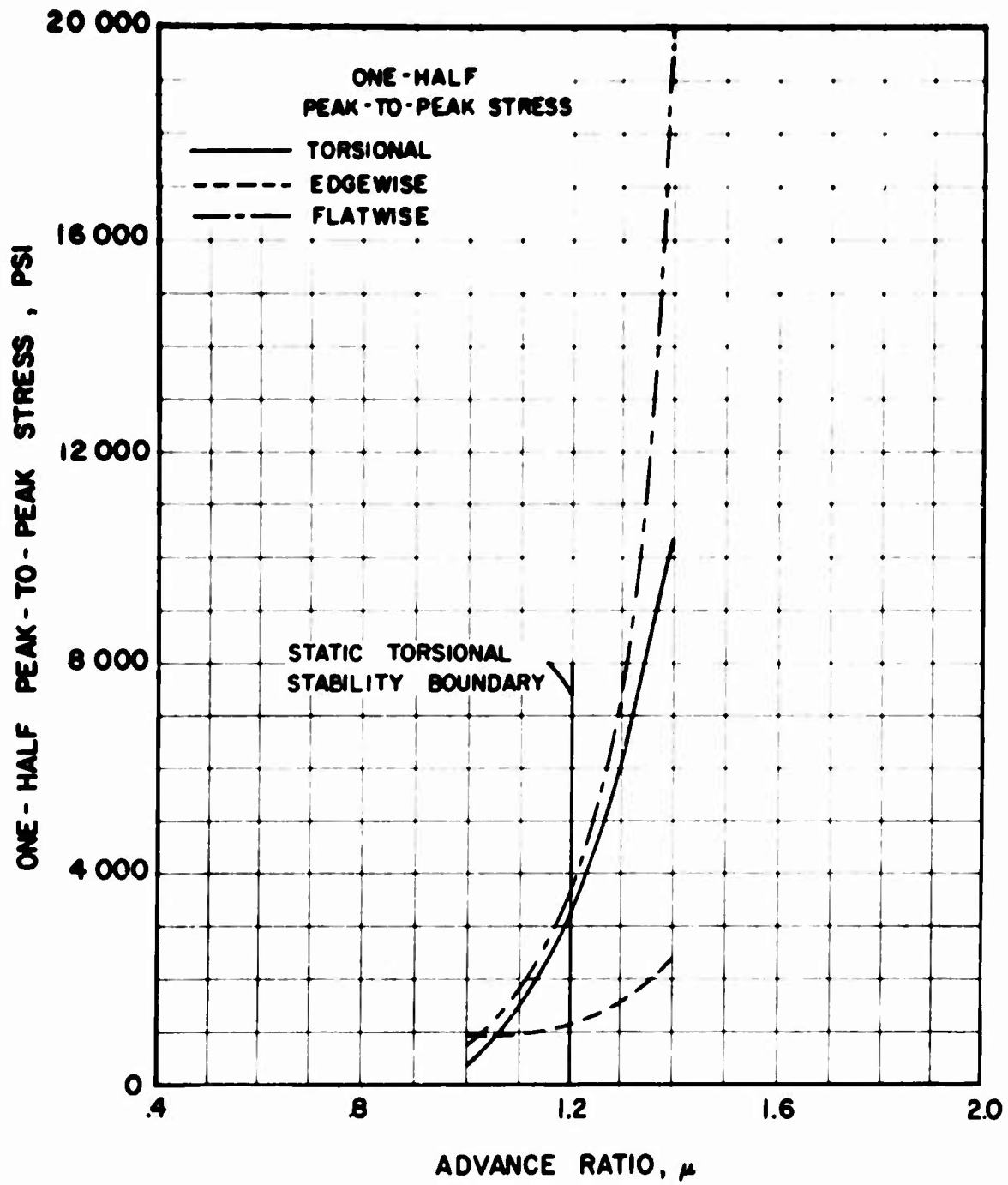


Figure 19. Vibratory Stress Versus Advance Ratio for the Basic Articulated Rotor With Control System Flexibility; $I/K = .2$, $Y_{CG}/C = 0$, $X_{OA} = .12$, $X_{OS} = .060$, $M_{1,90} = .85$, $\delta_3 = 0^\circ$, $\alpha_0 \Omega^2 S_R = 96$.

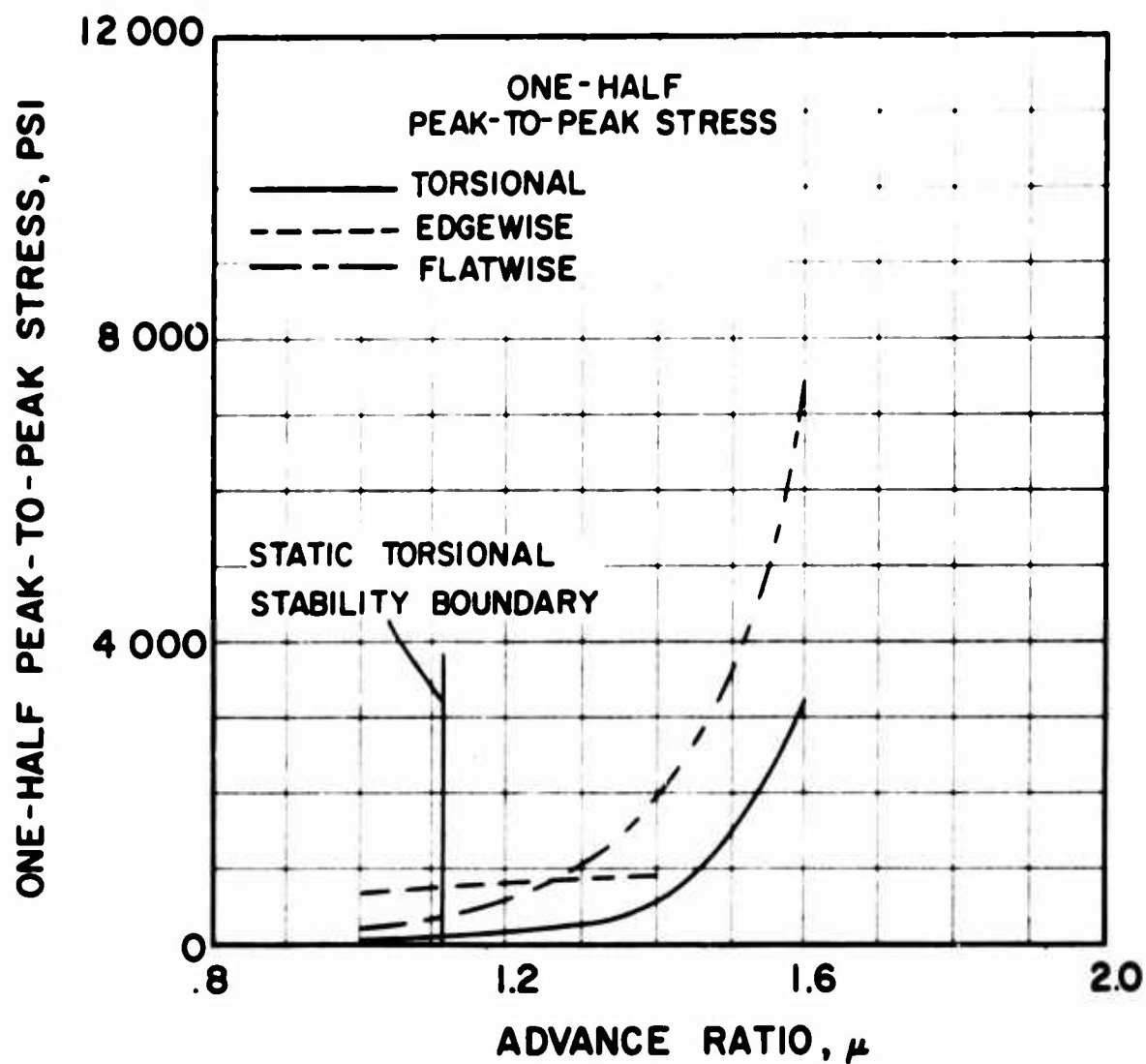


Figure 20. Vibratory Stress Versus Advance Ratio for the Basic Articulated Rotor With Pitch-Flap Coupling; $I/K = 0$, $Y_{CG}/C = 0$, $X_{0A} = .12$, $X_{0S} = .060$, $M_{1,90} = .85$, $\delta_3 = 45^\circ$, $a_0 \Omega^2 S_R = 96$.

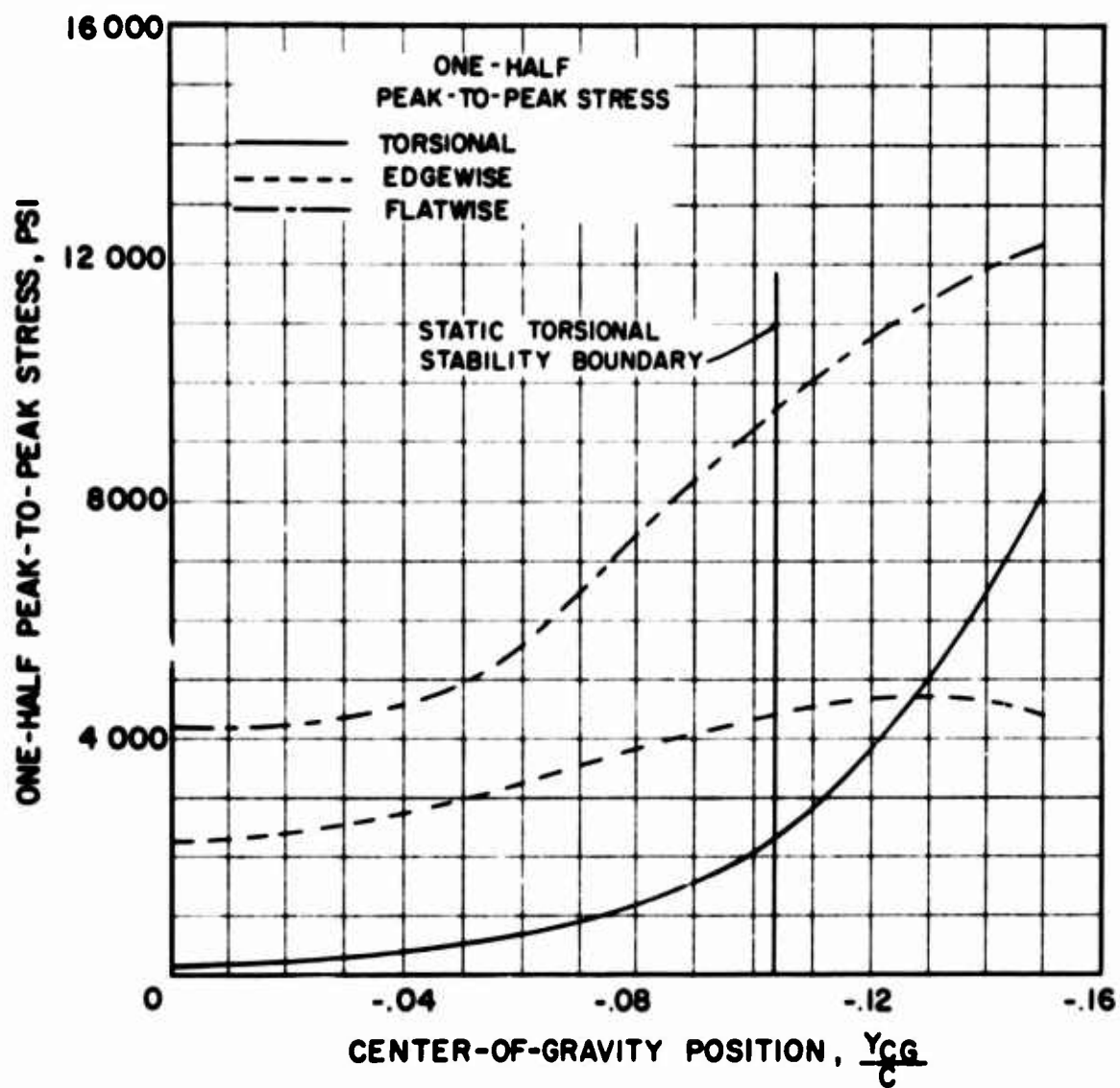


Figure 21. Vibratory Stress Versus Center-of-Gravity Offset for the Articulated Rotor; $I/K = 0$, $X_{0A} = .12$, $X_{0S} = .060$, $\mu = .6$, $M_{1,90} = .85$, $\delta_3 = 0$, $\sigma_0 \Omega^2 S_R = 96$, $\theta_{75R} = 2^\circ$.

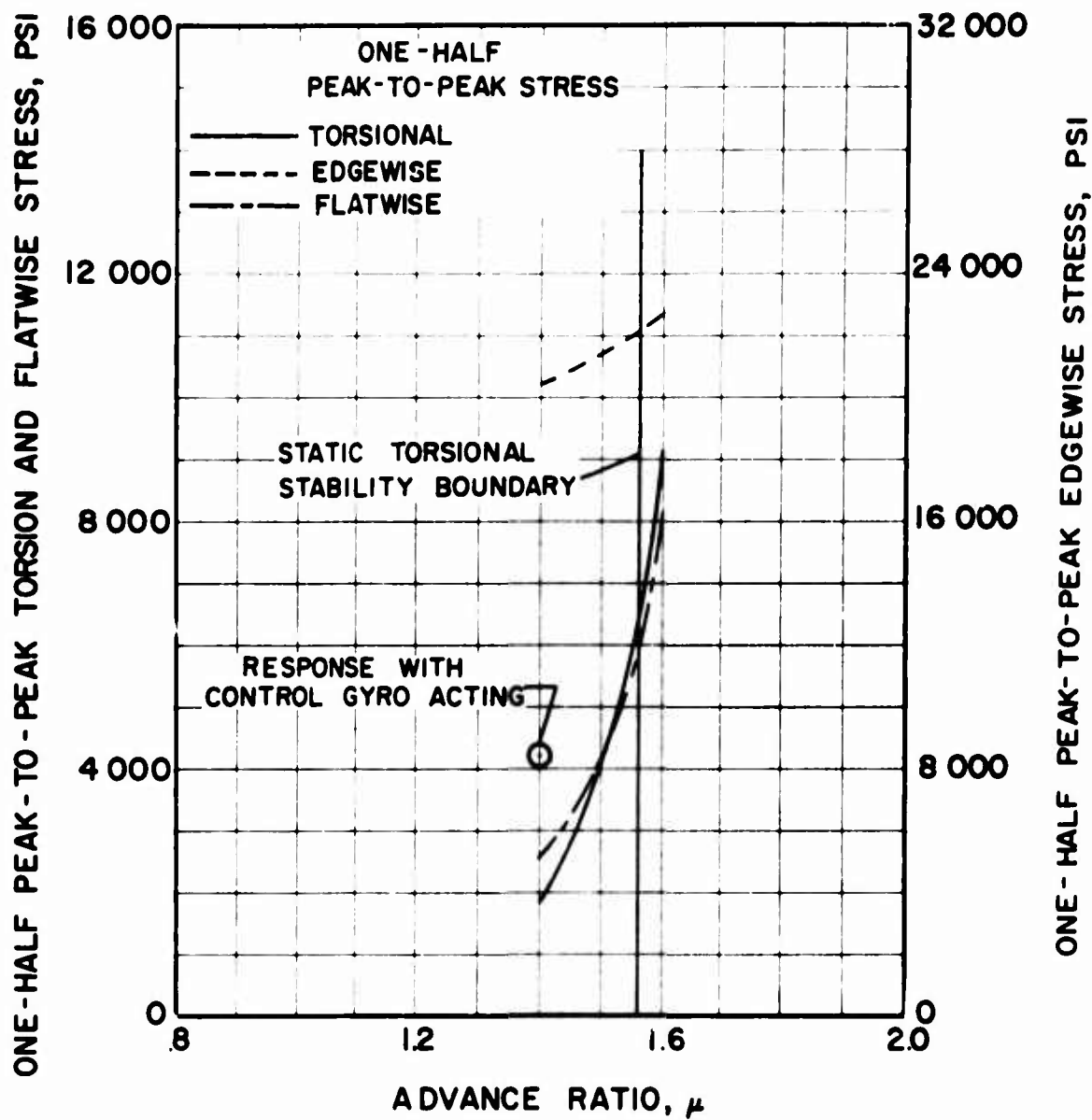


Figure 22. Vibratory Stress Versus Advance Ratio for the Basic Nonarticulated Rotor; $1/K = 0$, $Y_{CG}/C = 0$, $X_{0A} = .12$, $X_{0S} = .060$, $M_{1,90} = .85$, $\alpha_0 \Omega^2 S_R = 96$.

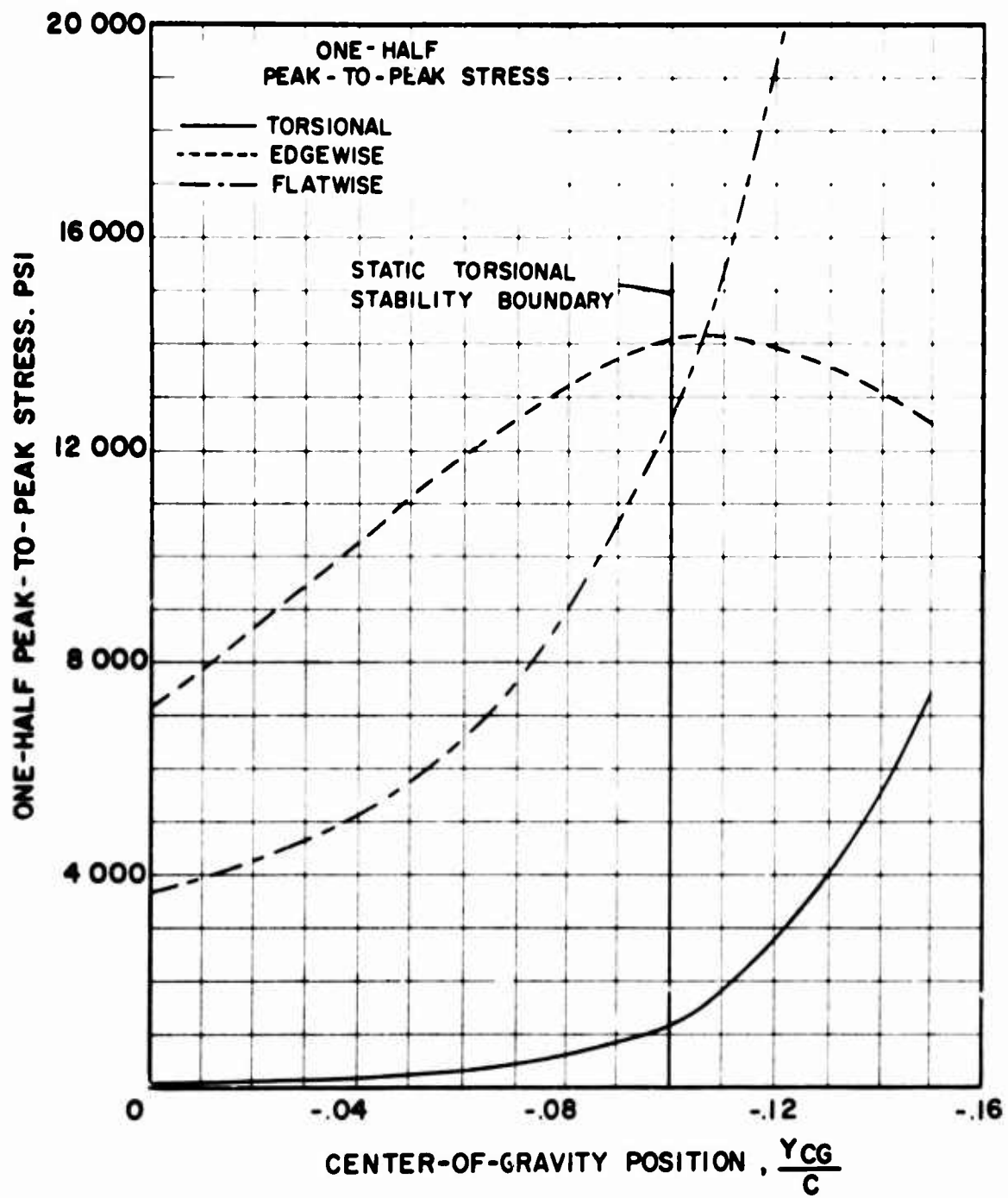


Figure 23. Vibratory Stress Versus Center-of-Gravity Offset for the Nonarticulated Rotor, $1/K = 0$, $X_{0A} = .12$, $X_{0S} = .060$, $\mu = .6$, $M_{1,90} = .85$, $a_0 \Omega^2 S_R = 96$, $\theta_{75R} = 2^\circ$, $\alpha_S = 0$, $A_{1S} = -1^\circ$, $B_{1S} = 2^\circ$.

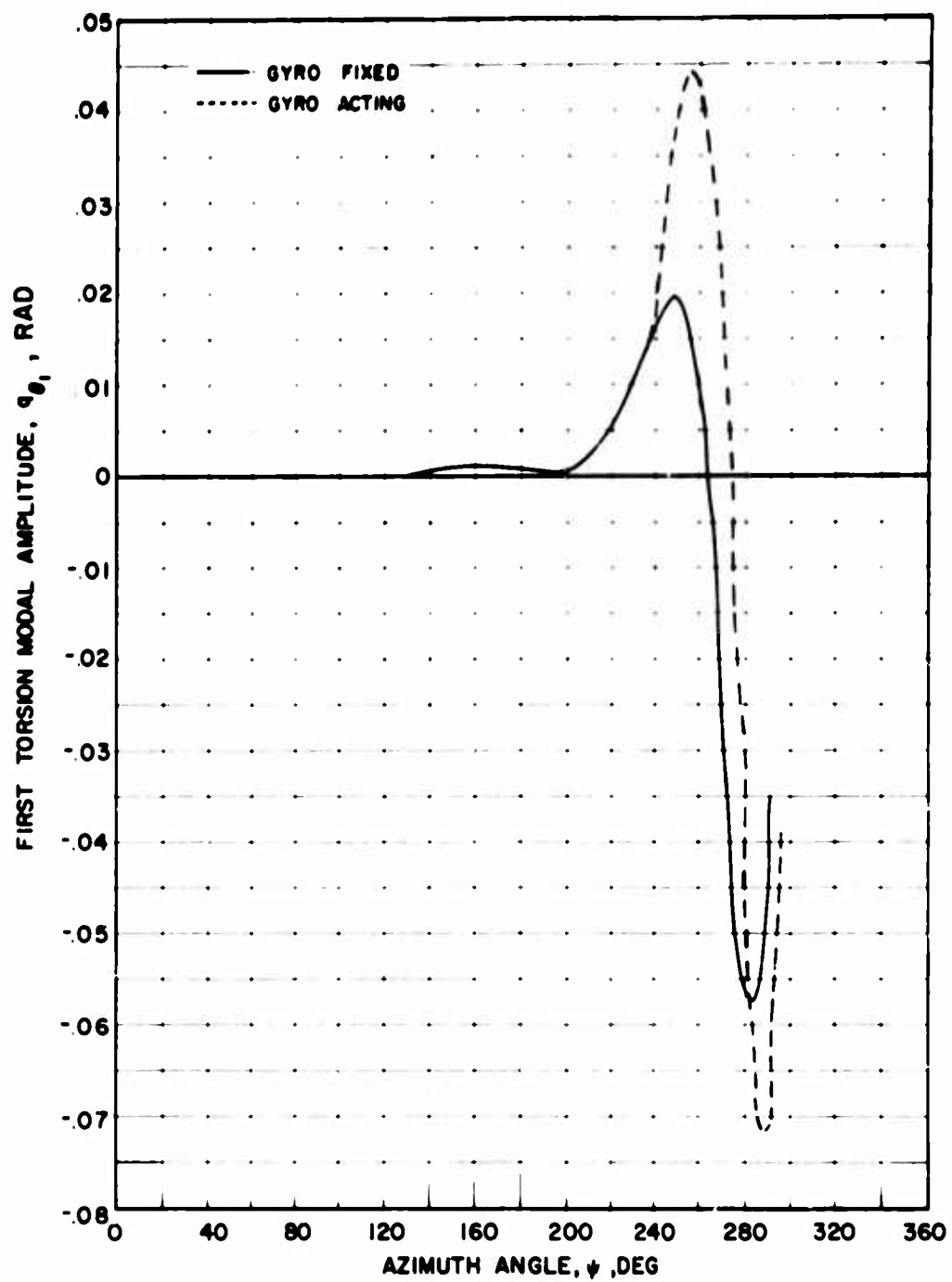


Figure 24. Blade First Torsion Modal Response Versus Azimuth Angle for the Nonarticulated Rotor; $\gamma_{cg}/C = 0$, $\mu = 1.4$, $M_{1,90} = .85$.

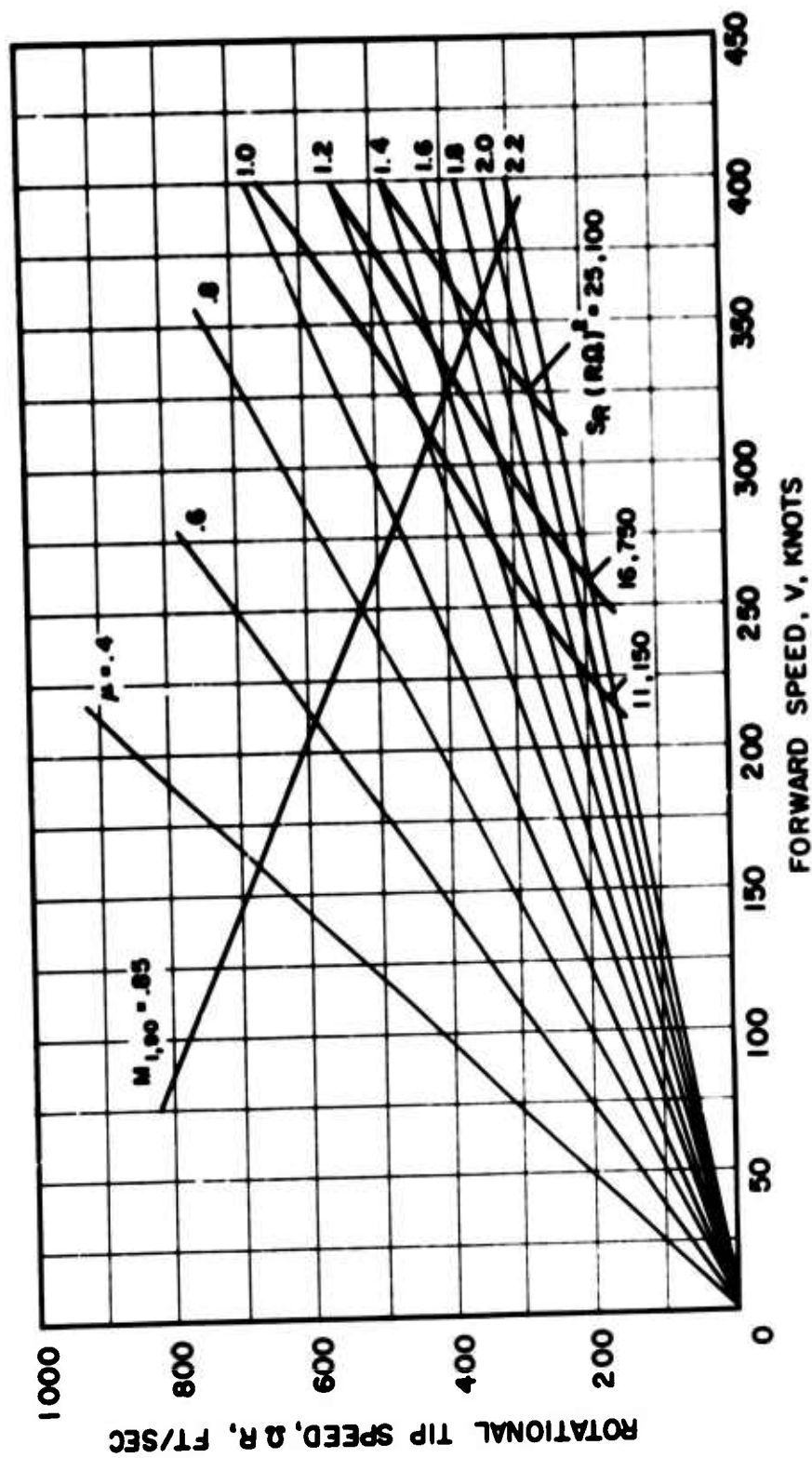


Figure 25. Effects of Torsional Stiffness Coefficient Variations on Typical Torsional Divergence Flight Condition Boundaries;
 $1/K = .001$, $Y_{CG}/C = 0$, $X_{OA} = .25$, $X_{OS} = 0$, $\alpha_0 = 2\pi$,
 $S_R (RQ)^2 = 2GJ/\rho \alpha_0 C_0^2 R^2$.

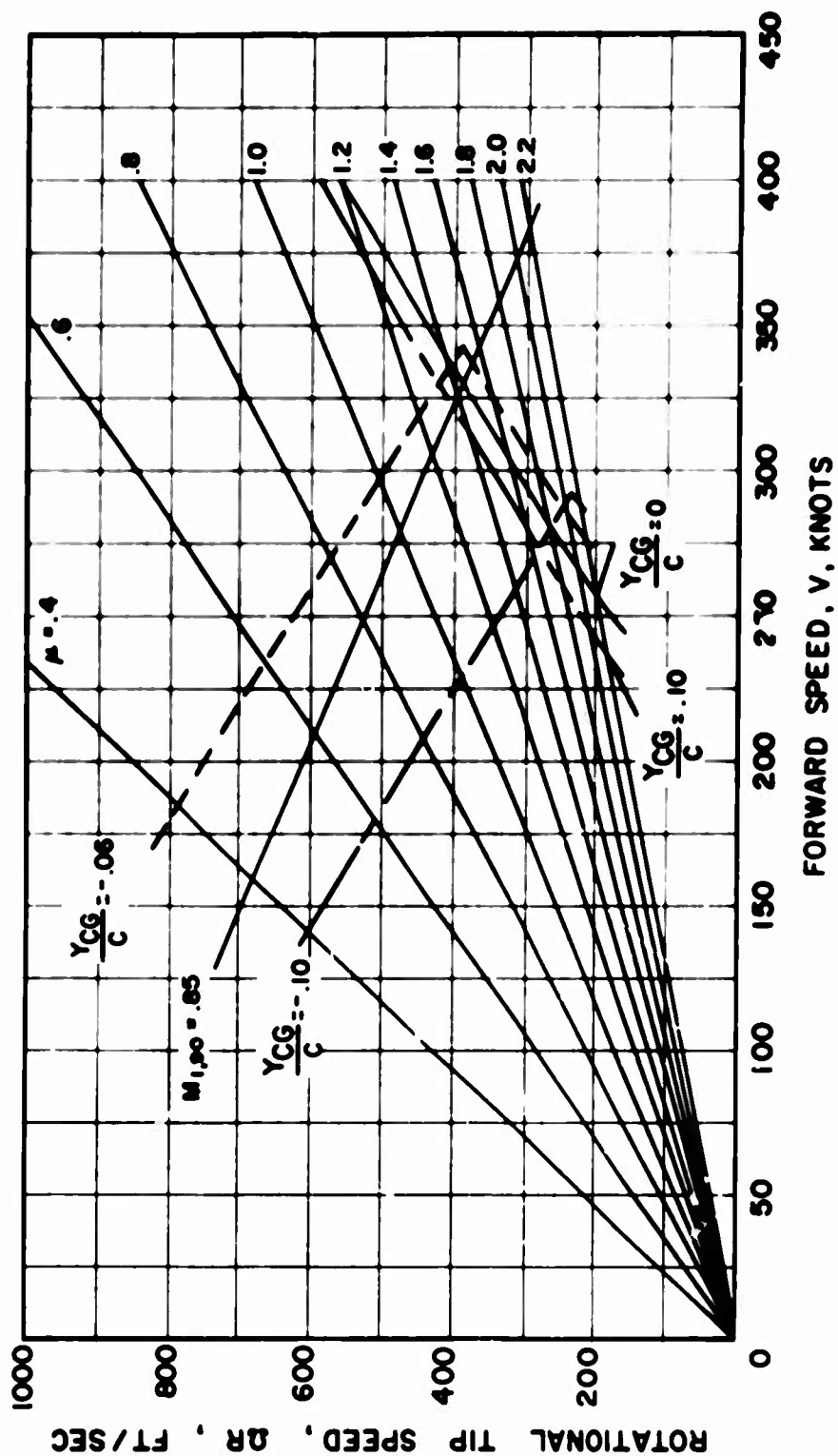


Figure 26. Effects of Chordwise Center of Gravity Location on Typical Torsional Divergence Flight Condition Boundaries; $1/K = .001$, $X_{0a} = .25$, $X_{0s} = 0$, $\alpha_0 = 2\pi$, $S_A(R\Omega)^2 = 2GJ/\rho\alpha_0 C_0^2 R^2 = 16,750 \text{ FT}^2/\text{SEC}^2$.

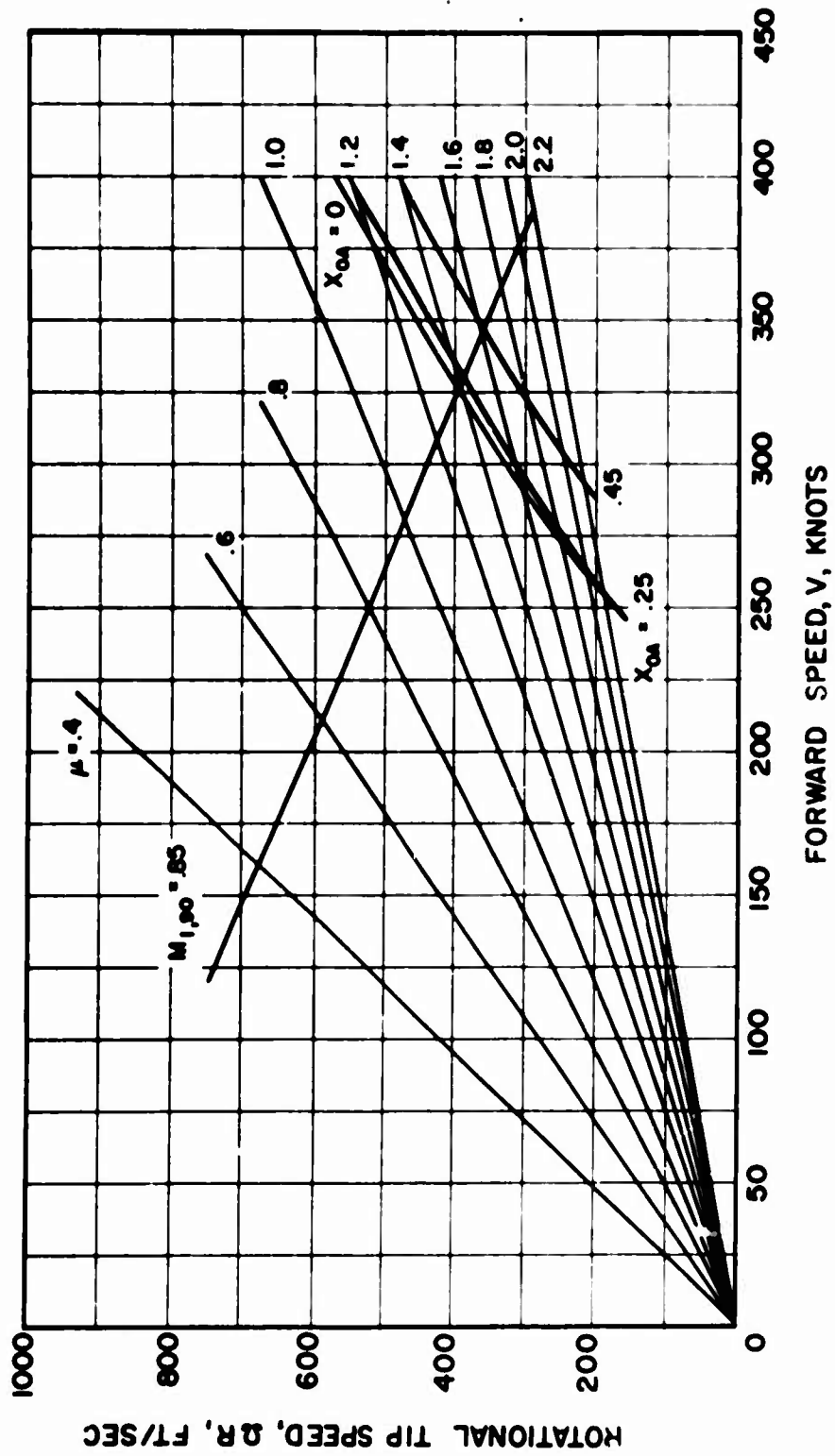


Figure 27. Effects of Aerodynamic Root Cutout on Typical Torsional Divergence Flight Condition Boundaries; $I/K = .001$, $Y_{CG}/C = 0$, $X_{OS} = 0$, $\alpha_0 = 2\pi$, $S_H(R\Omega)^2 = 26J/\rho\alpha_0 C_0^2 R^2 = 16,750 \text{ FT/SEC}^2$

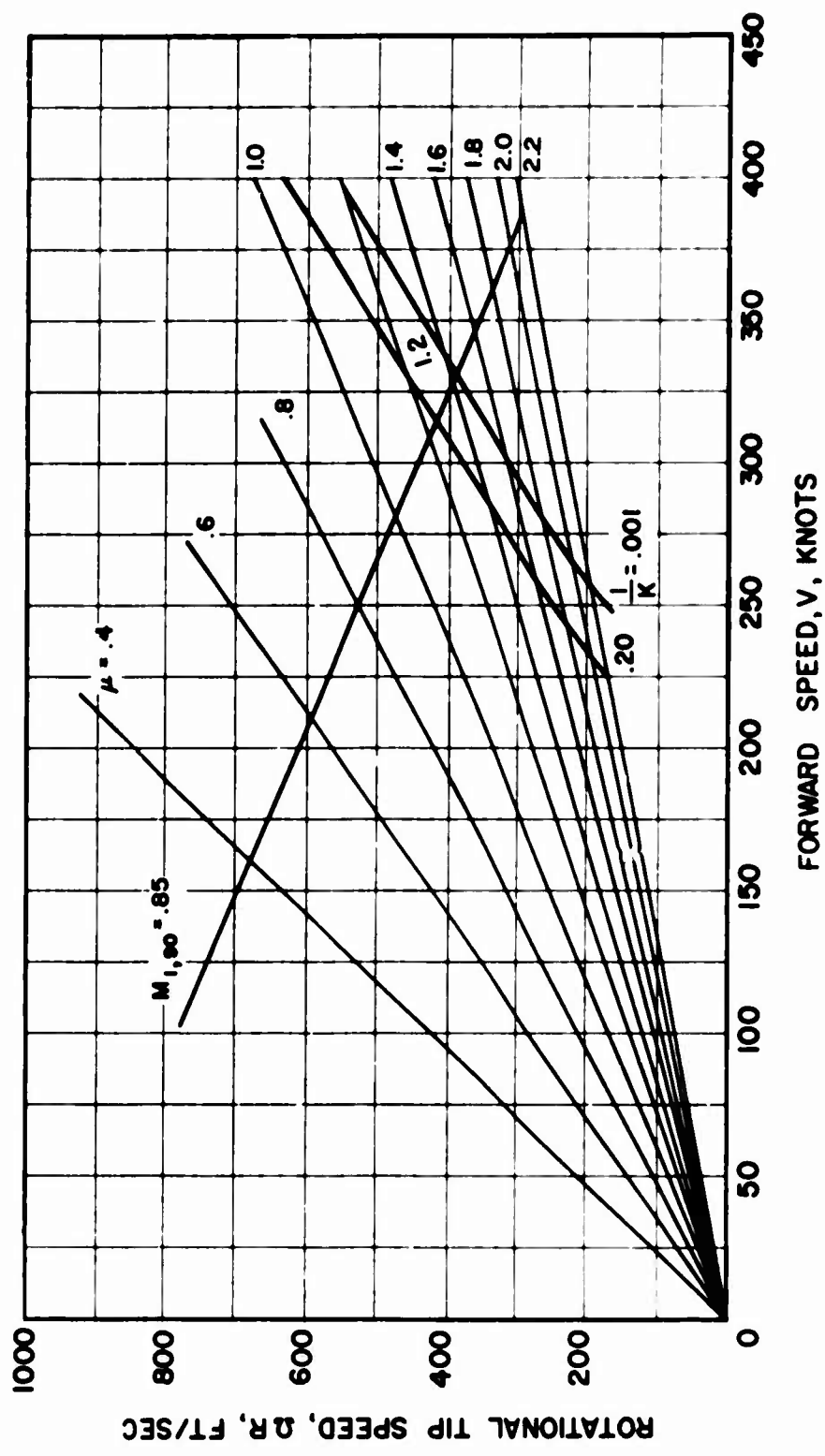


Figure 28. Effects of Control Stiffness on Typical Torsional Divergence Flight Condition Boundaries; $Y_{CG}/C = 0$, $X_{OA} = .25$, $X_{OS} = 0$, $\alpha_0 = 2\pi$, $S_N(R\Omega)^2 = 2GJ/\rho\alpha_0 C_0 R^2 = 16,750 \text{ FT/SEC}^2$.

TABLE I. BASIC PROPERTIES OF ROTOR SYSTEM USED IN TORSIONAL DIVERGENCE STUDIES WITH THE NORMAL MODE TRANSIENT ANALYSIS

Item	Symbol	Value	Unit
Radius	R	31.0	ft
Number of Blades	b	5	-
Chord	c	1.52	ft
Flatwise Stiffness	EI_F	1.56×10^8	lb-ft ²
Edgewise Stiffness	EI_E	1.74×10^8	lb-ft ²
Torsional Stiffness	GJ	2.43×10^8	lb-ft ²
Mass per Unit Length	m	.202	slugs/ft
Flap-Lag Hinge Offset	\bar{e}	.0339	-
Tip Loss Factor	B	.97	-
Aerodynamic Root Cutout	X_{oa}	.12	
Structural Root Cutout	X_{os}	.060	

TABLE II. ROTOR CONFIGURATIONS FOR TORSIONAL DIVERGENCE STUDY WITH THE NORMAL MODE TRANSIENT ANALYSIS

Configuration Number	Articulated or Nonarticulated	$\frac{1}{K}$	$\tan \delta$	$\frac{Y_{C0}}{C}$	Control Gyro Condition
1	Articulated	.001	0.0	0.0	-
2	Articulated	.20	0.0	0.0	-
3	Articulated	.001	1.0	0.0	-
4	Articulated	.001	0.0	-.05	-
5	Articulated	.001	0.0	-.10	-
6	Articulated	.001	0.0	-.15	-
7	Nonarticulated	.001	-	0.0	Fixed
8	Nonarticulated	.001	-	-.05	Fixed
9	Nonarticulated	.001	-	-.10	Fixed
10	Nonarticulated	.001	-	-.15	Fixed
11	Nonarticulated	.001	-	0.0	Acting

TABLE III. FLIGHT CONDITIONS FOR TORSIONAL DIVERGENCE STUDY
WITH NORMAL MCDE TRANSIENT ANALYSIS

Condition Number	Advance Ratio, μ	Air Density, ρ Slugs/ft ³
1	0.6	.002378
2	1.0	.002378
3	1.2	.002378
4	1.4	.002378
5	1.6	.002378
6	1.4	.001585
7	1.6	.001585
8	1.8	.001585

TABLE IV. CONFIGURATION AND FLIGHT COMBINATION COMBINATIONS
FOR TORSIONAL DIVERGENCE STUDY WITH THE NORMAL
MODE TRANSIENT ANALYSIS

Configuration (TABLE II)	Condition (TABLE III)
1	1,2,3,4,5,6,7,8
2	2,3,4
3	2,3,4,5
4	1
5	1
6	1
7	4,5
8	1
9	1
10	1
11	4

CONCLUSIONS

1. The static torsional divergence boundary usually approximates a practical operating limit defined by a rapid rise in peak-to-peak torsional stress. This approximation is valid for a useful number of blade parameters.
2. Critical advance ratio for static torsional divergence is affected most strongly by blade elastic torsional stiffness, air density, lift-curve slope, rotational tip speed, chord, radius, chordwise center-of-gravity position, aerodynamic root cutout, control stiffness, and structural root cutout.
3. The torsional divergence characteristics for articulated and non-articulated blades of conventional stiffness are practically identical.
4. The basic parameters for the study of static torsional divergence are the advance ratio μ and the torsional stiffness coefficient S_θ .
5. The use of the first natural vibration mode as a divergence mode is a good simplifying assumption for static divergence calculations.

RECOMMENDATIONS

The present static stability analysis is adequate for the rapid generation of approximate blade operating boundaries for a broad range of parameters and blade characteristics. In order to predict the effects of pitch-flap coupling and inertia variations with greater confidence, a two-degree-of-freedom torsion-flapping dynamic analysis should be considered.

Unclassified

Security Classification

DOCUMENT CONTROL DATA - R & D		
<i>(Security classification of title, body of abstract and indexing annotation must be entered when the overall report is classified)</i>		
1. ORIGINATING ACTIVITY (Corporate author) Sikorsky Aircraft Division of United Aircraft Corporation Stratford, Connecticut		2a. REPORT SECURITY CLASSIFICATION Unclassified
2. REPORT TITLE PREDICTION OF ROTOR INSTABILITY AT HIGH FORWARD SPEEDS Volume IV - Torsional Divergence		2b. GROUP
4. DESCRIPTIVE NOTES (Type of report and inclusive dates) Final Report		
5. AUTHOR(S) (First name, middle initial, last name) Charles F. Niebanck H. L. Elman		
6. REPORT DATE February 1969	7a. TOTAL NO. OF PAGES 127	7b. NO. OF REFS 0
8a. CONTRACT OR GRANT NO. DA 44-177-AMC-332(T)	8b. ORIGINATOR'S REPORT NUMBER(S) USAAVLABS Technical Report 68-18D	
8c. PROJECT NO. Task 1F125901A13904	8d. OTHER REPORT NO(S) (Any other numbers that may be assigned this report) SER-50469	
10. DISTRIBUTION STATEMENT This document has been approved for public release and sale; its distribution is unlimited.		
11. SUPPLEMENTARY NOTES Volume IV of a 5-volume report	12. SPONSORING MILITARY ACTIVITY U. S. Army Aviation Materiel Laboratories Fort Eustis, Virginia	
13. ABSTRACT A simple energy balance method for determining static stability was used to evaluate rotor blade torsional divergence boundaries, and a set of blade design charts was generated. To compare the results of this simple analysis with a more refined method, and to investigate the effects of parameters not included in the simple method, other calculations were made with the extended Normal Mode Transient Analysis. One type of practical rotor blade operating boundary is defined by peak-to-peak torsional stress. The static torsional divergence stability boundary usually approximates this practical operating limit, as verified by the Normal Mode Transient Analysis calculations. This approximation is valid for an important number of blade parameters. Recommended preliminary design procedures, incorporating the charts generated for this volume are given for the rapid definition of blades with adequate torsional stiffness.		

DD FORM 1473

REPLACES DD FORM 1473, 1 JAN 64, WHICH IS OBSOLETE FOR ARMY USE.

Unclassified

Security Classification

Unclassified

Security Classification

14.	KEY WORDS	LINK A		LINK B		LINK C	
		ROLE	WT	ROLE	WT	ROLE	WT
Helicopter Rotor Blade Torsional Divergence							

Unclassified

Security Classification